

Dagmar de Rooij

Molecular Dynamics Simulations of Interactions between Hydrogen and Fusion-relevant Materials

**IPP 17/21
2010**

Molecular Dynamics Simulations
of Interactions between
Hydrogen and Fusion-relevant Materials

© Copyright 2010 Dagmar de Rooij
Printed by Ipskamp Drukkers

The work described in this dissertation was carried out at the FOM Institute for Plasma
Physics Rijnhuizen in Nieuwegein, The Netherlands.

ISBN 978-90-393-5282-3

Molecular Dynamics Simulations of Interactions between Hydrogen and Fusion-relevant Materials

Moleculaire dynamica simulaties
van interacties tussen
waterstof en fusierelevante materialen
(met een samenvatting in het Nederlands)

Proefschrift

ter verkrijging van de graad van doctor aan de Universiteit Utrecht op gezag van de rector magnificus, prof.dr. J.C. Stoof, ingevolge het besluit van het college voor promoties in het openbaar te verdedigen op woensdag 24 februari 2010 des middags te 12.45 uur
door

Elisabeth Dagmar de Rooij

geboren op 12 september 1965 te Gräfelfing, Duitsland

Promotoren: Prof.dr. W.J. Goedheer
Prof.dr. A.W. Kleyn

This work, supported by the European Communities under the contract of Association between EURATOM/FOM, was carried out within the framework of the European Fusion Programme with financial support from NWO and the research school CPS. The views and opinions expressed herein do not necessarily reflect those of the European Commission.

*Two roads diverged in a wood, and I –
I took the one less traveled by,
And that has made all the difference.*
- Robert Frost

Engage!
- Captain Jean-Luc Picard

Contents

1	Introduction	1
1.1	Background Story: The Energy Problem	1
1.1.1	Energy Sources	1
1.2	Fusion Feasibility	3
1.2.1	Main Challenges	3
1.2.2	Research of Plasma Surface Interactions	7
1.2.3	This Work	9
2	Molecular Dynamics	11
2.1	What is Molecular Dynamics?	11
2.1.1	Circumventing Schrödinger	11
2.1.2	Newton's Law	12
2.1.3	The MD code	13
2.1.4	Interpretation of Temperature	17
2.1.5	Thermostat	17
2.1.6	Bulk Simulation	20
2.1.7	Sample Creation	21
2.1.8	Bombardment Simulation	21
2.1.9	Determining Material Properties	24
2.1.10	Limitations	25
3	Overview of the Studies	27
4	Sticking Probability of Hydrogen on Diamond	29
4.1	Introduction	29
4.2	Modelling	29
4.3	Results	30
4.4	Conclusions	35
5	Diamond and Amorphous Hydrogenated Carbon Compared	37
5.1	Introduction	37
5.2	Modelling	38
5.3	Results	39
5.3.1	Retained Hydrogen Fraction	39
5.3.2	Carbon Erosion Yield	41

5.3.3	Eroded Hydrocarbon Species	44
5.4	Conclusion	50
6	a-C:H under extremely high H fluxes	51
6.1	Introduction	51
6.2	Modelling	53
6.2.1	MD code	53
6.2.2	Simulated sample	53
6.2.3	Heat transport	55
6.2.4	Hydrogen pressure	56
6.3	Results & discussion	57
6.3.1	Flux dependency of the yield	57
6.3.2	Hydrogen buildup in the cumulatively bombarded sample . .	60
6.3.3	Eroded species	62
6.4	Conclusions	64
7	Redeposition of Hydrocarbons	67
7.1	Introduction	67
7.2	Modelling	68
7.3	Results	70
7.3.1	Sample Properties	70
7.3.2	Sticking Probability	70
7.3.3	Breaking of Hydrocarbons	76
7.4	Conclusions	77
8	Tungsten Carbide under Deuterium Bombardment	79
8.1	Introduction	79
8.2	Modelling	81
8.3	Results	82
8.3.1	The 50% Carbon Sample	82
8.3.2	The 95% Carbon Sample	90
8.3.3	The 15% Carbon Sample	92
8.3.4	Bubble Depths	93
8.3.5	Carbon and Tungsten Erosion Yields	94
8.4	Conclusions	94
9	Conclusions & Outlook	97
	List of Publications	109
	Computing Facilities	113

Summary	115
Samenvatting	117
Acknowledgements	119
Curriculum Vitae	121

Chapter 1

Introduction

1.1 Background Story: The Energy Problem

1.1.1 Energy Sources

Ever since humans learned to wield fire they satisfied their energy needs by burning carbon based materials: First wood, then coal, oil and gas. For the longest time this habit did not seem to have any adverse consequences.

Since several decades it is known that emissions of fossil fuel burning machines pollute the air and pose a health risk. Only recently one has realised that meeting the exponentially increasing global energy demand by using fossil fuels increases the amount of carbon-dioxide in the atmosphere resulting in global warming which in turn will cause a noticeable rise in sea levels and extremer weather, for example, more rain storms and longer droughts. Additionally, the amount of fossil fuel stored in the Earth is not endless and mining the remainders will become increasingly difficult, dangerous and cost intensive. Furthermore, a non-negligible amount of the global reserve of fossil fuel is located in countries that are politically unstable, unwilling to share the resources or using them as means for blackmail.

All these considerations combined highlight the need for alternative energy supplies that do not change the environment, pose a health risk or run out in the foreseeable future and that are available to all countries not giving some governments potentially more power because they happen to have a lot of fuel in their ground.

There are a number of alternative energy sources which have been used to cover part of the energy demand in the recent decades and will do so in future. These are solar power, wind power, water power, biomass and nuclear fission. Except for nuclear fission none of the above provides the gross of any country's energy need. Nuclear fission does not produce any carbon-dioxide but has the disadvantage of leaving radioactive waste with half-lives of hundreds of thousands of years potentially causing problems for the coming generations.

There is another way of winning energy which is under research now and has not yet

succeeded in supplying energy: thermonuclear fusion. In fusion, energy is released through merging two elements to form a heavier element. Only light elements (with less than 58 nucleons) are suitable for energy production through fusion. Heavier elements only deliver energy through fission because the binding energy per nucleon in the nucleus has a maximum at around mass number 58 [1]. This is shown in Fig. 1.1.

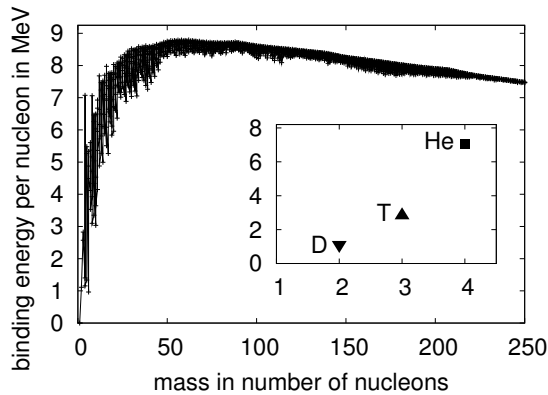


Fig. 1.1: Binding energy per nucleon. At a mass number of around 58 the binding energy per nucleon reaches a maximum. Fusing elements with less mass and splitting elements with more mass releases energy [2].

The binding energy ranges for a given mass number are a result of the isotopes that are included in the graph. The binding energies per nucleon are marked for deuterium, tritium and helium, the fuels and the product of nuclear fusion as it is envisaged as a future energy supply for humanity.

The gained energy is reflected in the mass difference Δm between the fusion fuels and the products. The fusion products have less mass m and the energy gained amounts to $\Delta E = \Delta m c^2$ where c^2 is the speed of light. Specifically, in the future fusion reactors a deuterium ($m = 1875.6 \text{ MeV}/c^2$) and a tritium nucleus ($m = 2808.9 \text{ MeV}/c^2$) are fused to a helium nucleus ($m = 3727.4 \text{ MeV}/c^2$) and a neutron ($m = 939.5 \text{ MeV}/c^2$). Hence, when deuterium and tritium fuse to form helium and a neutron, an energy of 17.6 MeV is released: ${}^2\text{H} + {}^3\text{H} \rightarrow {}^4\text{He} (3.5 \text{ MeV}) + n (14.1 \text{ MeV})$. Since the neutron has only one fourth of the mass of a helium the neutron carries away four times as much kinetic energy as the helium. In a fusion reactor this neutron is caught in a lithium containing blanket in the vessel walls where it gives off its kinetic energy. The resulting heat is used to produce steam which drives turbines for electricity production. Additionally, the neutron undergoes an exothermic nuclear reaction with the lithium-6 and lithium-7 in the wall, thereby creating tritium that is used as fusion fuel: ${}^6\text{Li} + n \rightarrow {}^4\text{He} + {}^3\text{H}$ and ${}^7\text{Li} + n \rightarrow {}^4\text{He} + {}^3\text{H} + n$. In the latter reaction the neutron is preserved and is available

to produce more tritium. On the down side the bombardment with highly energetic neutrons causes considerable damage in the walls.

In the following I will use hydrogen as general term for all hydrogen isotopes.

1.2 Fusion Feasibility

1.2.1 Main Challenges

To get energy from fusion is difficult to achieve. There are a number of challenges that have to be taken on before it can become the energy source of the future.

To maintain fusion a temperature of around 150 Million K in the reactor is required. The hot plasma needs to be confined in a complicated magnetic field which is illustrated in Fig. 1.2.

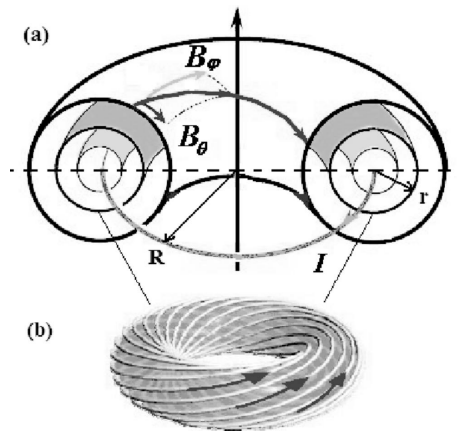


Fig. 1.2: A cartoon illustrating the shape of the magnetic field in a tokamak. Panel (a) shows the nested flux surfaces, panel (b) the way the magnetic field lines are twisted around the torus. Each magnetic flux surface has a different twist, meaning that the B_ϕ and B_θ values are different for each flux surface.

This field possesses a toroidal component B_ϕ created by the coils around the plasma and a poloidal component B_θ created by the induced current I . As result the field lines follow a helical path along the torus. The twist of the field lines varies in the radial direction of the torus. Field lines with the same twist form a magnetic flux surface. This way nested magnetic flux surfaces are created. Furthermore, the plasma has to be kept stable and turbulences have to be controlled. They cannot be suppressed entirely because some turbulence is needed to transport helium and impurities out of the plasma

core. The wall materials of the reactor must be able to withstand the immense power and particle fluxes that are generated. Additionally, walls have to cope with excessive neutron bombardment. Other challenges concern superconducting magnets and the efficient handling of the fuel.

None of the existing tokamak experiments has achieved a positive energy balance. There was always more energy needed to start and sustain fusion than the amount of energy gained from fusion. This can largely be attributed to the heat loss these small machines suffer.

In the next generation fusion experiment ITER [3, 4] one aims at reaching a power amplification of at least ten, that is, the fusion power output is ten or more times higher than the power that is put in to keep the fusion reaction going. The plan is to output around 500 MW. This requires that ITER is about twice as large than the largest existing tokamak JET [5]. Fig. 1.3 shows a drawing of a cut through ITER.

At the bottom of the vacuum vessel of ITER the divertor is located, see Fig. 1.4. Its task is to extract heat and helium - the products of the fusion reaction - and other impurities from the plasma, effectively functioning as an exhaust. To guide the ashes towards the divertor plates the magnetic field lines cross the surface of the material wall.

Consequently, a cut through the magnetic flux surfaces is not a circle but has an oval shape where at one end outside the last closed flux surface the field lines form an X-point and charged particles can leave the confinement. Not only helium and impurities are led to the divertor but all charged particles, also hydrogen. The expected conditions at the divertor surface are listed in Table 1.1.

Table 1.1: Conditions expected at the ITER divertor [6, 7].

hydrogen flux	$10^{24} \text{ m}^{-2} \text{ s}^{-1}$
hydrogen energies	1 - 100 eV
surface temperature	$\approx 1000 \text{ K}$
heat load	10 MW m^{-2}
electron density	10^{21} m^{-3}
neutral particle density	10^{20} m^{-3}

At the divertor surface charged particles collide with the material of the wall and energy is lost through radiation and collisions causing a high heat load on the divertor.

There are two candidate materials for the ITER divertor that may withstand such a heat load: carbon (C) and tungsten (W). Both are planned to be part of the initial divertor configuration in ITER [8].

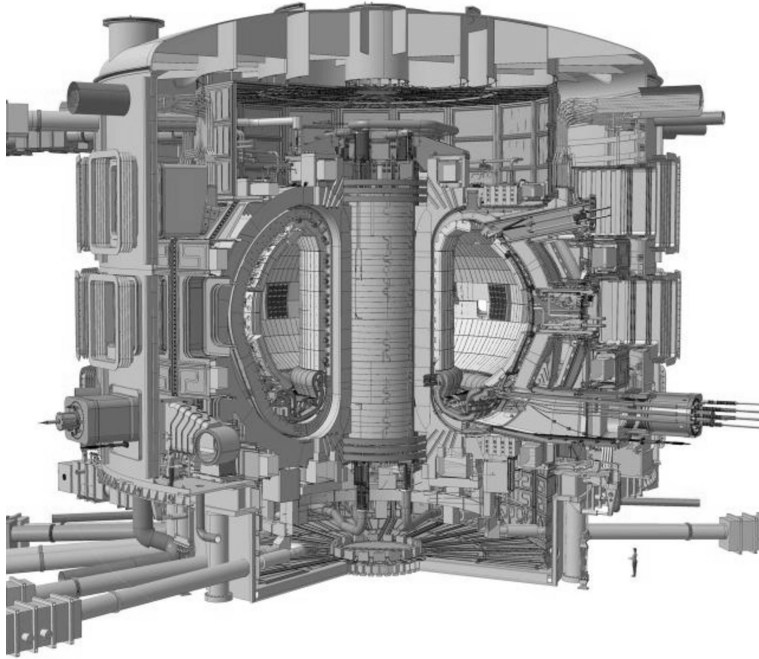


Fig. 1.3: A drawing of ITER, the next generation fusion experiment. Once built and in operation it is expected to reach a power amplification of $Q \geq 10$ and output around 500 MW. The walls of the main chamber will be covered with beryllium, the divertor surfaces at the bottom of the vessel will be partly covered with carbon and partly with tungsten. Picture from the ITER web page [4].

Carbon has the distinct disadvantage that it very willingly reacts chemically with hydrogen, the fusion fuel. This leads to chemical erosion of carbon, dust formation and retention of hydrogen. Through carbon erosion at the surface carbon can enter the plasma in the main chamber where fusion takes place. The carbon is partly ionised and its electrons are added to the plasma. Partly ionised carbon atoms emit line radiation (proportional to Z^{3-4} , with Z as the number of protons in the nucleus which equals the number of electrons in the neutral atom) and - more importantly - the free electrons in the plasma produce Bremsstrahlung (proportional to Z^2) when deflected by nuclei. These radiative losses cool the plasma which can go as far as stopping the fusion reaction. However, carbon is a low- Z element with $Z=6$ and a burning plasma can tolerate a few percent of carbon without stopping fusion.

The hydrocarbons that result from the erosion undergo chemical nucleation, coagula-

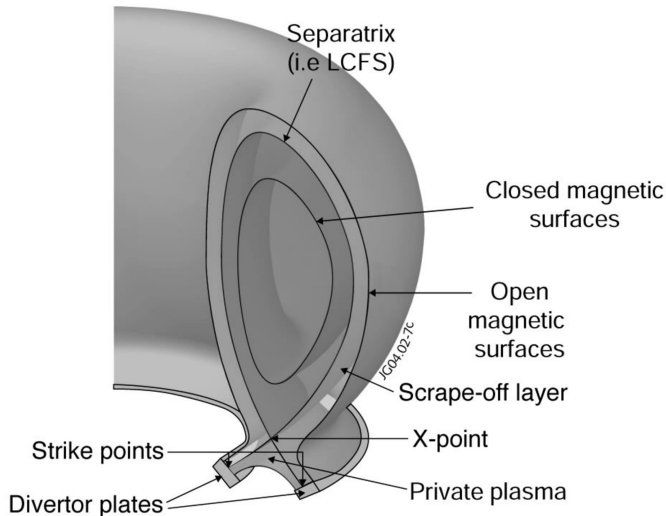


Fig. 1.4: A cut through the torus of the vacuum vessel showing the shape of the magnetic flux surfaces. The magnetic field is constructed such that it allows particles to leave the confinement of the closed magnetic flux surfaces along the X-point or the scrape off layer to the strike point on the divertor surface. Picture from the EFDA web page [5].

tion and attachment of radicals. This way they form larger particles resulting in dust particles ranging in size from less than 100 nm to several mm [9, 10]. The dust contains both deuterium and the radioactive tritium. It tends to creep into every little crack and opening at the most unexpected places and is very hard to remove. Additionally, the hydrogen contained in the dust is unavailable for fusion. The dust radioactively contaminates far corners of the reactor and bears the risk of a dust explosion.

A part of the hydrogen that hits a carbon surface forms chemical bonds with the carbon and is retained in the material. This again leads to loss of fuel. Hydrogen retention is a problem since the amount of radioactive tritium allowed in the reactor at any one time is strictly limited. Obviously one wants all the fuel available for fusion and not caught up in the divertor or scattered about the reactor in the form of dust.

Tungsten does not readily form chemical bonds with hydrogen, so there is no chemical erosion and dust formation. However, hydrogen can enter the tungsten material and diffuse through it. This may lead to hydrogen accumulations under the surface which can result in blister formation. The hydrogen can be returned to the plasma either through cracks or when the blisters burst. Bursting blisters can also transport tungsten

into the plasma. In contrast to carbon, tungsten is a high-Z element with $Z=74$ and therefore knows many line transitions. A few ppm of tungsten in the plasma can cause sufficient cooling through line radiation to stop the fusion process [11].

Additionally, since both materials will erode under the conditions at the divertor, both materials will also be redeposited leading to mixed material surfaces. These mixed materials show different properties than pure carbon or tungsten surfaces.

Neither of the materials is ideal as divertor surface and it is not known how they will actually react under the extreme conditions at the ITER divertor. No experiment so far has been able to recreate all conditions in combination and subject material to them.

1.2.2 Research of Plasma Surface Interactions

General

Apart from their role in the fusion research, plasma surface interactions are important in the medical field where plasma may be used to disinfect surfaces or prepare surfaces of prostheses to make them more acceptable to the human body. Furthermore, plasma surface interactions are important in film deposition or etching.

To research plasma surface interactions one can pursue two different approaches: experiments and computer simulations. Simulations have the advantage that they can concentrate on one physical aspect and the effect of this aspect can be studied isolated from other effects. Furthermore the physical conditions are well-defined. However, creating meaningful simulations that help in gaining insight requires a basic understanding of what is going on. Experiments can help in this. However, in experiments the sum of several phenomena is measured. At times it is difficult to disentangle them and to find out about the fundamental physics.

Both approaches are needed to gain a complete picture. The experiments give a view on the macroscopic events. Simulations can give us an idea of the fundamental processes happening.

Also in the context of fusion research both experiments and simulations are conducted to gain an understanding of the involved processes.

Experiments

Research on plasma wall interactions for fusion typically happens with different types of machines: tokamaks (for example, JET in the UK, and ASDEX in Germany), ion beams and plasma beams (for example, Pilot PSI and MAGNUM at the FOM Rijnhuizen [12]). The exact conditions that occur at the divertor of a tokamak are very much depending on the dimensions of the machine. There are no tokamaks which can recreate the ITER

scenario in a sufficiently exact way to obtain data that can be used to accurately predict what will happen to the divertor surface in ITER. Furthermore, there are no divertors currently installed which have both carbon and tungsten surfaces, the configuration planned for the initial operation of ITER.

A number of the results of tokamaks, plasma and ion beam experiments on carbon erosion under deuterium bombardment have been collected, normalised to a hydrogen energy of 30 eV and compiled into one plot by Roth et al. [13]. The plot suggests that the carbon erosion yield Y , that is, the number of C atoms eroded per impinging H ion, decreases as a function of the hydrogen flux Φ as $Y \propto \Phi^{-0.54}$.

There are no similar experiments for tungsten yet. Only recently a number of plasma beam experiments dedicated to tungsten and tungsten carbide have been conducted. The results show a tendency of tungsten to form blisters which subsequently burst [14, 15, 16, 17]. This mechanism can transport tungsten into the plasma. Measured tungsten erosion yields are in the order of 10^{-3} or less tungsten atoms per hydrogen [18]. There is no study regarding a flux dependency.

Simulations

In the ITER research simulations are conducted on several levels for all tokamak regions. For example, modelling of the plasma dynamics within the closed magnetic flux surfaces, in the scrape-off layer and at the divertor surfaces. Plasma surface interaction simulations are concerned with the divertor surfaces since they - by design - interact the most with the plasma.

As simulation methods molecular dynamics (MD) and Monte Carlo (MC) are the most popular. Examples are ERO a 3D Monte Carlo impurity transport code [19] and HC-PARCAS [20] an MD code simulating chemical interactions. The main difference between them is that MD simulations return information about the dynamics of the system, following each particle's trajectory. MC simulations return information about the statistical behaviour and can handle larger systems and longer time scales since the trajectories are not followed.

The main limitation of simulations of plasma surface interactions are imposed by computer capabilities. Consequently, the size of the simulated system is small and the simulated time is short compared to experiments, in the order of a few nm and not much longer than 100 ns. In experiments typically fluxes of less than $10^{24} \text{m}^{-2} \text{s}^{-1}$ are reached. Simulating these fluxes would require extremely long calculation times. For example, with the computers we used at the Rechenzentrum Garching (see page 113) simulating the bombardment of a sample of $3 \times 3 \times 1.5 \text{ nm}^3$ with a flux of $10^{24} \text{m}^{-2} \text{s}^{-1}$ would require a time span of more than 100 days for one particle impact.

1.2.3 This Work

The studies presented in this thesis use the results of MD simulations in an attempt to shed some light on the behaviour of the candidate divertor materials under the expected extreme conditions.

Most of the aspects of the studies presented here have not been investigated yet. The flux dependency of the carbon erosion yield is one of them, as is the sticking probability of hydrocarbons on surfaces previously subjected to different fluxes. The relatively new implementation of tungsten potentials in an MD code enabled us to investigate carbon erosion and hydrogen retention in mixed tungsten-carbon materials with various carbon percentages.

The remainder of the text is structured as follows:

In chapter 2 the concept and necessary ingredients of molecular dynamics are explained and the used MD code is introduced. This chapter includes some detail about how the simulations are run. Here you will find the measures taken to make the simulations reflect reality as closely as possible, which materials are simulated and how material properties are determined. The following chapters of the thesis contain the individual studies.

The first study verifies that the used MD code returns realistic results for the adsorption of hydrogen on a diamond surface as is predicted by the potential corrected Baule model. The hydrogen energies are between 0.1 and 20 eV and the sample temperatures 700 and 1000 K.

In the next section, both a diamond and an amorphous hydrogenated carbon (a-C:H) surface are bombarded with hydrogen of energies between 1 and 20 eV for different surface temperatures. The bombardment is continued for much longer than in the previous study until a steady state is reached, meaning that the amount of retained hydrogen and the carbon erosion yield do not change anymore under further bombardment. The aim is to determine the differences between the two materials regarding these two quantities.

In the third study the flux dependency of the carbon erosion yield is investigated. The simulations are conducted with an a-C:H sample and mono-energetic hydrogen of 10 eV. The bombardment was done for three different hydrogen flux values. The motivation for this study are experimental results that suggest a decrease of the carbon erosion yield with increasing hydrogen flux [13]. However, in the simulations no flux dependency was found [21].

This lack of flux dependency led to the next set of simulations where the steady state samples of the hydrogen bombardment were bombarded with hydrocarbons to investi-

gate whether the sticking probabilities are depending on the hydrogen flux the sample was subjected to previously. The results suggest that the sticking probability is higher for higher fluxes.

After this we turned our attention to tungsten. Kai Nordlund from the Helsinki University [22] was so friendly to give us a version of the MD code incorporating tungsten-tungsten, tungsten-carbon and tungsten-hydrogen potentials which was made in his group. With this we studied amorphous mixtures of tungsten and carbon as they may appear at the divertor surfaces. We bombarded them with hydrogen and investigated the carbon erosion and blister formation.

Chapter 9 gives conclusions and an outlook.

Chapter 2

Molecular Dynamics

2.1 What is Molecular Dynamics?

In principle all systems where particle interactions are described by a potential can be simulated with the molecular dynamics (MD) method, be the particles galaxies or atoms. Here we concentrate on the simulation of atomic interactions.

2.1.1 Circumventing Schrödinger

Atoms consist of negatively charged electrons and positively charged nuclei. Atoms can have many discrete energy states whose description requires solving the Schrödinger equation. Calculating the exact quantum mechanical expressions is computationally very intensive and already for molecules of only a few atoms currently practically impossible. Therefore a number of approximations need to be invoked enabling us to study larger systems.

The Born-Oppenheimer approximation allows the calculation of the wave-function of a molecule to be split in electronic and nuclear (vibrational, rotational) components. This means that the motions of the fast and slow degrees of freedom are calculated separately. The velocity difference is caused by the factor of ≈ 1800 between the masses of the electron and the proton or neutron. In MD we assume that the cloud of electrons follows the motion of the nucleus instantaneously and we allow only one electronic state which is usually the ground state. Consequently, for each single atom of the same element there is only one potential energy function.

When describing chemical interactions in larger systems, encompassing many atoms, the potentials generated around the individual atoms are depending on the number of bonds, bond angles and bond types, so they are different from the potential generated by an isolated atom. These potentials superimpose and result in the potential energy surface (PES) of the system.

Additionally, it is assumed that the atoms behave as classical particles in a conservative force field whose trajectories are described by Newton's equation of motion.

2.1.2 Newton's Law

The basic assumption is that the atom configuration of the studied system generates a PES. From the potential the force acting on each atom can be determined. This approach enables the calculation of many body systems.

Input to the MD simulations is a set of positions and velocities, one for each atom in the system, and the potential energy function V . Then the new positions and velocities after a given time step are numerically calculated by using $\vec{F} = -\vec{\nabla}V = m\vec{\ddot{r}}$ where \vec{F} is the force exerted on a particle, m is its mass, \vec{r} its position, $\vec{\ddot{r}}$ the acceleration it experiences. The new positions and velocities are input to the calculations of the data at the next time step. Finding the correct description for the potential energy function is the biggest challenge in molecular dynamics.

We want to simulate atoms, so we need to use a potential that recreates the behaviour of chemical bonds and reactions in a sufficiently exact manner that simulation results approach experimental results. This way information can be obtained about events at the atomic level that cause the macroscopic behaviour. A potential modelling chemical interactions is typically attractive on the intermediate range and repulsive on the short range as shown in Fig. 2.1 for carbon-hydrogen interactions and Fig. 2.2 for hydrogen-carbon-tungsten interactions. Furthermore the potential depends on the coordination, the type of atoms, type of bond (for example, single, double, conjugated) and the bond angle. Note that in Fig. 2.2 the WH potential describes the bond between a single W and a single H . On surfaces or in interstitial locations hydrogen can be bound with energies in the order of 1 eV [23].

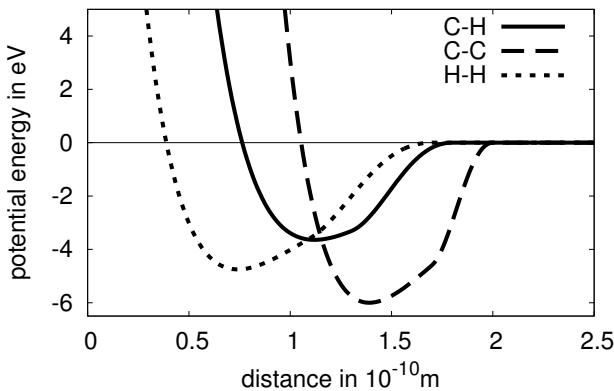


Fig. 2.1: The shape of the Brenner potentials [24]. Note that the CC potential describes a double bond.

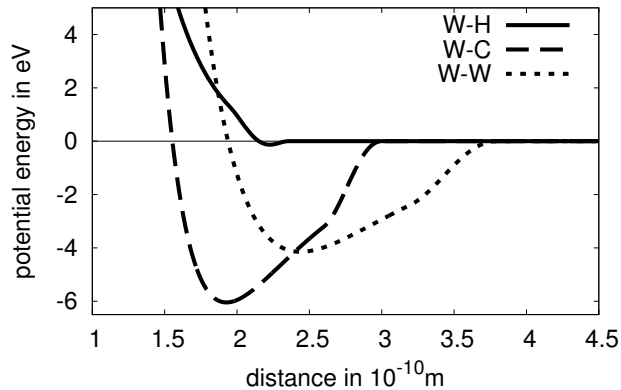


Fig. 2.2: The shape of the Tungsten-Carbon-Hydrogen potentials [22].

The potential energy function is cut off, that means, its value is pulled to zero by a smooth cutoff function, at a distance where the gradient in the potential energy function becomes negligible. Atoms outside the sphere given by the cutoff radius are not considered in the calculation of the potential and the forces. The cutoff distance is depending on the elements that interact and is in the order of 1.5 times the length of the chemical bond.

The potential energy function is not everything that is needed to run MD simulations whose results approach reality. One needs an algorithm to calculate the forces, the sample has to get a temperature and that temperature has to be maintained.

2.1.3 The MD code

For our simulations we used the Hydrocarbon Parallel Cascade (HCPaCas version V3.22) code [20], which calculates the inter-atomic forces in hydrocarbon systems by using the empirical Brenner potential energy function with parameter set II [24, 25] For the simulation of tungsten-carbon-hydrogen systems the code contains potentials developed at the University of Helsinki by Juslin et al. [22].

The attractive and repulsive potentials are Morse type functions, which are limited in range by a smooth cutoff function. The value of the attractive potential is multiplied with a bond order function, correcting it according to bond order, bond angle and bond character.

Brenner Potential

For the simulation of hydrocarbons the Brenner potential [24, 25] is implemented in the MD code and provides an empirical potential energy expression. Originally the potential was designed to simulate the chemical vapour deposition of diamond films. Since then the potential has been used to simulate all sorts of systems involving carbon and hydrogen, from diamond to graphene and nano-tubes and amorphous structures.

Lately it is used in fusion research to investigate the interactions of carbon materials with non-thermal hydrogen. For this simulation purpose the parameter set II is chosen which returns more accurate stretching force constants in exchange for larger bond lengths for the CC-double (3.7%) and triple bond (7.5%).

The inter-atomic potential energy E_b is described by the following sum over the potential energies of all atoms:

$$E_b = \sum_i \sum_{j>i} [V_R(r_{ij}) - \bar{B}_{ij} V_A(r_{ij})] \quad (2.1)$$

where i and j identify the respective atom pair (i, j), V_R is the repulsive component (stemming from the core-core interactions etc.) of the potential and V_A the attractive component (e.g. from valence electrons). \bar{B}_{ij} is the bondorder function correcting the value of the attractive potential according to bond order, bond angle and bond character (radical or part of conjugated system). The attractive and repulsive potentials are expressed as:

$$V_R(r) = f_{ij}(r_{ij}) \frac{D_{ij}}{S_{ij} - 1} e^{-\sqrt{2S_{ij}} \beta_{ij}(r-R_{ij})} \quad (2.2)$$

$$V_A(r) = f_{ij}(r_{ij}) \frac{D_{ij} S_{ij}}{S_{ij} - 1} e^{-\sqrt{2/S_{ij}} \beta_{ij}(r-R_{ij})} \quad (2.3)$$

D_{ij} , R_{ij} , β_{ij} and S_{ij} are fitting parameters depending on the type of atom pair (CC, CH or HH). D_{ij} is the well-depth and R_{ij} is the distance in equilibrium. S_{ij} influences the gradients of the attractive and repulsive components or the forces of attraction and repulsion. f_{ij} is a cutoff function limiting the range of the interactions. It smoothly reduces the interaction potential to zero over a range from $R_{ij}^{(1)}$ to $R_{ij}^{(2)}$. The value of the cutoff function is given by:

$$f_{ij} = \begin{cases} 1 & , r < R_{ij}^{(1)} \\ \frac{1}{2} + \frac{1}{2} \cos \left[\pi \frac{(r-R_{ij}^{(1)})}{R_{ij}^{(1)}-R_{ij}^{(2)}} \right] & , R_{ij}^{(1)} > r > R_{ij}^{(2)} \\ 0 & , r > R_{ij}^{(2)} \end{cases} \quad (2.4)$$

The shape of the Brenner potentials is shown in Fig. 2.1. The center of the atom creating this potential is located at 0 \AA . When an atom comes closer than the cutoff distance it experiences an attractive force following the gradient of the potential into the potential well. If the absolute value of its kinetic energy before interaction is smaller than the absolute value of the energy associated with the depth of the potential well the atom cannot escape the well and is chemically bound. The depth of the potential well gives the bond energy and the distance of the minimum from 0 the nominal bond length. If the kinetic energy of the approaching atom is larger than the binding energy it can escape chemical bonding. If the atoms come too close to each other they are repelled by the positive charge of the nuclei simulated by the steep rise of the potential when approaching 0.

Escaping from the potential well or breaking the chemical bond is achieved through adding kinetic energy in the form of heat or a collision with another atom. The bond can also be broken when a chemically more attractive atom comes along. For example, a hydrogen atom bound to a carbon at the surface of diamond is bound there with an energy of 4.3 eV. If another hydrogen comes along the surface hydrogen may form a bond with it because the bond energy in a hydrogen molecule is 4.5 eV and thus energetically more favourable.

Note that it is not possible to accurately simulate graphite with the current form of the Brenner potential. For one, the van der Waals forces that keep the graphene sheets together are not incorporated in the potential. The other reason is that because of the highly conjugated nature of graphite the interactions between neighbouring atoms are determined by atoms that are further away than the bondorder function takes into account.

W-C-H Potential

The W-C-H potential [22] follows the basic structure of the Brenner potential described in the previous section with the exception of the bond conjugation terms which have been left out in the empirical bond order function \bar{B}_{ij} . The shape of the W-C-H potentials is shown in Fig. 2.2.

Algorithm

The code uses the sixth order Gear algorithm [26, 27, 28] which consists of a predictor and a corrector step. In the predictor step the positions, velocities and higher order time

derivatives up to the fifth order are determined using the Taylor expansion:

$$\begin{aligned}
 r_{1pr}(t + \Delta t) &= r_0 + v_0 \Delta t + a_0 \frac{\Delta t^2}{2} + r_0^{iii} \frac{\Delta t^3}{6} + r_0^{iv} \frac{\Delta t^4}{24} + r_0^v \frac{\Delta t^5}{120} \\
 v_{1pr}(t + \Delta t) &= v_0 + a_0 \Delta t + r_0^{iii} \frac{\Delta t^2}{2} + r_0^{iv} \frac{\Delta t^3}{6} + r_0^v \frac{\Delta t^4}{24} \\
 a_{1pr}(t + \Delta t) &= a_0 + r_0^{iii} \Delta t + r_0^{iv} \frac{\Delta t^2}{2} + r_0^v \frac{\Delta t^3}{6} \\
 r_{1pr}^{iii}(t + \Delta t) &= r_0^{iii} + r_0^{iv} \Delta t + r_0^v \frac{\Delta t^2}{2} \\
 r_{1pr}^{iv}(t + \Delta t) &= r_0^{iv} + r_0^v \Delta t \\
 r_{1pr}^v(t + \Delta t) &= r_0^v
 \end{aligned} \tag{2.5}$$

Then the acceleration $a_{1(V)}$ is calculated from the potential energy function V_1 which was determined using the predicted values:

$$a_{1(V)} = -\frac{\nabla V_1}{m} \tag{2.6}$$

The two values for the acceleration a_{1pr} and $a_{1(V)}$ are generally not the same. The second step, the corrector step improves the values predicted in the first step of the algorithm by adding the difference $\Delta a = a_{1pr} - a_{1(V)}$ multiplied with a weighting factor. For the sixth order Gear algorithm the factors are [28]:

$$\begin{aligned}
 f_0 &= \frac{3}{16}, & f_1 &= \frac{251}{360}, & f_2 &= 1, \\
 f_3 &= \frac{11}{18}, & f_4 &= \frac{1}{6}, & f_5 &= \frac{1}{60}
 \end{aligned} \tag{2.7}$$

The corrector equations look as follows:

$$\begin{aligned}
 r_1(t + \Delta t) &= r_{1pr}(t + \Delta t) + f_0 \Delta a \frac{\Delta t^2}{2} \\
 v_1(t + \Delta t) &= v_{1pr}(t + \Delta t) + f_1 \Delta a \frac{\Delta t}{2} \\
 a_1(t + \Delta t) &= a_{1pr}(t + \Delta t) + f_2 \Delta a \\
 r_1^{iii}(t + \Delta t) &= r_{1pr}^{iii}(t + \Delta t) + f_3 \Delta a \frac{3}{\Delta t} \\
 r_1^{iv}(t + \Delta t) &= r_{1pr}^{iv}(t + \Delta t) + f_4 \Delta a \frac{12}{\Delta t^2} \\
 r_1^v(t + \Delta t) &= r_{1pr}^v(t + \Delta t) + f_5 \Delta a \frac{60}{\Delta t^3}
 \end{aligned} \tag{2.8}$$

This scheme is more complicated than other algorithms, however, this is compensated by its numerical stability. Profiling reveals that the computation times with the sixth order Gear algorithm are not longer than with simpler algorithms, mainly because its numerical stability allows larger time steps [26].

2.1.4 Interpretation of Temperature

Temperature can be interpreted as the kinetic energy of the atomic oscillations in their potential wells. Since in the MD simulations the velocities of all atoms are known and the velocity distribution is a Maxwell-Boltzmann distribution, the temperature T of a sample comprising N atoms can be easily calculated by equating the kinetic energy to the thermal energy:

$$\frac{1}{2} \sum_{i=0}^N m_i v_i^2 = \frac{3}{2} N k_B T$$

$$T = \frac{1}{3 N k_B} \sum_{i=0}^N m_i v_i^2 \quad (2.9)$$

where m_i and v_i are the mass and velocity of the i -th atom.

In an MD simulation of a closed system the total energy should be conserved. The temperature and with it the kinetic energy of the atoms fluctuates. Consequently the potential energy of the system has to fluctuate for compensation.

2.1.5 Thermostat

Eventually we aim at simulating the bombardment of a piece of material with atoms or molecules. This bombardment adds energy to the sample. As mentioned before a sample consists of no more than a few thousand atoms. If we shoot an H atom with an energy of $E=10$ eV at a sample of $N=2000$ atoms and assume that the entire energy is transferred to the sample, each atom gains an energy of $10 \text{ eV}/2000$ which corresponds to a temperature gain of $T = 2E/3Nk_B = 39 \text{ K}$. Considering that a few thousand H atoms need to be shot at the sample to obtain reasonable statistics this rise in temperature has to be prevented.

In real life the heat energy of an impacting H atom is dissipated in the bulk. In MD a thermostat is used to remove excess heat from the sample. The cooling or heating of the sample is achieved by scaling the velocities of selected atoms, such that the desired temperature of the sample is reached. Which atoms the thermostat is applied to is explained below. The temperature controlled atoms lose or gain kinetic energy through the velocity scaling of the thermostat and do not behave physically. Therefore

the thermostat must not be applied to atoms in whose dynamical behaviour we are interested, that is, for example, the atoms in the impact region. Instead, atoms well away from the impact region are temperature controlled and the thermostat's temperature adjustments are conducted to the impact region according to the heat transport properties of the simulated material.

One possible configuration is to apply the thermostat to the border regions and the bottom of the sample, such that the atoms are lying in a sort of "bathtub". Alternatively, the thermostat is only applied to the bottom. In a setup with periodic boundary conditions the latter method may have the disadvantage that heat pulses leaving the sample on one side enter on the other side making it hard to maintain the desired temperature. On the other hand it allows atoms that are not bound and move around in the sample to cross the periodic boundaries without being affected by temperature scaling. So, if atoms are likely to move over the periodic boundaries during the simulation and thereby influence the simulation results the latter setup is recommended. The atoms in the bombarded region can become very hot. Bonds between hot atoms and artificially kept cool atoms of the thermostated region can become overstretched or even broken. To avoid this a buffer zone is introduced. The atoms in the buffer zone are neither bombarded nor temperature controlled. Therefore they are not likely to be very hot thus preventing the overstretching or breaking of bonds. Both configurations are shown in Fig. 2.3.

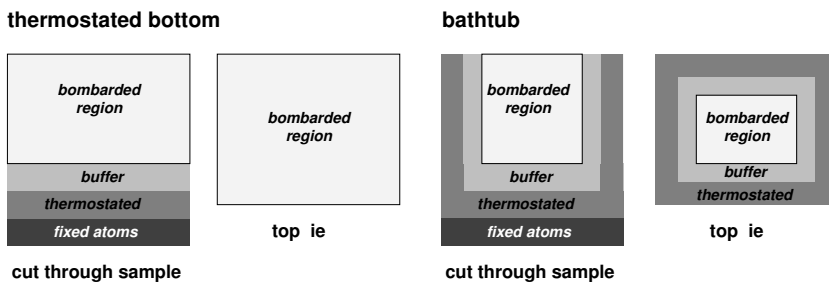


Fig. 2.3: Illustration of the thermostat configurations. The configuration with the thermostated bottom is shown in the two pictures to the left and the "bathtub" configuration in the two pictures to the right. A cut in z-direction through the sample and the top view is shown. Between the temperature controlled region and the bombarded region a buffer zone is located to avoid overstretching or breaking of bonds. The fixed atoms prevent the sample from moving under bombardment.

The thermostated region acts like a chunk of material where kinetic energy is dissipated. This is visualised in Fig. 2.4. The impact of an H atom sends a spherical heat wave through the material. The energy degrades with $1/r^2$ where r is the distance from

the impact site. When the heat wave hits the thermostated region energy is removed by scaling down the velocities of the atoms in that region and the energy decay happens faster than $1/r^2$. At the end of the thermostated region the heat energy is at a level that corresponds to the level of an undisturbed heat wave that has travelled a distance of Δr further. This does not effectively increase the bombarded surface and decrease the flux in a bombardment simulation, see section 2.1.8.

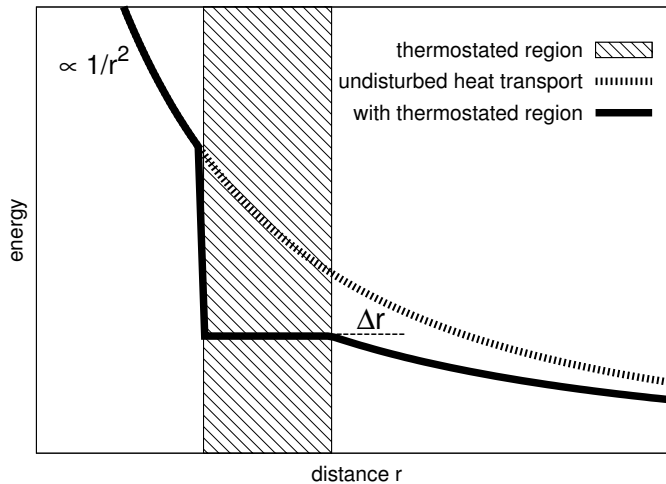


Fig. 2.4: Illustration of how the thermostated region simulates a chunk of material by removing kinetic energy from the atoms. Explanation, see text.

In our simulations the Berendsen heat bath [29] is used for temperature control. It works by multiplying the velocities of the atoms in the thermostated regions with the following factor λ :

$$\lambda = \sqrt{1 + \frac{\Delta t}{\tau} \left(\frac{T_0}{T} - 1 \right)} \quad (2.10)$$

where T_0 is the desired temperature and T is the actual temperature of the sample as determined by Eqn. 2.9. The τ is the rise time of the thermostat determining how fast the system is forced to the desired temperature value. The scaling with λ results in an exponential temperature reduction in the temperature controlled region, see Fig. 2.5. During simulations the temperature T which is input to the velocity scaling should be measured for the region of the non-temperature controlled atoms.

It was mentioned before that the Berendsen thermostat does not recreate temperature fluctuations in a physical way. One rather dramatic result of this is the so-called

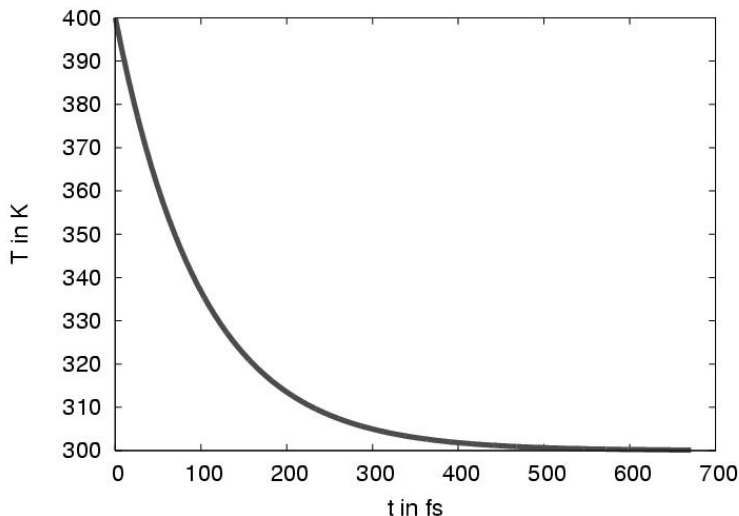


Fig. 2.5: Plot of the exponential temperature decrease resulting from scaling the velocities with factor λ of Eqn. 2.10 and $\tau = 100$ fs in the Berendsen thermostated region.

“flying ice cube” effect. The thermostat has a dampening effect on the thermal oscillations gradually decreasing their frequency. This can go so far that thermal motion is transformed into translational motion. Hence the simulated sample loses its thermal oscillations, meaning that it cools down, but gains momentum and starts “flying”. This has been described by Harvey et al. [30].

2.1.6 Bulk Simulation

One requirement for the simulation of a material surface is that from an atom’s point of view the surface is infinite. This is achieved by applying periodic boundary conditions in two dimensions.

Furthermore, the sample should be immobile. The momentum exerted by a hydrogen plasma on the targets in ion beam experiments or on divertor plates in tokamaks is not sufficient to move them. In our simulations are therefore all velocity components of the atoms at the bottom of the simulated sample fixed to zero during the whole duration of the simulation. A thickness of approximately 2 monolayers is sufficient for the fixed region. It is a good idea to apply temperature control to the atoms neighbouring the fixed atoms to avoid excessive stretching or even breaking of the bonds between fixed and non-fixed atoms.

Additionally, we want the sample to have a temperature. From Eqn. (2.9) we can determine the mean velocity of the atoms. Initially velocities are assigned from a Gaussian distribution around this average value. The velocities should add up to zero to avoid giving the sample momentum.

2.1.7 Sample Creation

The creation of a stable sample is an art and a hobby in its own right. Starting from the desired composition of the material one has to decide on the dimensions of the sample. Here one needs to find a balance between the calculation time which encourages small samples and - for bombardment simulations - the thickness required to avoid that the projectile shoots cleanly through the sample. A common way to determine the required thickness is to use the TRIM/SRIM (Transport of Ions in Matter/Stopping and Range of Ions in Solids) software package [31]. It calculates quickly the stopping and range of energetic ions in matter.

Once the thickness is determined one has to bring the sample in thermal equilibrium. First the periodic boundary conditions are set in all three dimensions and none of the atoms in the sample is fixed. Then the Berendsen thermostat is applied to all atoms performing annealing of the sample, that is, heating to a high temperature (typically the melting point or beyond) with subsequent cooling. This treatment enables the atoms to find a configuration of minimal potential energy and hence a stable configuration. Several cycles of annealing and cooling should be applied. Then the sample can be brought to the desired simulation temperature. After this the thermostat is switched off and the temperature fluctuations should not be larger than a few percent.

The next step is to “take off the lid”, meaning that the periodic boundary condition in one direction is removed and the atoms in the bottom of the sample are fixed. If the process was successful the sample is stable and not falling apart. After letting the sample rest for approximately a nanosecond the thermostat in the desired configuration (“bathtub” or a layer over the fixed atoms only) can be applied and the bombardment simulation can begin.

2.1.8 Bombardment Simulation

Projectile Positioning

When simulating the bombardment of a surface with particles the initial position of the projectile needs to be far enough above the surface that there is no interaction between the projectile and the surface atoms. This can be achieved by placing it more than one cutoff length above the highest surface atom. Next an initial velocity and direction are

assigned to the projectile.

Assuming the surface normal is the z-direction, then the x and y positions of the subsequent projectiles have to be varied randomly to avoid shooting at the same spot over and over again.

Thermostat configuration

If the thermostat configuration is the “bathtub” the temperature controlled atoms at the surface should not be bombarded. As explained in section 2.1.5 the bombarded region should not touch the thermostated region but is by approximately one atom-diameter removed from it. The buffer zone prevents the overstretching or even breaking of bonds between hot atoms that interacted with the projectile and cold atoms in the thermostated region. The configurations are illustrated in Fig. 2.3 which shows a top view and a cross section of the sample where the different regions are indicated.

Sample Dimensions

For the choice of sample size the following has to be taken into account:

The sample should be small enough to minimise needed computer time. Assuming periodic boundary conditions in x- and y-direction the lower limits for x and y are given by the implementation of the periodic boundary conditions in the code which does not allow cells smaller than twice the cutoff radius. This is to prevent atoms interacting with themselves over periodic boundaries.

The thickness in z-direction of the bombarded region needs to be large enough to accommodate the penetration depth of the projectiles. One does not want a large number of the projectiles ending up in the thermostated region as this changes the dynamics of the added atoms in the sample and the sample atoms. If the sample is much too thin most projectiles will push through into the fixed region where they may get stuck or fly through exiting the sample at the bottom. This need not be a problem if one is only interested in surface top layer effects as erosion. It is not desirable if one wants to learn about retention.

Particle Flux

The instantaneous flux Φ of the incoming particles is determined by the area A that is bombarded and the time span t_{run} between impinging projectiles:

$$\Phi = \frac{1}{A t_{run}} . \quad (2.11)$$

In the simulations the time t_{run} between the projectile impacts can be chosen either

constant or randomly distributed, for example, as in a Poisson distribution:

$$t_{\text{run}} = -\log(x) \langle t_{\text{run}} \rangle \quad (2.12)$$

where x a random number between 0 and 1 and $\langle t_{\text{run}} \rangle$ the mean time span between projectile impacts. Running bombardment simulations with both fixed $t_{0_{\text{run}}}$ and t_{run} from a distribution around the mean value $\langle t_{\text{run}} \rangle = t_{0_{\text{run}}}$ yields the same results, assuming that near simultaneous impacts at the same location are very unlikely. Consequently, one can stick to the constant time interval between projectile impacts.

Angle of Incidence

Another variable in the bombardment of samples is the angle of incidence with which the projectile hits the surface.

One needs to distinguish two cases: either the projectile energy is higher or lower than the physical sputtering threshold. Physical sputtering occurs when the kinetic energy of the projectile is large enough to remove atoms from the material by breaking bonds.

In the case of physical sputtering bombardment with an angle other than 0 from the surface normal the sputtered atom experiences an acceleration parallel to the surface which facilitates its escape from the surface. This is expected to result in larger yields with increasing angle of incidence [32].

For lower energies erosion can only take place through chemical erosion. Here the projectile forms a chemical bond with a surface atom. This may lead to a situation where the surface atom is no longer bound to the bulk of the material and is carried off into the gas phase. This type of erosion is hardly affected by the momentum transfer. The determining factor is that a larger angle of incidence leads to a lower penetration depth which is likely to have the same effect as bombardment with a lower energy and hence lower erosion yields.

Furthermore, in the context of the ITER divertor exposure to plasma, the potential drop formed by the plasma - the sheath potential - at the divertor surface accelerates positively charged ions towards the surface. The magnetic field lines form a small angle with the divertor surface [8]. Ions move around field lines along spiral-shaped trajectories. Most of them feel the effect of the sheath potential when they are in the part of the trajectory that moves towards the surface. Consequently, their velocity component parallel to the surface is small. Hence their incidence angle on the divertor surface is close to the surface normal. Therefore, for this work, the simulation of a normal angle of incidence is considered sufficient.

2.1.9 Determining Material Properties

Apart from the easily calculated density and composition of the material (e.g. atomic percentage of hydrogen and carbon) there are properties connected to the heat transport that can be determined from the MD simulations. This is interesting because heat has to be conducted from the impact site to the temperature controlled regions of the simulated sample. The quantities specific heat at constant pressure c_P , thermal conductivity k and the thermal diffusivity α should be close to the values measured in experiments.

The thermal conductivity k is a measure for the ability of the material to conduct heat and the thermal diffusivity α gives the rate at which heat is conducted through a medium. They are defined as follows:

$$k = \frac{\Delta Q}{\Delta t A} \frac{l}{\Delta T} \quad (2.13)$$

$$\alpha = \frac{k}{\rho c_P} \quad (2.14)$$

with ΔQ the heat, Δt time, A the surface, l the length over which ΔT applies and ρ the mass density. The quotient $\Delta Q/(\Delta t A)$ is equal to the product of particle flux Φ and particle energy E .

To determine the specific heat c_P of the simulated sample we can use two different approaches: firstly, by using the definition of c_P as the heat energy required to increase the temperature of 1 kg material by 1 K and secondly, by calculating c_P from enthalpy fluctuations.

For the first method the specific heat c_P can be expressed as:

$$c_P = \frac{\Delta E}{\Delta T m} \quad (2.15)$$

with ΔE as heat energy, ΔT as temperature and m as mass. The quotient of ΔE over ΔT is found by bombarding a thermalised sample with the thermostat switched off. From this we can determine the amount of energy ΔE that has been added to the sample. ΔT is given by the temperature rise during the same time. For a given temperature (c_P is a function of the temperature) the quotient ΔE over ΔT can now be determined. The mass is given by the non-fixed atoms of the sample and with (2.15) the specific heat can be calculated.

The other way of determining c_P is using enthalpy fluctuations. The specific heat at

any temperature can be written as [33, 34]:

$$c_P = \frac{\langle H^2 \rangle - \langle H \rangle^2}{mk_B T^2} \quad (2.16)$$

where H is the enthalpy, m the mass, T the temperature of the sample and k_B the Boltzmann constant. The enthalpy H is defined by $H = U + pV$ with U as the internal energy, p the pressure and V the volume. Since the pressure in the system is very small the second expression pV is much smaller than the internal energy U . The quantity U is an output of the simulations, therefore $H = U$ is used in the actual calculation of c_P . The mean of the enthalpy and the mean square enthalpy can be determined from a simulation of a sample in thermal equilibrium at the desired temperature.

The two values determined with Eqn. 2.15 and Eqn. 2.16 should be similar.

2.1.10 Limitations

The main limitation of MD is the needed computation time. Conducting MD simulations is attractive because dynamical processes can be resolved. This is achieved by calculating the forces acting on each atom in the model system for each time step. This requires that the time step is short enough to resolve the typical lattice vibrations of about 10^{13} Hz. If there are particles with high velocities in the model system the time might have to be even shorter to properly sample the motion of fast particles. Obviously, the more time steps are required the longer the simulation will last. If bombardment is to be simulated the energy of the projectile dictates a minimum sample thickness to avoid interactions of the projectile with the thermostated region or even exiting of the projectile at the sample bottom. Taking all these considerations into account the simulated time is typically in the order of nanoseconds for a sample of a few thousand atoms. Hence, effects that take considerably longer are not included in the simulation results, examples are diffusion, full relaxation of a surface and low particle fluxes.

Furthermore MD does not take particle charges into account. In many simulations of subjecting a surface to a plasma beam one talks about ions, this is strictly speaking not correct. MD only knows neutral particles whose interactions are determined by the potential. However, by assuming that ions recombine to neutrals before they start interacting with the surface atoms, the use of MD to study plasma surface interactions can be justified. The recombination takes place through Auger and resonance neutralisation. Studies show that these take place on metal and graphite surfaces [35, 36] facilitated by the dislocated electrons of these materials. Since the potential drop that forms at the plasma wall interface creates an electron surplus one can assume that the ions from the plasma are neutralised before interacting with the surface.

Another related effect that is not directly simulated is the effect of electronic stopping. It occurs in metallic substances where the valence electrons form a cloud that interacts with projectiles. The moving particle loses energy through ionisation or atomic excitation. The mean energy loss the particle experiences is described by the Bethe formula for the stopping power $S(E) = -dE/dx$ with E as energy and x as travelled distance. The stopping power in the non-relativistic regime is proportional to $\ln(v)/v^2$ with v the velocity which results in a maximum at the energy where the particle becomes so fast that interaction with the material becomes less likely.

The effect is simulated with the help of precomputed tables listing the projectile velocity and the corresponding stopping power in the sample material. The stopping power is subtracted from the projectile's energy while moving through the sample.

Fig. 2.6 shows the stopping power a deuterium experiences in tungsten carbide with 15, 50 and 95% carbon contents as a function of the deuterium's kinetic energy. One clearly sees the typical shape with a maximum energy loss at around 10^5 eV.

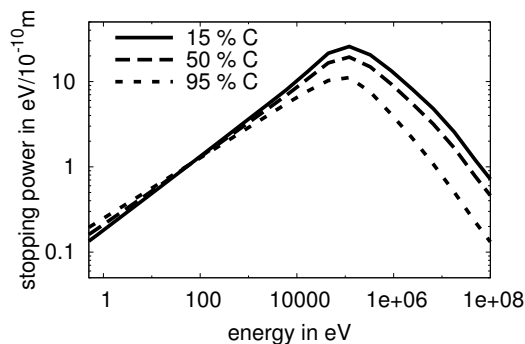


Fig. 2.6: Stopping power a deuterium experiences in tungsten carbide with different carbon contents as a function of the deuterium's kinetic energy [31].

The composition of the material plays a role particularly for high particle energies of more than 10 keV, the electronic stopping power is proportional to the amount of metal in the material.

Nuclear stopping is another process that slows down a moving ion in a solid. It is caused by interactions between the ion and the atoms. The simulation of this effect is already included in the shape of the potential energy function. Nuclear stopping plays a role only at low particle energies.

Chapter 3

Overview of the Studies

This chapter gives an overview of the studies that are described in detail in chapters 4 to 8. The conducted MD simulations comprise the following subjects:

Sticking Probability of Hydrogen on Diamond (*Chapter 4*)

The sticking of hydrogen on a {111} diamond surface is investigated using MD simulations. The hydrogen energy ranges from 0.1 to 20 eV and the surface temperatures are 300 and 1000 K. The simulations cover the first 200 H atom impacts during cumulative bombardment. Saturation of the diamond surface with hydrogen is not reached.

The results show that the hydrogen sticking probability has a minimum at the H atom energy where the transition from surface interaction to surface penetration takes place. In our simulations surface penetration of hydrogen in diamond occurred at around 7 eV. This value agrees very well with the predicted 7.9 eV of the potential corrected Baule model describing binary collisions [37]. In the simulations less hydrogen sticks to the hot sample than to the cool one which is in agreement with experiments [38].

This study shows that the MD simulations recreate the sticking behaviour as expected.

Comparing diamond and amorphous hydrogenated carbon (*Chapter 5*)

One has only recently started to study diamond as material for the divertor plates in ITER [39]. Currently the preference goes out to carbon fiber composite (CFC) materials. This material has been experimented with in existing tokamaks and linear plasma beam devices. After some exposure to hydrogen CFC turns into amorphous hydrogenated carbon (a-C:H). This fate is predestined for all carbon materials including diamond. The transformation to a-C:H is caused by chemical binding of impinging hydrogen to the surface and inside the sample. Additionally, redeposition of eroded hydrocarbons back onto the surface forms an a-C:H layer on the surface. In this study a diamond and an a-C:H sample are bombarded with hydrogen until a steady state is reached, that is, the erosion yield and amount of retained hydrogen reach a steady state.

The results show that the diamond sample retains more hydrogen than the a-C:H sample. For diamond the retained amount does not depend from the temperature, for a-C:H

the amount of retained hydrogen drops with the temperature. On the other hand the carbon erosion yields obtained from diamond are clearly lower than those from a-C:H.

Amorphous Hydrogenated Carbon under high Hydrogen Fluxes [21] (Chapter 6)

This section treats the flux dependency of the carbon erosion yield and the hydrogen enrichment of the surface in the high flux regime at 10^{28} ions per m^2s and higher. An a-C:H sample is exposed to high flux hydrogen bombardment with a hydrogen energy of 10 eV at surface temperatures of 700 and 1000 K. The simulation results show that the carbon erosion yield is higher for higher sample temperatures but does not show a strong dependency on the hydrogen flux. Hence, the hydrogen enrichment in the upper surface layer observed in the simulations most likely does not contribute to the erosion yield reduction in the experiments. Furthermore, the composition of the eroded material shows a slight increase in CH, C₂H and C₂H₂ for higher fluxes, whereas species with more hydrogen, C atoms and C₂ are decreased. However, the H:C ratio in the eroded material shows no flux dependency.

Redeposition of Hydrocarbons on Amorphous Hydrogenated Carbon (Chapter 7)

Redeposition is one of the effects that form a-C:H layers on divertor plates and targets in linear plasma beam devices. It is one of the candidates for reducing the carbon erosion yield when the hydrogen flux is increased. That is, there may be a flux dependency of the amount of material redeposited on the surfaces. To investigate this idea, the steady state samples of the bombardment simulations in the previous study were subjected to bombardment with hydrocarbons and the sticking probability determined as function of the flux the sample was subjected to in the previous simulations.

The results show that the structure of the bombarded sample in terms of sp^2/sp^3 ratio and the porosity play a significant role in the sticking probability of hydrocarbons. Both factors are determined by the history of the sample.

Tungsten Carbide under Hydrogen Bombardment (Chapter 8)

The current design plans for ITER foresee a divertor with carbon as well as tungsten plates. During operation some of both materials will get eroded transported into the plasma and subsequently redeposited on the divertor plates. This leads to mixed material surfaces. This study investigates the behaviour of amorphous tungsten carbide samples with different carbon percentages under 100 eV deuterium bombardment.

Results show that especially the 50% carbon sample is prone to blister formation where deuterium gas accumulates below the surface. The deuterium is returned to the gas phase either through gradual out-gassing or through bursting of the blister where tungsten and carbon material is separated from the bulk and eroded.

Chapter 4

Sticking Probability of Hydrogen on Diamond

4.1 Introduction

Experiences with fusion reactor experiments and theoretical studies have shown that hydrogen is retained in the carbon surfaces of the divertor. In previous MD simulations the hydrogen contents of carbon reaches more than 50% and for higher projectile energies more hydrogen sticks [40]. This is in agreement with experiments, which additionally showed that hot material retains less hydrogen than cold material [38].

In this study we present the results of MD simulations of a diamond {111} surface with temperatures of 300 and 1000 K exposed to hydrogen atoms with energies ranging from 0.1 to 20 eV. The aim is to study the amount of retained hydrogen after the first 20 and after the first 200 H atom impacts.

The results of the simulations include the dependencies on the sample temperature and on the H atom energy. We start the simulations with a pure diamond sample which is cumulatively bombarded with H atoms. The angle of incidence is normal to the sample surface. Varying the incidence angle is not expected to change the results since the projectile energy lies below the physical sputtering energy of about 30 eV and only chemical erosion plays a role, see section 2.1.8.

Hydrogen saturation is not reached and the hydrogen contents of the diamond is still increasing after the simulated 200 shots.

4.2 Modelling

The MD code we used for our simulations is described in section 2.1.3.

The model system consists of a diamond {111} block of the size $25.3 \times 26.3 \times 18.6 \text{ \AA}^3$. This corresponds to 2160 C-atoms in 18 layers of 120 atoms each. This is shown in Fig. 4.1.

The boundaries are periodic in two dimensions to simulate an infinite surface. The two

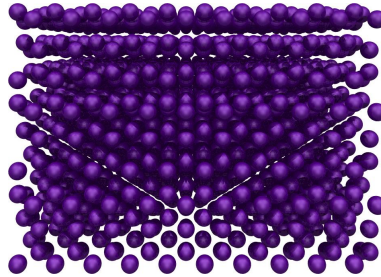


Fig. 4.1: The initial sample for the simulations. One clearly sees the layers of carbon atoms in the diamond $\{111\}$ configuration.

bottom layers have a fixed zero velocity to avoid motion of the sample. The entire initial sample consisting of pure carbon is heated to the desired temperature until thermal equilibrium is reached. The simulated temperatures are 300 and 1000 K. The sample is then cumulatively bombarded with H atoms of energies between 0.1 and 20 eV and of normal incidence. During the simulation the “bathtub” configuration of the thermostat as described in section 2.1.5 is applied. The rise times are 100 and 200 fs. Thermostated regions are not bombarded. For each combination of temperature and H energy the sample is cumulatively bombarded with 200 H atoms in four different runs (two per rise time). The time intervals between hydrogen impacts are fixed to 127 fs which corresponds to a flux of about $10^{30} \text{m}^{-2} \text{s}^{-1}$.

4.3 Results

The presented results are the average values and their standard deviations found from the four simulation runs performed for each combination of temperature and H energy.

In the following, all H atoms which are either bound to the sample’s surface or trapped inside the sample bulk are considered to be retained.

Two different basic processes can be distinguished: a) the interaction of a projectile with surface atoms resulting in chemisorption or reflection and b) the penetration of the surface by a projectile where the particle is absorbed into the sample. The former happens for low projectile energies, the latter for high energies.

In Fig. 4.2 images of the samples at 300 K after the bombardment with 200 H atoms are shown. One can see that with increasing H energy the surface gets more disturbed and that H atoms penetrate deeper into the sample.

In Fig. 4.3 the number of retained H atoms is shown as function of the sample depth after 200 H have been shot. The bin width is 0.5 \AA and the top layer is about 1 \AA thick. The binning is such that H atoms that are bound to a C atom of the surface top layer

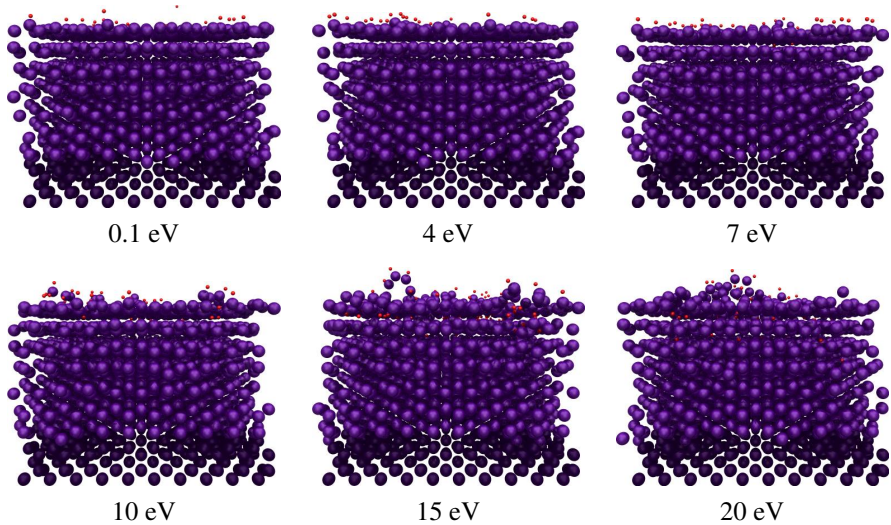


Fig. 4.2: The diamond samples after 200 H shots of energies of 0.1, 4, 7, 10, 15 and 20 eV at 300 K sample temperature. The blue spheres symbolise carbon atoms, the red ones hydrogen. The darker blue atoms at the bottom are fixed.

and reside above the other C atoms of the top layer are in the bin at depth 0. The bond length between an H and a C atom is about 1.1 Å and between two C atoms in diamond about 1.5 Å. This means that H atoms up to 2 Å depths in the plots have not penetrated the surface top layer. Bearing this in mind one sees that for both temperatures the H atoms need at least 7 eV to push through the surface top layer and reach a depth where they can form bonds with atoms that are not part of the top layer.

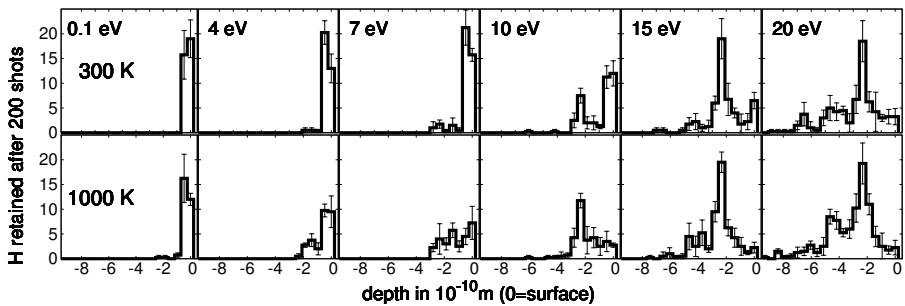


Fig. 4.3: The depth distribution of H atoms of various energies in the diamond sample after 200 shots. The top row shows the sample at 300 K the bottom one at 1000 K. Depth 0 corresponds to the hydrogen atoms residing on the top of the diamond surface. The bin width is 0.5 Å.

In the sample of 300 K the H atoms prefer to bind to the top layer C atoms even for H energies as high as 10 eV. The hotter sample retains H atoms preferably deeper in the sample. The H atoms can penetrate the hot sample easier due to the thermal motion of the sample atoms which temporarily form larger gaps. This effect makes diffusion through the 1000 K sample easier. This goes for both directions: into the sample and out of it. Hence - compared to the 300 K sample - we find less hydrogen close to the top layer but more hydrogen at larger depths in the hotter sample.

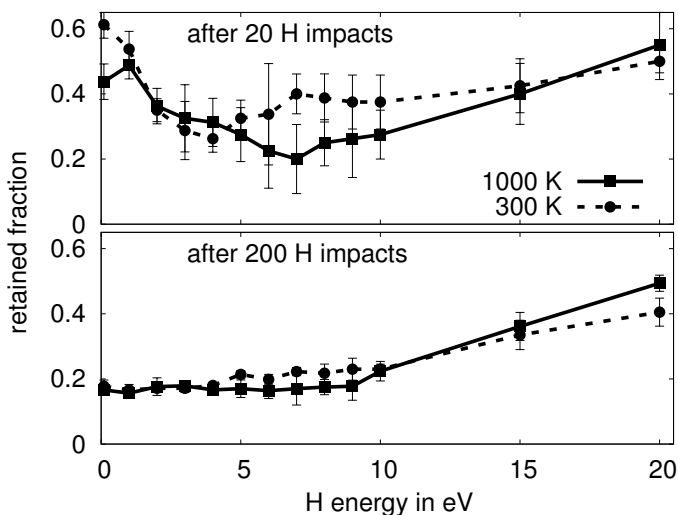


Fig. 4.4: The sticking probability of hydrogen atoms on a $\{111\}$ diamond surface after a bombardment with 20 H atoms (top) and with 200 H atoms (bottom).

Fig. 4.4 shows the retained fraction of the shot hydrogen after 20 and after 200 shots. The retained fraction is the ratio between the number of retained H atoms to the total number of H atoms which were shot at the sample. It is plotted as a function of the H atom energy and for different sample temperatures.

After 20 H atoms were shot the retained fraction shows a distinct shape where we distinguish three regions:

- Below about 1 eV the retained fraction drops for the 300 K sample but rises for the 1000 K one.
- Above 1 eV projectile energy the retained fraction decreases until about 4 eV for the 300 K sample and until about 7 eV for the 1000 K sample.
- For impact energies higher than 4 eV the retained fraction remains constant for the 300 K sample slightly rising for energies above 10 eV. For the 1000 K sample the retained fraction rises monotonically for projectile energies above 7 eV.

This can be explained as follows:

Thermal H atoms with energies of less than 1 eV need to encounter a dangling bond to be chemisorbed on the surface otherwise they are reflected away from the surface. Material of higher temperatures generally retains less hydrogen which explains the lower retained fraction for the 1000 K sample at 0.1 eV even though the effect is not very strong in diamond (see chapter 5). Therefore one would expect that the retained fraction in the 1000 K sample remains below the one of the 300 K sample.

However, for projectile energies of about 1 eV one can observe H atoms bound to C atoms of the second layer and sitting between the C atoms of the top layer. This is illustrated in Fig. 4.5.

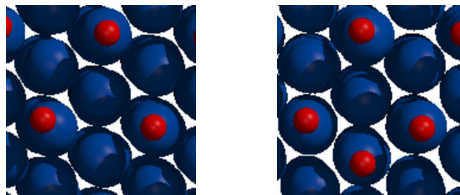


Fig. 4.5: The view on a few atoms on the surface of a 111 diamond. The blue spheres symbolise carbon atoms, the red ones hydrogen. To the left three hydrogen atoms are bound to C atoms that had dangling bonds in the initial {111} diamond surface. The C atoms with dangling bonds are located slightly higher at the surface as can be seen in Fig. 4.1. Thermal hydrogen atoms preferably bind to these sites. If the H projectile has an energy of about 1 eV it can create its own binding site on a C atom. This is shown to the right where a fourth H atom is bound to a C atom which did not have a dangling bond in the initial configuration.

Apparently H atoms with energies of about 1 eV have enough energy to create their own binding site. Particularly in the surface top layer where the C atoms have a dangling bond some CC double bonds may be present. This is promoted by a higher temperature. These double bonds like to break in the presence of hydrogen. In the process another dangling bond is created which can accommodate another H atom. This way the amount of retained hydrogen in the 1000 K sample reaches the same level as the 300 K sample.

For higher H energies the retained fraction drops and has a minimum around 4 eV for the 300 K sample and around 7 eV for 1000 K.

The drop can be understood with the potential corrected Baule model [37, 41]. The model is based on momentum and energy conservation in a collision of two hard

spheres with the addition of taking into account the binding potential. According to this model the maximum amount of energy ΔE an atom of mass m and initial energy E_i can lose in a collision with another atom of mass M is given by

$$\Delta E = \frac{4mM}{(m + M)^2} (E_i + E_b) \quad (4.1)$$

where E_b is the binding energy between the two atoms. For a collision between an H and a C atom with $E_b = 4.3$ eV this results in $\Delta E = 0.3E_i + 1.2$ eV. The minimum energy after the collision is given by $E_f = E_i - \Delta E$ resulting in $E_f = 0.7E_i - 1.2$ eV. When setting $E_f = 0$ one finds that atoms with an energy of less than about 1.7 eV can lose all their energy in the collision. If there are dangling bonds available these atoms are chemisorbed. H atoms with higher energies have energy left after the collision and can scatter away from the surface. Hence, the sticking probability drops as the H atom energy rises. The sticking probability reaches a minimum if the energy the H atom has left after the collision is too high to allow chemisorption but too low to penetrate the surface. For H-energies where the energy after the collision exceeds the binding energy of the C-H bond the H atom has enough energy left to penetrate the surface layer. Inside the sample it continues to lose energy and gets trapped resulting in an increase of the sticking probability with increasing H-energy. In our simulations surface penetration occurs for H atom energies of around 7 eV and higher which agrees well with the energy $E_i (E_f = 4.3 \text{ eV}) = 7.9$ eV predicted by the Baule model.

For the 1000 K sample the sticking probability drops monotonically until 7 eV. The minimum of the sticking probability on the 300 K sample stretches over a range of 3 eV from 4 eV to 7 eV. This is a temperature effect where for the cooler sample the H atoms cannot easily penetrate the surface and hence stay at the surface, see Fig. 4.3 and the discussion around it. Consequently, the surface coverage increases faster on the 300 K sample than on the hotter sample.

Above an energy of 7 eV the H atoms are able to penetrate the surface top layer and get lodged beneath the surface. With increasing energy the penetration depths increases and the hydrogen gets more effectively trapped. Hence the increase of the retained fraction.

The discussed effects below 7 eV are not visible anymore after 200 H shots where the sticking probability is more or less constant until 9 or 10 eV. This is a consequence of the increasing surface coverage which results in a decrease of the sticking probability [42].

The differences in retained hydrogen fraction for the different samples are very small. Experimental results show that hot carbon material can retain less hydrogen than cooler material [38]. One would expect the same result from the MD simulations. How-

ever, one need to bear in mind that after 200 hydrogen shots the system is still far from equilibrium. In chapter 5 the bombardment of the diamond surface is continued until a steady state is reached. Then the temperature effect shows as expected.

4.4 Conclusions

We conducted MD simulations of a carbon sample with temperatures of 300 and 1000 K which is bombarded with H atoms of energies from 0.1 to 20 eV. We examined the amount of hydrogen that is retained in the sample after 20 and after 200 H shots.

The results of the MD simulations after 20 shots show that the sticking probability is lower on surfaces with high temperatures. Consequently the surface coverage increases faster for cooler samples. This temperature effect disappears after 200 H shots. The reason is probably that the system is still far from equilibrium. In simulations of steady state systems the temperature effect is reproduced, see chapter 5.

The simulation results after 20 H shots show a minimum of the hydrogen retained fraction between 4 and 7 eV of H atom energy. The decrease of the retained fraction is explained by the potential corrected Baule model which describes the energy loss in a collision based on momentum and energy conservation taking into account the binding energy between two atoms. The drop is less pronounced for lower temperatures because the surface coverage increases faster than for hotter surfaces.

After 200 H shots the fraction of retained H atoms increases steadily for energies higher than 7 eV. At an H energy of 7 eV the transition from surface interactions to penetration of the surface by the H atoms takes place. Hence, not only the top surface layer is available to hold H atoms but additionally the layers underneath. The larger the energy of the incoming H atom the more sites to accommodate it in the sample are available.

Chapter 5

Diamond and Amorphous Hydrogenated Carbon Compared

5.1 Introduction

Carbon material comes in many flavours, for example, as diamond where all carbon atoms are sp^3 hybridised which means that they are chemically bound to four other atoms and all of these bonds are single bonds. A C atom can have other hybridisations, namely sp^2 in a CC double bond and sp in a CC triple bond. The sp^2 hybridisation gives rise to materials as graphite or amorphous carbon.

In the context of fusion research, where carbon is one of the candidate materials for the ITER divertor plates [8], we are interested in the behaviour of carbon materials under hydrogen bombardment. This behaviour depends on the material's structure, for example, the hydrogen percentage and the sp^2/sp^3 ratio.

Recently nano crystalline diamond was exposed to deuterium plasma in the MAST tokamak [39]. The results showed that diamond films are apparently well suited to endure the conditions in the reactor vessel. Previously, experiments were conducted on the etching of graphite and diamond by thermal hydrogen atoms [43] for a surface temperature range of 300 to 1200 K. They showed that the carbon erosion yield of diamond is in the order of 10^{-6} C atoms per H atom. This is 2 to 4 (depending on the temperature with a maximum around 800 K) orders of magnitude lower than for graphite. Similar experiments with a-C:H containing $\approx 30\%$ hydrogen [44] resulted in yields of 10^{-4} to 10^{-2} C atoms per H atom. Experiments with H ions of energies ≥ 300 eV impacting on graphite with temperatures from 500 to 1000 K resulted in carbon erosion yields of 10^{-2} to 10^{-1} C atoms per H atom [45].

Experiments where diamond at room temperature was exposed to hydrogen plasma of energies of 10 to 500 eV showed that a defective structure emerged very similar to that of a-C:H. Exposure of diamond samples at higher temperatures gave rise to annealing of the defects creating a graphitic structure. Continuing plasma exposure removed the graphitic layers [46, 47].

In this study we compare a diamond sample which has 100% sp^3 bonds and 0% hydrogen to an a-C:H sample with 38% hydrogen and an sp^2/sp^3 ratio of about 0.25. We determined the retained hydrogen fraction in the samples and the carbon erosion yield as functions of the hydrogen energy and sample temperature.

5.2 Modelling

The MD code we used for our simulations is described in section 2.1.3.

Both, the diamond and the a-C:H sample, are bombarded with hydrogen atoms ranging in energy from 1 to 20 eV. The angle of incidence is 0 with respect to the surface normal. The simulated temperatures of the sample are 300, 700, 1000 and 1400 K. The initial samples are shown in Fig. 5.1. For both samples the boundaries are periodic

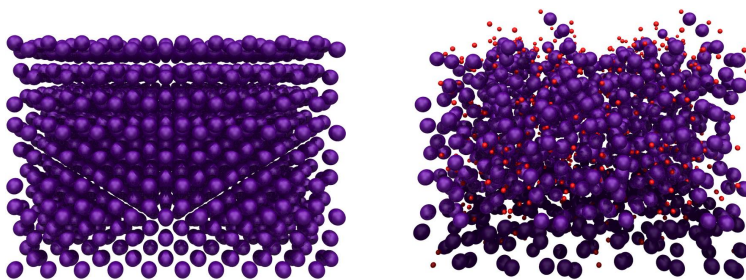


Fig. 5.1: The initial samples for the MD simulations. To the left the diamond sample is shown, to the right the a-C:H sample.

in two dimensions to simulate an infinite surface. The atoms in the bottom 3 Å have their velocity fixed to zero to avoid motion of the sample. The samples are cumulatively bombarded with H atoms, one every 127 fs which corresponds to a hydrogen flux of about $10^{30} \text{ m}^{-2}\text{s}^{-1}$. The projectile is placed above the surface outside the interaction range of the potential. The initial position is varied randomly over the surface area. Before the bombardment the sample is heated to the desired temperature until thermal equilibrium is reached. During the simulation the “bathtub” configuration of the thermostat as described in section 2.1.5 and Fig. 2.3 is applied. Two simulations were run for two different rise times 100 and 200 fs totalling to four runs per combination of temperature and projectile energy. Thermostated regions are not bombarded. The samples are bombarded with 3000 H atoms. At that point a steady state is reached, meaning that the erosion yield as function of the number of shot H atoms reaches a plateau and does not change with time anymore. Further bombardment leads to a decreasing erosion yield since the number of atoms in the sample is depleted.

The diamond sample has a size of $25.3 \times 26.3 \times 18.6 \text{ \AA}^3$. This corresponds to 2160 C-atoms in 18 layers of 120 atoms each. A total of 1368 atoms is neither fixed nor temperature controlled. The surface has the {111} orientation. The density is $\rho \approx 3500 \text{ kg m}^{-3}$ which agrees well with experimentally measured values.

The a-C:H sample has a size of $27.8 \times 28.4 \times 13.7 \text{ \AA}^3$. It contains 1860 atoms of which 1152 are C atoms. The atomic hydrogen content is $\approx 38\%$. A total of 1075 atoms (445 H and 630 C) is neither fixed nor temperature controlled. The sample was created from a sample used in earlier simulations [48]. It was cut in half in z-direction and then the remaining atoms were copied in x- and y-direction, thereby increasing the surface area by a factor of four. The resulting configuration was annealed and subsequently left to rest without temperature control to ensure that it is stable and relaxed before the simulation starts. The density of the sample is $\rho \approx 1800 \text{ kg m}^{-3}$. These values are consistent with measured densities and H fractions of a-C:H [49].

5.3 Results

The values presented in the following are determined by averaging over the four simulation runs for each combination of temperature and energy values. For the highest projectile energy the Berendsen thermostat with the rise time of 200 fs had difficulties maintaining the desired temperature. Consequently, it took longer before the desired temperature was reached again and in a few instances the subsequent H projectile arrived before this temperature was reached. This resulted in a wider spread of the calculated values and consequently in larger error bars.

5.3.1 Retained Hydrogen Fraction

In Fig. 5.2 the retained fraction of hydrogen atoms on a diamond {111} and a-C:H surface are plotted. Retained fraction in this context means the number of hydrogen atoms that is either sticking to the surface top-layer or lodged in the sample under the surface top-layer divided by the total number of hydrogen atoms shot at the sample. The number of retained hydrogen atoms is determined by counting the number of H atoms that is on or below the sample surface after the 3000 H atoms have been shot.

The solid lines show the results for diamond. The retained hydrogen fraction increases with increasing projectile energy. The retention occurs in two ways. For H atoms with energies that cannot penetrate the surface layer, the hydrogen binds to a dangling bond at the surface. H atoms with enough energy to penetrate the surface top layer (about 7 eV, see chapter 4) get lodged under the surface and may react chemically with a C atom. The penetration depth that can be reached by the H projectiles depends on their energy. Diffusion does not play a role here. The typical diffusion length l_D in three

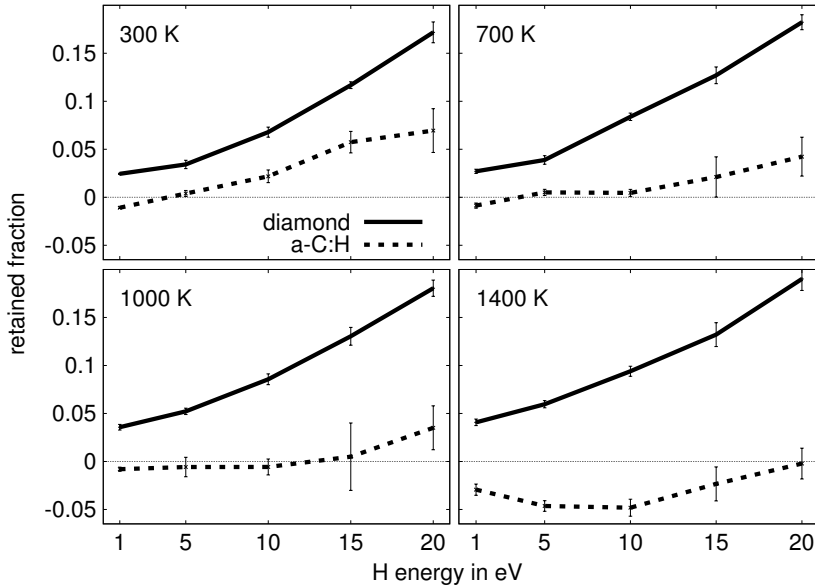


Fig. 5.2: The fraction of hydrogen retained in diamond compared to a-C:H after having shot 3000 H atoms at the sample. Negative values mean that the sample loses H atoms.

dimensions is given by:

$$l_D = \sqrt{6Dt} \quad (5.1)$$

where D is the diffusion coefficient and t the time. The total simulated time t is less than 0.5 ns. The diffusion coefficient of hydrogen in diamond is in the order of $D = 2 \cdot 10^{-14} \text{ cm}^2 \text{ s}^{-1}$. This yields for the typical diffusion length $l_D \approx 0.1 \text{ \AA}$. Once this layer of the surface is saturated with hydrogen almost all of the subsequently shot H atoms are reflected or replace a previously abstracted hydrogen atom. Hydrogen abstraction from the surface can occur through the Eley-Rideal process [50], surface recombination or the hot atom process and the vacated sites can be filled by other hydrogen projectiles. The retained fraction in diamond is not depending on the temperature in the simulated range. The amplitude of thermal oscillations in diamond apparently does not increase in such a way that the penetration of hydrogen into the crystal or out-gassing is facilitated, the crystal structure is too rigid. This is supported by the small coefficient of linear thermal expansion for diamond of 10^{-6} K^{-1} which is half of the value for graphite.

The dashed lines in the plots show the retained hydrogen fraction for the a-C:H sample. Here the increase of the retained fraction with increasing projectile energy is counteracted by the effect of the temperature: The hotter the sample the more hydrogen is

lost to the gas phase. The higher the temperature the larger the range of H energies where more hydrogen is out-gassed than shot at the sample resulting in a negative retained fraction. One sees in the plots of Fig. 5.2 that with increasing temperature the projectile energies increase where the number of retained H atoms surmounts the number of out-gassed H atoms (the point where the retained fraction becomes positive again). Thermal oscillations open temporary gaps and the higher the temperature the larger the gaps. This facilitates motion of hydrogen in both directions, into and out of the sample. The a-C:H structure is not rigid as diamond and more pliable such that it reacts stronger to temperature changes. Additionally, hydrogen abstraction takes place through the aforementioned effects of the Eley-Rideal process [50], surface recombination or hot atom process to a larger degree than for diamond because more hydrogen is present in the simulated sample. For H atoms with 20 eV energy the H atoms are lodged so deeply under the surface that the temperature of 1400 K is not sufficient to drive out more hydrogen than is shot at the sample.

Overall for all temperatures the sticking probability on diamond is larger than on a-C:H. In the a-C:H a certain degree of saturation has been reached which shows in the negative retained hydrogen fraction. Furthermore, there is a connection to the carbon erosion yield treated in the following section: The erosion yield is larger for the a-C:H sample than for diamond which implies that more hydrocarbons and with them more hydrogen leaves the sample.

5.3.2 Carbon Erosion Yield

Fig. 5.3 shows the carbon erosion yield for the simulated samples. The erosion yield is determined by dividing the total number of carbon atoms that is not bound to the sample anymore by the number of H atoms shot at the sample. The results for diamond are shown with a solid line and for the a-C:H with a dashed line. At the temperatures of 300 and 700 K some of the yield values at 1 eV hydrogen energy are zero and therefore do not show in the logarithmic plot. The carbon erosion yield is larger for the a-C:H than for the diamond sample for all temperatures. This is because the a-C:H has more sp^2 hybridised carbon and the CC double bonds readily reduce to a single bond in the presence of hydrogen [51]. Furthermore, in the a-C:H the carbon is already partly hydrogenated, so it takes less bonds to break before a C atom is freed from the sample.

In experiments with thermal hydrogen impacting on a-C:H and diamond [43, 44] the carbon erosion yield from a-C:H was 2 to 4 orders higher than the yield for diamond which was 10^{-6} C atoms per H atom.

Our lowest simulated H energy is 1 eV which is more energetic than thermal hydrogen. One may therefore expect that the erosion yield is higher than in the experiments with thermal hydrogen. For diamond our simulations result in a yield of 10^{-4} C atoms per

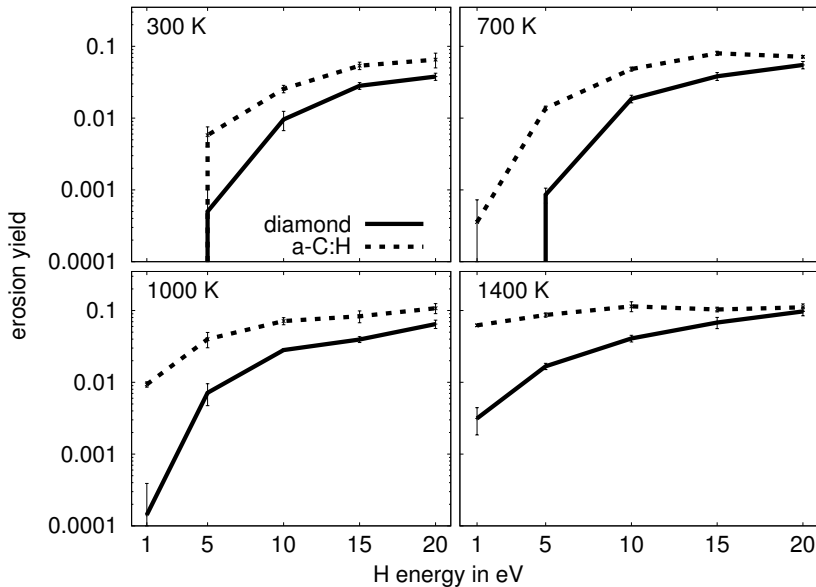


Fig. 5.3: The carbon erosion yield of diamond compared to a-C:H after having shot 3000 H atoms at the sample.

H atom which is a factor of 100 higher than in the experiments. For a-C:H the yield is 10^{-2} C atoms per H atom which is at the lower end of the range measured experimentally.

Experiments with hydrogen of energies ≥ 100 eV impacting on graphite show carbon erosion yields of 10^{-2} to 10^{-1} C atoms per H atom [45] which is in the same order of magnitude as we find in our simulations for H energies ≥ 10 eV.

Generally the erosion yields obtained from our MD simulations are about one order of magnitude higher than the values determined in experiments. This is because the simulations do not include processes that may lower the experimentally measured erosion yields significantly. One example is the redeposition of erosion products. More details are described in chapters 6 and 7.

The diamond sample exhibits steadily increasing erosion yields with increasing temperatures for all projectile energies. The higher the temperature the more kinetic energy the C atoms have which contributes to bond breaking.

The picture is different for a-C:H. Here the erosion yield also increases with higher temperatures but the yield also saturates at a maximum which moves towards lower projectile energies for higher temperatures. This may be caused by the accumulation of hydrogen on the a-C:H surface. This has a shielding effect, repelling incoming hydrogen

projectiles such that they cannot react with sample C atoms and contribute to erosion. Salonen et al. [52] observed this effect in MD simulations when they non-cumulatively bombarded samples with different hydrogen percentages and obtained a lower carbon erosion yield for higher hydrogen contents.

We saw in the previous section on the retained hydrogen fraction in a-C:H that for higher temperatures this fraction becomes lower. With a little imagination the curves for retained fraction and erosion yield appear mirrored at a line parallel to the x-axis. In other words, they behave inversely proportional: the more hydrogen is retained the lower the erosion yield (for a given H energy).

Interestingly, this is not true for diamond where the retained hydrogen fraction is virtually the same for all temperatures. So, the nature of the dependency of the erosion yield for a-C:H must be caused by its structure and the hydrogen contents.

Fig. 5.4 shows the erosion yield as a function of the sample temperature. For diamond the yield steadily increases with increasing temperature and H projectile energy. For a-C:H the yield increases as well but above 1000 K this trend seems to stop and the temperature dependency flattens. In experiments one observes a temperature with an erosion yield maximum [43, 44]. In our simulations there is no such maximum, most

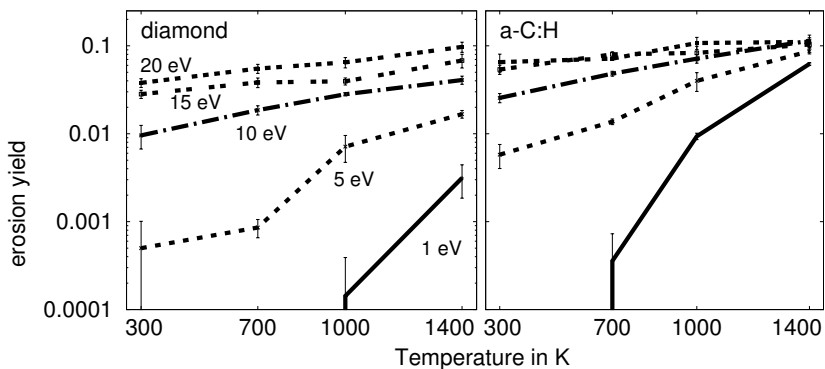


Fig. 5.4: The carbon erosion yield of diamond (left) and a-C:H (right) as function of the temperature.

likely because the time scale of the MD simulations is too short to observe thermally activated reactions. These reactions are described in the model of Küppers et al. [53, 54] which was amended by Mech et al. [51]. According to this model the reduction of the yield above a temperature of about 600 K is caused by the thermal annealing which returns the structure to a sp^2 hybridisation by releasing hydrogen.

5.3.3 Eroded Hydrocarbon Species

Figs. 5.5 through 5.10 show the particle yield per shot hydrogen for H atoms, H molecules and different hydrocarbon species. There is one figure per H energy and in each figure the yields for diamond and a-C:H at the four temperatures are compared.

Hydrogen Atoms and Molecules

The number of reflected H atoms is very large for all sample temperatures and hydrogen energies. This number decreases with increasing H energy. This is in line with the understanding that projectiles with higher energies get lodged deeper in the sample and are less likely to get reflected.

At 1 eV hydrogen energy there is no temperature dependency of the number of reflected H atoms or released H molecules for the diamond sample. The surface of the diamond is fully hydrogenated and the majority of the H projectiles is simply reflected independent of the sample temperature. This is shown in Fig. 5.5.

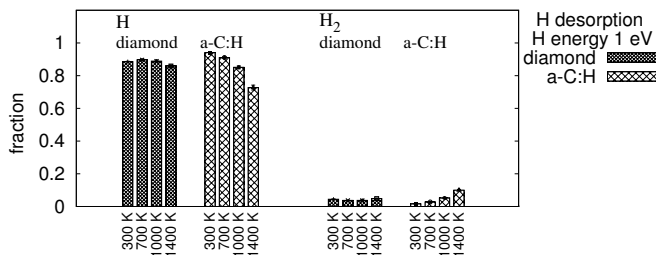


Fig. 5.5: The fraction of hydrogen desorbed from diamond and a-C:H samples with different temperatures and under bombardment with H atoms of 1 eV energy.

In contrast to this, the number of H atoms reflected from the a-C:H sample drops from more than 0.9 at 300 K to about 0.75 at 1400 K. This drop is almost entirely explained by the increasing H₂ formation for increasing temperature. At 300 K the fraction is about 0.02, at 1400 K it is 0.1. Instead of leaving the sample as H atom they leave in pairs as H₂.

Processes as Langmuir-Hinshelwood, Eley-Rideal and hot-atom reactions play a role here [55]. The Langmuir-Hinshelwood process describes the recombination of two H atoms that are bound to the surface and are thermalised. When they meet they form a chemical bond and fly off as hydrogen molecule. This process is enabled by higher temperatures encouraging diffusion of H atoms over the surface and thus making the meeting of two hydrogen more likely. Furthermore, a higher temperature eases

the breaking of the existing bond between the hydrogen and the surface atom. So, it is to be expected that the Langmuir-Hinshelwood process becomes more frequent with increasing temperature. This is what we see in Fig. 5.5.

The Eley-Rideal process describes the instant reaction of an incoming H atom with an H atom bound to the surface to form an H_2 . The cross section of this reaction is in general fairly small and becomes even smaller with increasing sample temperature [50, 56].

These two processes are the extremes of a continuous spectrum of possible processes. The in-between process is called hot-atom reaction where an incoming H projectile dissipates some of its energy but before thermalising and becoming a part of the sample it forms a bond with an H atom which is bound to the surface and the resulting H_2 is released from the sample.

The information about the frequency of the three processes cannot be extracted from the existing simulation data. To obtain this information reruns are required where more intermediate data are stored.

At 5 eV hydrogen energy the behaviour of the a-C:H sample is similar to the sample under 1 eV bombardment. The only difference is that less H atoms and more H_2 molecules are released which was already explained. The results are shown in Fig. 5.6.

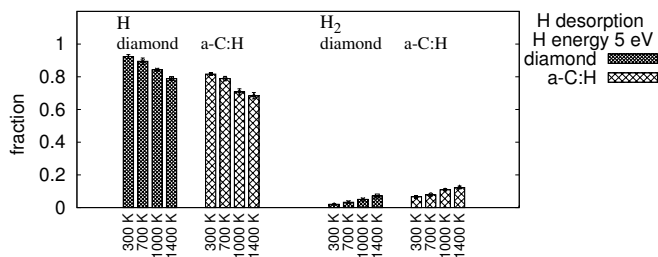


Fig. 5.6: The fraction of hydrogen desorbed from diamond and a-C:H samples with different temperatures and under bombardment with H atoms of 5 eV energy.

The diamond sample shows a decrease in the release of H atoms and an increase of the number of H_2 molecules. The dependency of the H_2 formation on the temperature may point to the fact that the hot-atom process plays an important role. The larger energy of the H projectile enables it to get through the shield formed by the fully hydrogenated surface and lose some of its energy in the process. This also increases its residence time and consequently the probability to form a H_2 with one of the bound

hydrogen. Here the dependency on the sample temperature which enhances diffusion plays a role again as explained earlier.

At 10 eV hydrogen energy the diamond sample behaves similar as under 5 eV bombardment with the only difference that more H_2 are formed. This is shown in Fig. 5.7. The H atoms of this energy can easily penetrate the hydrogen shield formed by the hydrogenated surface, hence even more H projectiles will get the chance to recombine with a surface H than under 5 eV bombardment.

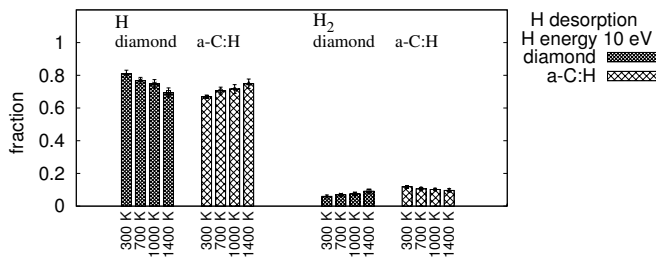


Fig. 5.7: The fraction of hydrogen desorbed from diamond and a-C:H samples with different temperatures and under bombardment with H atoms of 10 eV energy.

The a-C:H sample shows different behaviour than at lower H energies by reflecting an increasing number of hydrogen atoms for increasing sample temperature. At this energy the H projectiles reach implantation depths well below the surface top layer. The likelihood of recombination with a surface H atom is very small. What we see here is the temperature dependent out-gassing of hydrogen.

At 15 and 20 eV hydrogen energy the trends described for 10 eV bombardment still show, however, the effect is weaker because the H projectile now reaches depths in the diamond and a-C:H samples that almost guarantee that this particular H atom gets trapped. Out-gassing plays a role and the H_2 molecules are most likely formed in the sample and subsequently released. This is visualised in Fig. 5.8.

Carbon Atoms, Carbon Molecules and Hydrocarbons

Figs. 5.9 and 5.10 show the particle yield for CH_y and C_2H_y with $y=0-4$. The general trend is that, within error bars, the number of eroded species increases with the H projectile energy and the sample temperature. Furthermore, the erosion of the a-C:H sample is larger than of the diamond sample. This trend is true for every individual hydrocarbon. Hydrocarbons with more than two hydrogen rarely form. Mostly they are

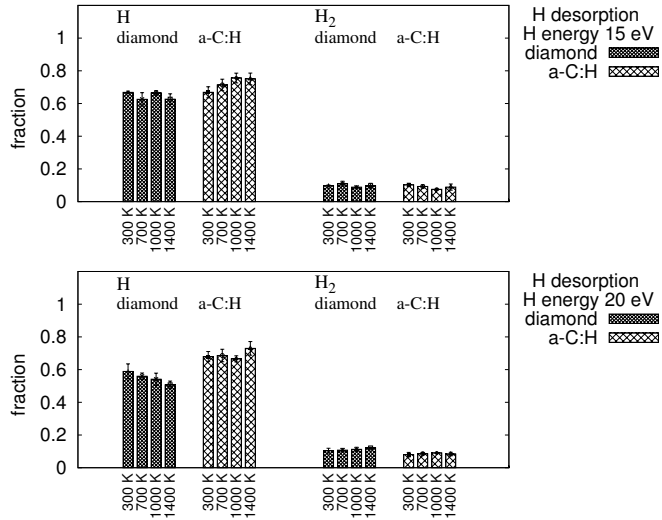


Fig. 5.8: The fraction of hydrogen desorbed from diamond and a-C:H samples with different temperatures and under bombardment with H atoms of 15 and 20 eV energy.

the result of bombarding the a-C:H sample with 1 or 5 eV. Possibly the lower energies favour hydrogenation because the projectile does not penetrate the material and interacts with the C atoms at the top layer.

The most eroded species are C, CH, C₂, C₂H and C₂H₂.

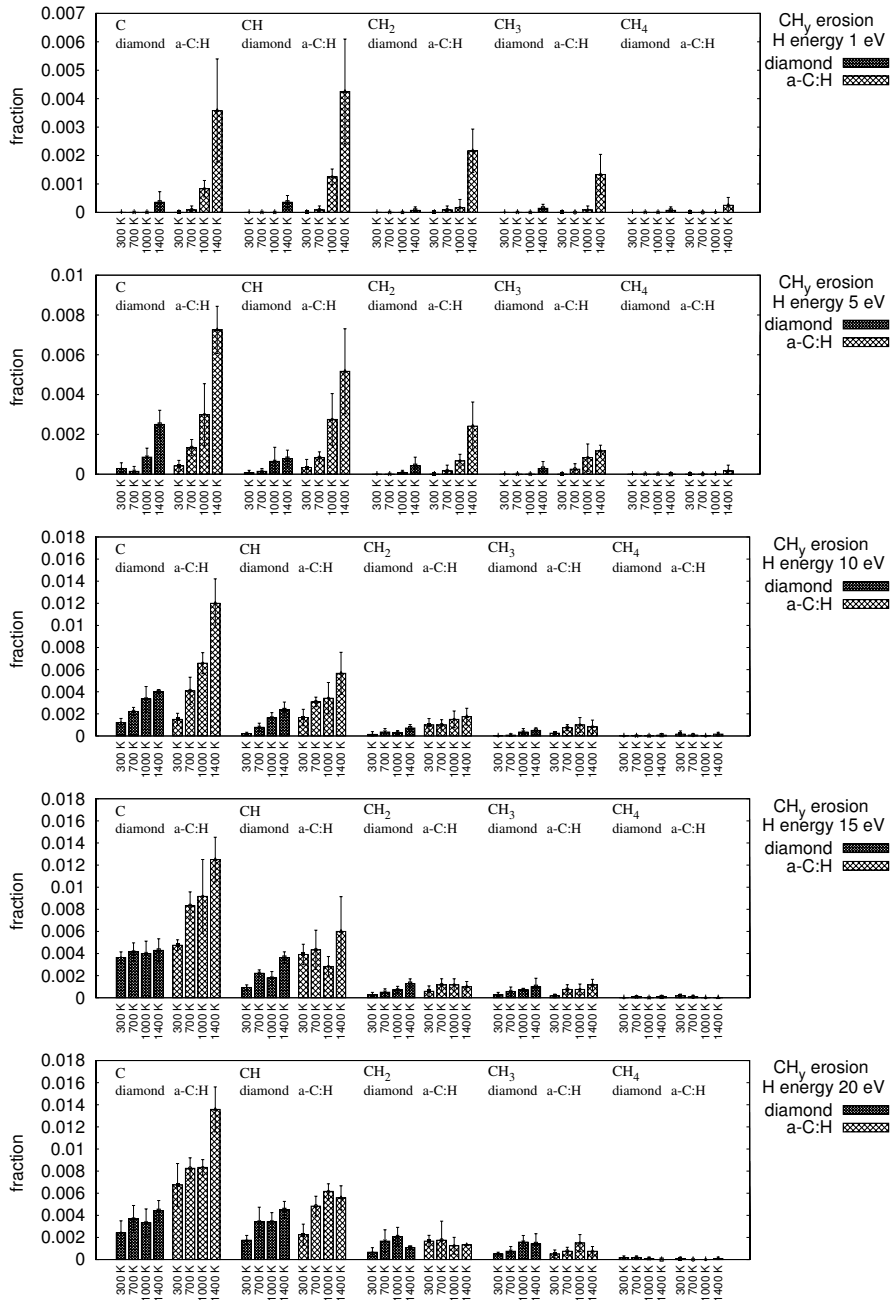


Fig. 5.9: The yields of eroded CH_y hydrocarbon species from diamond and a-C:H samples with different a-C:H temperatures and under bombardment with H atoms of different energies.

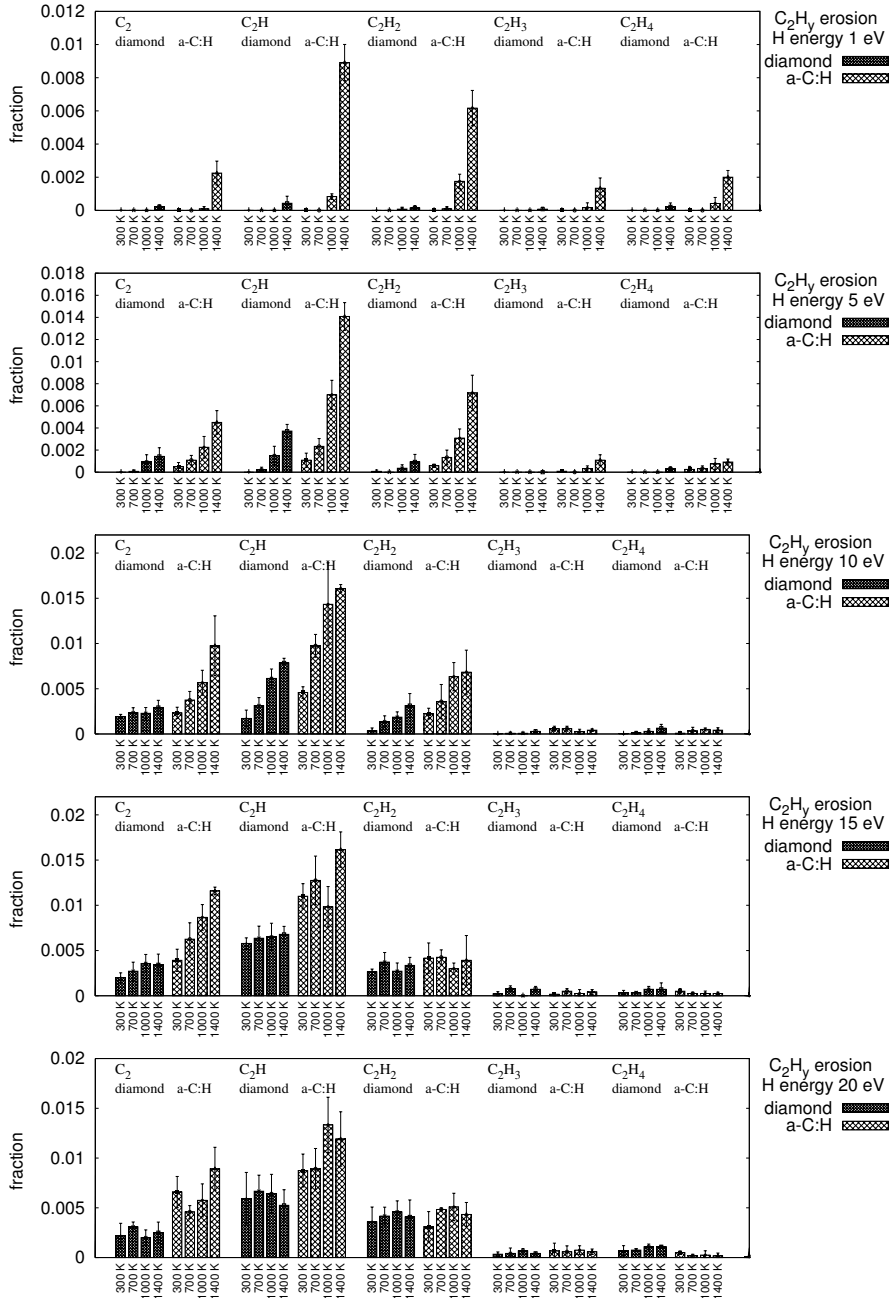


Fig. 5.10: The yields of eroded C_2H_y hydrocarbon species from diamond and a-C:H samples with different temperatures and under bombardment with H atoms of different energies.

5.4 Conclusion

The retained hydrogen fractions and carbon erosion yields of a-C:H and diamond under hydrogen bombardment were simulated with MD. The hydrogen energies ranged from 1 to 20 eV, the sample temperatures were 300, 700, 1000 and 1400 K.

The retained hydrogen fraction is larger on the diamond sample than on the a-C:H sample. The a-C:H sample is already (partly) saturated and the diamond sample has dangling bonds at the surface where hydrogen can easily stick.

Temperature has little effect on the hydrogen retention in diamond. The a-C:H sample loses an increasing amount of hydrogen with increasing temperature which is in line with experimental findings. This loss is caused by the thermal motion of the sample atoms which enables the diffusion of hydrogen out of the sample. Other effects include surface abstraction of hydrogen through the Langmuir-Hinshelwood and hot-atom processes.

The carbon erosion yield is larger for a-C:H than for diamond. This can be mainly attributed to the higher amount of sp^2 hybridised carbon atoms in the a-C:H and that many carbon atoms are already partly hydrogenated so less chemical bonds need to be broken to get the C atom out of the sample.

Each of the eroded hydrocarbon species shows the same temperature and H projectile energy dependency as the overall trend of the carbon erosion yield. The eroded hydrocarbon species are mainly C, CH, C_2 , C_2H and C_2H_2 .

However, one has to bear in mind that the time scale of the MD simulations is limited. Experiments have shown that the diamond structure under hydrogen bombardment of H energies ≥ 10 eV changes to a a-C:H like structure at room temperature and to a graphitic structure at higher temperatures. These graphitic layers are removed under subsequent exposure and possibly increase the carbon erosion yield to the same level as that of graphite or a-C:H.

Chapter 6

Amorphous Hydrogenated Carbon under extremely high Hydrogen Fluxes *

6.1 Introduction

Experiences with tokamak and ion beam experiments as well as theoretical studies have shown that carbon surfaces are significantly eroded by hydrogen. This presents a challenge for the design of large tokamaks, where some of the plasma facing surfaces may consist of carbon based material. In particular, the next generation experimental fusion reactor ITER [3] which is meant to demonstrate fusion as possible commercial energy supply. According to experiments and theoretical studies such a carbon surface may be eroded away on a short time scale, possibly too short to demonstrate the feasibility of fusion [38].

Roth et al. [13] compiled an overview of a number of ion beam and tokamak experiments where the erosion yield of carbon material under hydrogen bombardment was measured. Since the hydrogen energies and surface temperatures of the bombarded materials differ among experiments only experimental data taken at or near the maximum erosion yield temperature are included and the measured erosion yield values are scaled to a hydrogen energy of 30 eV. The normalisation factors are published in Roth et al. [57]. The data show that in the flux range of $10^{19} \text{ m}^{-2}\text{s}^{-1}$ to $10^{24} \text{ m}^{-2}\text{s}^{-1}$ the yield Y drops with increasing flux Φ as $Y \propto \Phi^{-0.54}$. Fig. 6.1 shows this dependency.

Salonen et al. [40] conducted molecular dynamics (MD) simulations of an amorphous hydrogenated carbon (a-C:H) sample at temperatures between 300 and 1100 K. The sample was non-cumulatively bombarded with H atoms of 10 eV. The results show that the erosion yield is temperature dependent with values between 0.002 and 0.02 C atoms per incident H atom and a maximum at 900 K. At 300 and 900 K the main eroded species was C_2H_2 . Furthermore, they observed that a non-cumulative bombardment of a surface supersaturated with hydrogen resulted in an erosion yield ten times smaller than the yield from their original sample. They concluded that the high

* Published in: Physical Chemistry Chemical Physics (PCCP), volume 11, page 9823, Authors: E. D. de Rooij, U. von Toussaint, A. W. Kley and W. J. Goedheer

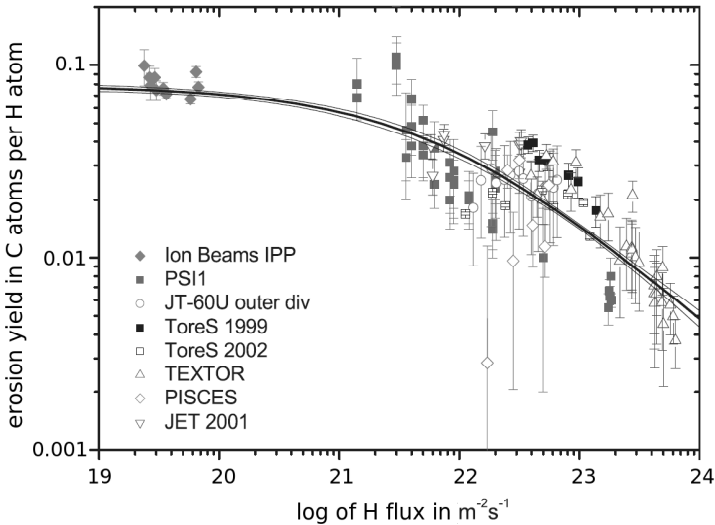


Fig. 6.1: The carbon erosion yield versus the hydrogen flux as compiled by Roth et al. [13].

hydrogen concentration in the upper surface layer reduces the erosion yield and may be the reason for the experimentally observed reduction of the erosion yield.

They also simulated cumulative bombardment of an a-C:H sample with 10 eV H atoms at 300 K and a flux of $1.5 \cdot 10^{29} \text{ m}^{-2} \text{ s}^{-1}$ which resulted in an erosion yield of 0.04. Here the main eroded species were CH_x ($x=1,2,3,4$) and C_2H_x ($x=3,4,5,6$). Later simulations by Träskelin et al. [58] of cumulative bombardment of an a-C:H sample with 10 eV H atoms resulted in a yield of 0.036 at 300 K and a flux of $4.4 \cdot 10^{28} \text{ m}^{-2} \text{ s}^{-1}$.

The flux dependency of the erosion yield has not been studied yet with MD. In this paper we present MD simulations of a-C:H samples that are bombarded with H atoms of 10 eV energy and normal incidence.

The energy of 10 eV is within the range that is expected at the divertor surface of ITER. Furthermore, in linear ion beam experiments the energy of the ions impinging on the target is around 10 eV and almost mono-energetic since the potential drop at the sheath is the determining factor for the ion energy.

In most linear ion beam experiments the magnetic field is parallel to the target surface normal. The ions are accelerated over the sheath at the target and the velocity component parallel to the surface normal is much larger than the velocity components associated with the gyration of the particle caused by the magnetic field. Hence, the angle of incidence is close to the surface normal. In the case of physical sputtering

bombardment with an angle other than 0 from the surface normal is expected to result in larger yields [32]. Since 10 eV lies below the physical sputtering threshold for a-C:H this effect is expected to be negligible.

The bombardment is done for sample temperatures of 700 and 1000 K and for different hydrogen flux values from $10^{28} \text{ m}^{-2}\text{s}^{-1}$ to $10^{30} \text{ m}^{-2}\text{s}^{-1}$. MD simulations of cumulative bombardment at lower fluxes are very time consuming. However, we make the additional assumption that our sample represents the equilibrium state [59] under a flux of $10^{18} \text{ m}^{-2}\text{s}^{-1}$. Hence, the erosion yield at this much lower and experimentally achievable flux can be determined by simulating non-cumulative bombardment.

The aim of this study is to explore the extent to which a hydrogen buildup in the upper surface layer can contribute to the observed erosion yield reduction. The absence of a flux dependency in the MD simulations suggests that the yield drop is not caused by erosion reduction through enrichment of the upper surface layers with hydrogen. Instead the reason lies in external factors as, for example, redeposition or vapour shielding through erosion products, thus changing flux or energy distribution of the impinging particles. These two phenomena cannot completely be simulated with MD.

Furthermore, the species that are eroded and the H:C ratio in the eroded material are determined as function of the flux and the sample temperature. The results are compared to the results of Roth et al. [13], Salonen et al. [40] and Träskelin et al. [58].

6.2 Modelling

6.2.1 MD code

The MD code we used for our simulations is described in section 2.1.3.

Salonen et al. [40] and Träskelin et al. [58] used the same code for their simulations.

6.2.2 Simulated sample

The simulated sample consists of an a-C:H sample of the size $27.8 \times 28.4 \times 13.7 \text{ \AA}^3$. It contains 1860 atoms of which 1152 are C atoms. The atomic hydrogen content is $\approx 38\%$. It was created by cutting an existing sample [48] in half in z-direction and then copying the remaining atoms in x- and y-direction, thereby increasing the surface area by a factor of four. The resulting configuration was annealed and subsequently left to rest without temperature control to ensure that it is stable and relaxed before the simulation starts. Fig. 6.2 shows the initial sample at both temperatures.

The density of the sample is $\rho \approx 1800 \text{ kg m}^{-3}$. These values are consistent with measured densities and H fractions of a-C:H [49].

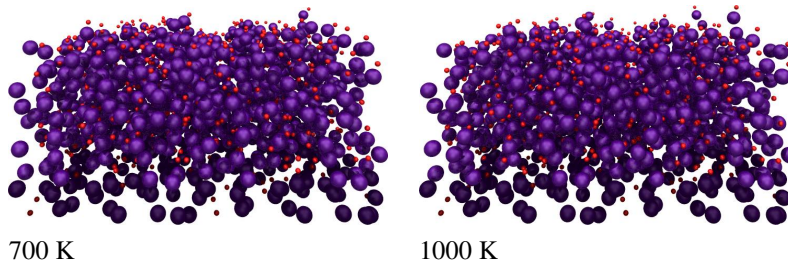


Fig. 6.2: The initial a-C:H samples. Blue spheres symbolise carbon atoms, red spheres hydrogen atoms. The left column shows the sample at 700 K and the right one at 1000 K.

The boundary conditions are periodic in two dimensions to simulate an infinite surface. The 108 H atoms and 264 C atoms in the bottom 3 Å have their velocity fixed to zero. This avoids motion of the sample and simulates an immobile bulk. The entire initial sample is heated to the desired temperature until thermal equilibrium is reached. The simulated temperatures are 700 and 1000 K. The sample is then bombarded with H atoms of 10 eV energy and of normal incidence.

During the bombardment the Berendsen thermostat is only applied to atoms located in the edge regions of 2 Å width and in a layer of 2 Å thickness above the fixed atoms. This is illustrated as the “bathtub” configuration in Fig. 2.3 on page 18. The bombarded region is limited to the atoms which are not temperature controlled, thereby avoiding immediate quenching of the impact energy. A total of 1075 atoms (445 H and 630 C) is neither fixed nor temperature controlled.

The simulations are run for different flux values: $10^{18} \text{ m}^{-2}\text{s}^{-1}$, $10^{28} \text{ m}^{-2}\text{s}^{-1}$, $10^{29} \text{ m}^{-2}\text{s}^{-1}$ and $10^{30} \text{ m}^{-2}\text{s}^{-1}$. For the fluxes of $10^{28} \text{ m}^{-2}\text{s}^{-1}$ and higher the sample is bombarded cumulatively, one H atom at a time and the output sample of the n -th bombardment is input to the $(n+1)$ -th. The flux Φ is determined by the time Δt between the H impacts: $\Phi = 1/(\Delta t A)$ with A as the bombarded surface area. In real time the computation of one H shot takes approximately 20 minutes on the computing cluster in Garching (see page 113) for a flux of $10^{28} \text{ m}^{-2}\text{s}^{-1}$. For $10^{29} \text{ m}^{-2}\text{s}^{-1}$ and $10^{30} \text{ m}^{-2}\text{s}^{-1}$ the time is roughly 10 and 100 times shorter, respectively.

3500 H atoms are shot at the sample, meaning that every surface atom has on average been hit 15 times (unless it is eroded away). After 3000 H impacts the carbon erosion yield levels out indicating that a steady state is reached. When bombarding longer the yield is dropping because most of the non-fixed and non-temperature controlled atoms are eroded away. Fixed atoms cannot be eroded and temperature controlled atoms quench the impact energy quickly and are less likely to leave the sample. So, further bombardment erodes less and less C atoms.

The MD simulation of cumulative bombardment at a flux of $10^{18} \text{ m}^{-2}\text{s}^{-1}$ is clearly outside the current computer capabilities. Therefore we take advantage of the fact that the initially prepared sample resembles very closely the experimentally observed steady state system under low-fluence bombarding conditions [48, 59]. Consequently, we do not have to wait the whole time span required after an H impact for this flux. We know how the sample will look like at the end of this time, namely as the initial sample and can do the simulation with non-cumulative bombardment. The waiting time is 1.27 ps (same as for a flux of $10^{29} \text{ m}^{-2}\text{s}^{-1}$). This time is five or ten times longer than the thermostat rise time (see below) and long enough for the sample to return to thermal equilibrium. In our simulations, if C atoms have been eroded this has happened within the first 0.7 ps after an H impact. So we can assume that we did not miss any eroded carbon.

The simulation runs are done twice for each of two thermostat rise times: 0.1 and 0.2 ps. Thus every set of flux and temperature values is run four times. We found that the rise time has no influence on the yield and from these four values the mean and the standard deviation for the carbon erosion yield are determined.

6.2.3 Heat transport

No real material is capable of withstanding the heat loads we subject our simulated sample to. These are 16 GW/m^2 at $10^{28} \text{ m}^{-2}\text{s}^{-1}$ to 1.6 TW/m^2 at $10^{30} \text{ m}^{-2}\text{s}^{-1}$. The material would immediately be overheated because of local defects or insufficient coupling to a heat sink. Our sample, on the other hand, is so small that all the excess heat can be conducted to the temperature controlled border regions and removed by the Berendsen thermostat before the impact of the subsequent H atom. Thus the simulation results show the response of the material to very high fluxes at a given temperature.

To show that our sample has the properties of real material we calculate the thermal conductivity k and thermal diffusivity α of the simulated sample following the procedure outlined in section 2.1.9 on page 24. Both values should be below experimentally determined values. First we need to determine the specific heat c_P of the simulated sample in two different ways, firstly, by using the definition of c_P as the heat energy required to increase the temperature of 1 kg material by 1 K and secondly, by calculating c_P from enthalpy fluctuations,

The quotient of ΔE over ΔT in Eqn. 2.15 is found by bombarding a thermalised sample with 10 eV H atoms impacting every 0.1 ps while the thermostat is switched off. For 50 shots, corresponding to a time $\Delta t = 5 \text{ ps}$, the total energy input into the system is $E_{\text{tot}} = 500 \text{ eV} = 8 \cdot 10^{-17} \text{ J}$. During the same time the reflected H atoms carry away an energy of $E_{\text{ref}} = 10^{-17} \text{ J}$ and the energy deposited into the sam-

ple is $\Delta E = 7 \cdot 10^{-17}$ J resulting in $\Delta E/\Delta t = 1.4 \cdot 10^{-5}$ J/s. As consequence of this energy input the temperature of the simulated sample changes with time as $\Delta T/\Delta t = 3.3 \cdot 10^{14}$ K s⁻¹ at 1000 K. The mass is given by the non-fixed atoms of the sample and $m = 1.86 \cdot 10^{-23}$ kg. With (2.15) this yields for the specific heat $c_P \approx 2280$ J K⁻¹ kg⁻¹ at 1000 K.

The mean of the enthalpy and the mean square enthalpy were determined from a simulation of a sample in thermal equilibrium at 1000 K. With Eqn. 2.16 this results in a specific heat of $c_P \approx 1975$ J K⁻¹ kg⁻¹ at 1000 K.

The experimental c_P value of graphite is $c_P \approx 1940$ J K⁻¹ kg⁻¹ at 1000 K [60]. A larger c_P -value for our sample is to be expected since a higher hydrogen content increases the heat capacity [61, 62].

We now calculate the values of k and α as they are required for our simulations. For c_P the lower value of 1975 J K⁻¹ kg⁻¹ is used which results in a larger value for the required heat diffusivity. For the flux the largest value of 10^{30} m⁻² s⁻¹ is used. The length l is taken as half the distance between the temperature controlled borders of the sample $l = 12$ Å, which is a typical length available for the impact heat to be conducted to the temperature controlled region. The temperature difference ΔT is the difference between the temperature at the impact site and the sample temperature. At the impact site the temperature is taken as the hydrogen energy expressed as temperature, where we assume that the entire kinetic energy of the projectile is transferred to the sample and propagated as atomic oscillations which we interpret as temperature. Therefore ΔT is 10 eV $\hat{=}$ $1.1 \cdot 10^5$ K. The thermal conductivity k and thermal diffusivity α that are required by the simulation to transport the heat of the highest flux are $k = 0.017$ W K⁻¹ m⁻¹ and $\alpha = 5 \cdot 10^{-9}$ m² s⁻¹. These values are well below the measured values of $k = 0.2 - 0.3$ W K⁻¹ m⁻¹ and $\alpha = 2 \cdot 10^{-7}$ m² s⁻¹ for polymeric and graphitic films [61]. Hence, the simulated material shows properties that are similar or no better than the ones of real material.

6.2.4 Hydrogen pressure

During our simulations the sample is subjected to a very high hydrogen pressure. This pressure P can be expressed as

$$P = \frac{F}{A} = \frac{m_H v_H}{\Delta t A} \quad (6.1)$$

where F is the force exerted by the hydrogen on the surface A , m_H and v_H are mass and velocity of the H atom and Δt is the time between the H impacts. This yields a pressure of 1 MPa at 10^{28} m⁻² s⁻¹ to 100 MPa at 10^{30} m⁻² s⁻¹.

To determine whether these pressures significantly influence the material properties in the simulations, we calculate the mean decrease in inter-atomic distances resulting from the highest pressure.

The compressibility β of solids is defined as the quotient of the fractional volume change $-dV/V$ and the applied change in pressure dP :

$$\beta = -\frac{1}{V} \frac{dV}{dP}. \quad (6.2)$$

Typical values are in the order of $10^{-11} \text{ m}^2/\text{N}$ [63].

The mean change in inter-atomic distance can now be calculated as follows: with $P = 10^8 \text{ Pa}$ which is the hydrogen pressure on the material at a flux of $10^{30} \text{ m}^{-2} \text{ s}^{-1}$ one finds that the change in volume is $-dV/V < 10^{-2}$, thus the volume under pressure differs by less than 1 % from its original value. The inter-atomic distances are the third root of the compressed volume and hence $0.99^{1/3} = 0.9967$ of their original value. Hence, the atoms are displaced by less than 0.35 % of the nominal bond length corresponding to approximately 0.005 \AA in a C-C bond which is about ten times smaller than the mean thermal displacement at the simulated temperatures.

Therefore we can conclude that the hydrogen pressure exerted on the surface by the impinging hydrogen does not change the material properties.

6.3 Results & discussion

6.3.1 Flux dependency of the yield

Fig. 6.3 shows the erosion yield as function of the hydrogen flux. In panel (a) our simulation results for 10 eV hydrogen energy are plotted. In panel (b) all shown data are scaled up to 30 eV, that is, multiplied with factor 1.4 [57]. This includes our results and the results of Salonen et al. [40] and Träskelin et al. [58]. Additionally, the fit to experimental data as proposed by Roth et al. [13] is shown with extrapolation towards lower and higher flux values.

The original plot by Roth et al. [13] with the experimental data used for the fit is shown in Fig. 6.1.

The erosion yield is determined from the simulation data by counting the number of C atoms eroded from the sample divided by the number of H atoms that were shot at it. The displayed values from our simulations are the mean values with their standard deviation calculated from the four runs done for each parameter combination. The erosion yield values at a flux of $10^{18} \text{ m}^{-2} \text{ s}^{-1}$ result from non-cumulative bombardment. The yields for $\Phi \geq 10^{28} \text{ m}^{-2} \text{ s}^{-1}$ stem from cumulative bombardment.

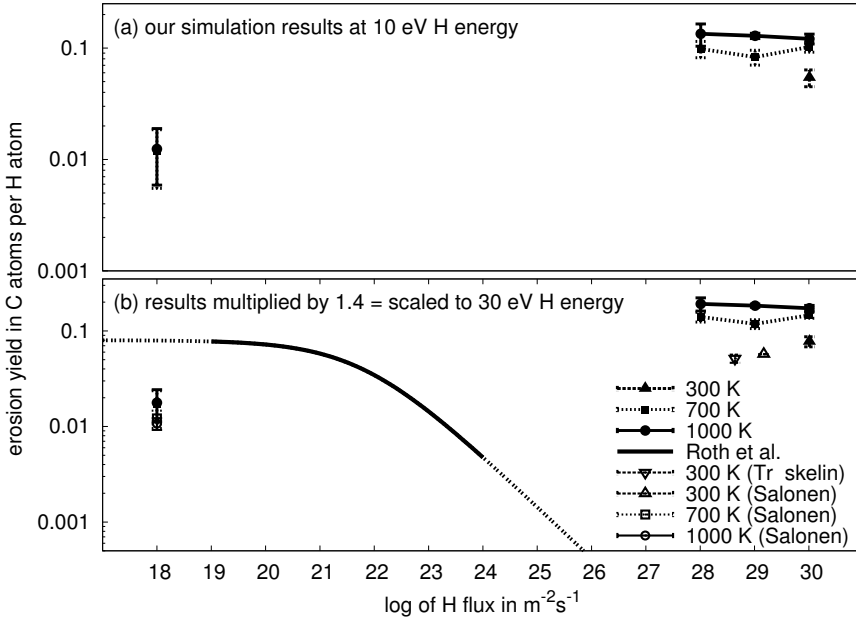


Fig. 6.3: Panel (a) shows the carbon erosion yield as function of the hydrogen flux from our simulations for temperatures of 300, 700 and 1000 K and an H energy of 10 eV. Panel (b) shows our results multiplied with 1.4 to scale the erosion yields to 30 eV H energy [57]. For comparison, the extrapolated fit to experimental data from Roth et al.[13] and the results of the MD simulations by Salonen et al.[40] and Träskelin et al.[58] at 300 K are shown along with our simulations at that temperature. The values for the flux of $10^{18} \text{m}^{-2}\text{s}^{-1}$ are obtained with non-cumulative bombardment.

The results from our cumulative bombardment show a temperature dependency, with the yield at 1000 K being larger than at 700 K. This is in line with previously published models of the erosion mechanism stating that with increasing atomic hydrogen flux the temperature of maximum erosion T_{max} shifts towards higher temperatures [54, 64].

However, our results do not show a drop in the erosion yield for increasing fluxes as the extrapolation of the experimental data to higher fluxes does. At the fluxes of $10^{28} \text{m}^{-2}\text{s}^{-1}$ and higher the erosion yields of our simulations lie many orders of magnitude higher than the fitting function and there is hardly any dependency on the flux.

This huge discrepancy suggests that the reason for the drop of the erosion yield which shows in experiments is not included in our simulations. One possible cause could be the redeposition of eroded C_xH_y . For a higher hydrogen flux more hydrocarbons are redeposited and do not appear in the gas phase. Alternatively, the surface could be shielded by a cloud of atomic and molecular hydrogen and hydrocarbons. This cloud

could work as a buffer where the incoming H atoms are decelerated such, that they cause less erosion at the surface.

Our erosion yields for the cumulative bombardment at 700 and 1000 K are about a factor of 2.5 or 3 higher than found by Salonen et al. [40] and Träskelin et al.[58] at 300 K. There are two causes for this difference: the sample temperature and the sample structure. To estimate the temperature effect, we have done four cumulative simulation runs for 300 K at the highest flux of $10^{30} \text{ m}^{-2}\text{s}^{-1}$. Comparing the results of our cumulative simulation runs at 300, 700 and 1000 K at the highest flux we found that the yield at 300 K is a factor of 2 to 2.5 smaller than at 700 and 1000 K. Compared to the simulations of Salonen et al. [40] and Träskelin et al. [58] at 300 K our average yield at 300 K is a factor of 1.35 to 1.5 larger. This can be explained by the fact that the yields are very dependent on the exact structure and composition of the sample. In particular density, hydrogen percentage and sp^2/sp^3 ratio play a role. Lower densities allow a H projectile to penetrate deeper into the sample such that it does not erode carbon from the top layer. A higher hydrogen percentage means that the sample material is softer and may be easier to erode. In the presence of hydrogen the double bonds of sp^2 hybridised C atoms readily form a single CC bond and a CH bond. This hydrogenation is a first step towards erosion [51]. Our sample contains with 38 % more hydrogen and is therefore softer than the sample used by Salonen et al. [40] with 29 %, so it is to be expected that our yields are consistently higher.

Analogously, the different sample structure is the reason for the lower yields obtained by Salonen et al. [40] with non-cumulative bombardment.

The yields resulting from our non-cumulative bombardment are almost equal for the two temperatures. This agrees with the temperature dependency found by Salonen et al. [40] with non-cumulative bombardments: The yields for 700 and 1000 K are within error bars the same.

Furthermore, the yields found from non-cumulative bombardment are about one order of magnitude lower than the yields for the cumulative bombardments at the high fluxes. The difference in yields results from the different simulation methods. To verify this we took a sample where after 3000 H atom impacts under a flux of $10^{29} \text{ m}^{-2}\text{s}^{-1}$ the erosion yield started to level off, indicating that a steady state was reached, and bombarded it non-cumulatively. The resulting yield was 0.02 which is a factor 5 lower than for the cumulative bombardment. Similarly, Salonen et al. [40] found that their yield from cumulative bombardment was a factor of 20 larger than from non-cumulative bombardment.

This can be understood by considering the following: Under the non-cumulative bombardment the sample is not going through continuous erosion. Any defects in the surface left by an eroded C atom are not seen by the subsequent H projectile. Under

the cumulative bombardment the surface becomes defective with loosely bound hydrocarbons and thus more prone to erosion. Additionally, the continuous bombardment locally induces high temperatures resulting in stretching and weakening of bonds. This increases the probability that subsequent H projectiles break such a bond.

Multiplying our yield at flux $10^{18} \text{ m}^{-2}\text{s}^{-1}$ with a factor of 5 gives the yield for the cumulative bombardment according to our simulations. This puts the value right on the experimental curve.

6.3.2 Hydrogen buildup in the cumulatively bombarded sample

Fig. 6.4 shows the H:C ratio of the samples as function of the flux for both temperatures 700 and 1000 K. The hydrogen enrichment has values between 0.72 (41.8%) and 0.78 (43.8%) for 1000 K and between 0.84 (45.6%) and 0.86 (46.2%) for 700 K. The initial sample has a H:C ratio of 0.61, corresponding to 38.1% hydrogen. The hydrogen contents for 1000 K is lower than for 700 K which is to be expected since hotter material can hold less hydrogen. For higher fluxes there is a slight tendency towards a higher hydrogen percentage, however this trend is very small.

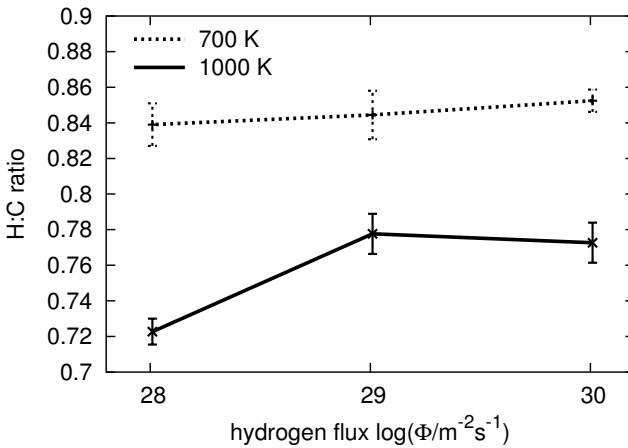


Fig. 6.4: The plot shows the ratio of the number of H atoms to the number of C atoms as function of the hydrogen flux for both temperatures 700 and 1000 K. The H:C ratio is larger for 700 K because samples of higher temperatures can hold less hydrogen.

Fig. 6.5 shows the H:C ratios for the initial sample and the steady state samples as function of the height of the sample for 700 K and for 1000 K.

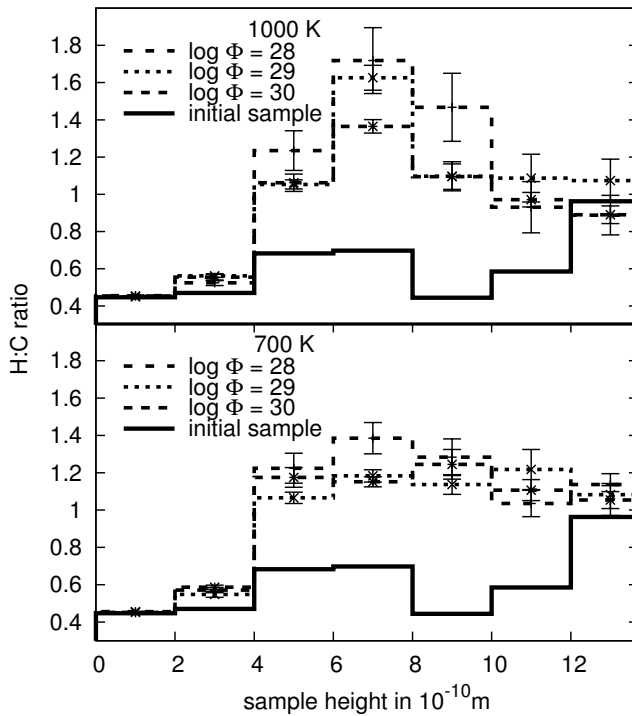


Fig. 6.5: The plot shows the ratio of the number of H atoms to the number of C atoms as function of the sample height at 1000 K in the top panel and at 700 K in the bottom panel. $x=0$ corresponds to the sample bottom. The values for steady state under the different hydrogen fluxes of 10^{28} , 10^{29} and $10^{30}\text{m}^{-2}\text{s}^{-1}$ are displayed and for the initial sample. One sees that the buildup of hydrogen in the sample under bombardment is only weakly depending on the flux.

One sees that there are no large differences in the hydrogen buildup under the different fluxes. All samples show a buildup of hydrogen in the layers above 4 Å with a maximum at around 7 Å which is more pronounced in the 1000 K sample. This formation of a hydrogen enriched layer has also been observed in several other simulations under a broad range of parameters (for example, for hydrogen energies of 10 eV [52] down to 0.5 eV [65]). At the top layer (above 12 Å) the hydrogen percentage drops as carbon is eroded away and with it binding sites for hydrogen disappear. This indicates that the hydrogen atoms in the enriched top layers are chemically bound to carbon atoms. A look at the total potential energy of the sample supports this assumption. Additionally, experiments where a barium surface was exposed to hydrogen ion bombardment show that the hydrogen enrichment of the surface reduces the physical sputtering yield [66].

The hydrogen buildup at the lowest flux is higher at larger depths than for the higher fluxes. This is caused by diffusion which starts to become visible at simulation times in the order of ns. Shooting 3500 H atoms with a flux of $10^{28} \text{m}^{-2} \text{s}^{-1}$ at the sample corresponds to a simulated time of 44.45 ns which is ample time for diffusion to show effects on that scale. For a higher temperature faster diffusion is to be expected which shows nicely in the higher H:C ratio of the sample at 1000 K.

Salonen et al. [52] non-cumulatively bombarded samples with different hydrogen percentages, and observed a lower carbon erosion yield for higher hydrogen contents. They proposed that this effect, which they termed hydrogen shielding, may explain the reduction of the erosion yield with increasing flux. Thereby they implicitly assumed that the hydrogen percentage of the steady state is flux dependent, such that a higher flux causes a higher hydrogen percentage. However, the variations of the hydrogen concentration buildup in our simulations over the flux range of two orders of magnitude are relatively small. This, together with the achieved steady state erosion profile, indicates that the effect of hydrogen shielding [52] alone is not sufficient to explain the experimentally observed carbon erosion yield reduction at fluxes above $10^{21} \text{m}^{-2} \text{s}^{-1}$, see Fig. 6.3.

6.3.3 Eroded species

Fig. 6.6, 6.7 and 6.8 show the reflection and desorption of hydrogen and the composition of the eroded hydrocarbons as function of the flux.

Fig. 6.6 shows the reflection and desorption of H atoms and H_2 for bombardment with 10 eV H atoms. The x-axis is broken between $10^{18} \text{m}^{-2} \text{s}^{-1}$ and $10^{28} \text{m}^{-2} \text{s}^{-1}$. For both temperatures there is a minimum in H_2 -formation at $10^{29} \text{m}^{-2} \text{s}^{-1}$. For $10^{30} \text{m}^{-2} \text{s}^{-1}$ the H_2 -formation is highest. H reflection shows the opposite behaviour. Under non-cumulative bombardment H reflection is lower and H_2 formation is higher than under cumulative bombardment. In the cumulative case the surface becomes saturated with hydrogen and reflection of incoming H projectiles becomes more likely. When H atoms are reflected they do not form bonds with surface H atoms and less H_2 is formed. The H_2 formation probably involves the Eley-Rideal, Langmuir-Hinshelwood and hot atom mechanisms for abstraction [50]. The cross sections for each of the processes cannot be extracted from our current simulation data.

Fig. 6.7 shows the yields of hydrocarbon species with one C atom for both temperatures. Under the cumulative bombardment the amount of eroded atomic C decreases with increasing flux. The CH yield shows an increase for 1000 K, at 700 K there is a dip at the flux of $10^{29} \text{m}^{-2} \text{s}^{-1}$. Both, CH_2 and CH_3 yields drop with increasing flux. At 700 K they also show a dip at $10^{29} \text{m}^{-2} \text{s}^{-1}$. Under non-cumulative bombardment and at 1000 K C, CH, CH_2 and CH_3 have almost the same yield; at 700 K CH has the

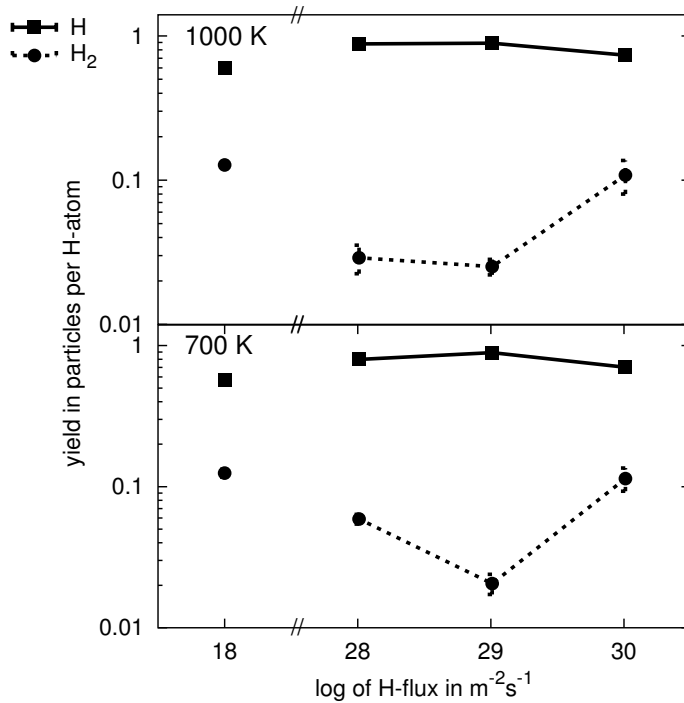


Fig. 6.6: The reflection and desorption of H and H₂ as function of the hydrogen flux for 700 and 1000 K. Note the broken x-axis. At the flux of $10^{18}\text{m}^{-2}\text{s}^{-1}$ the value for the non-cumulative bombardment is plotted.

highest yield closely followed by CH₂, CH₃ and C.

Fig. 6.8 shows the yields of hydrocarbon species with C₂. They behave very similar to the CH_y species. The yield of C₂ drops with increasing flux, the yields of C₂H and C₂H₂ increase and the yield of C₂ with more than 2 H atoms drops. Under non-cumulative bombardment C₂H and C₂H₂ show the highest yield. The values for C_xH_y for x larger than 2 are not shown because the contributions are below 10^{-4} .

Under cumulative bombardment most carbon is eroded in the form of C₂, C₂H and C and under non-cumulative bombardment as C₂H and C₂H₂ which agrees with Salonen et al. [40].

When calculating the total H:C ratio in the eroded hydrocarbons (H and H₂ are not included) one finds that there is no significant flux dependency. The H:C ratio is around 0.6 to 0.7, with lower values for the higher temperature. The non-cumulative bombardment shows a higher H:C ratio of 1.05 for 700 K and 1.1 for 1000 K.

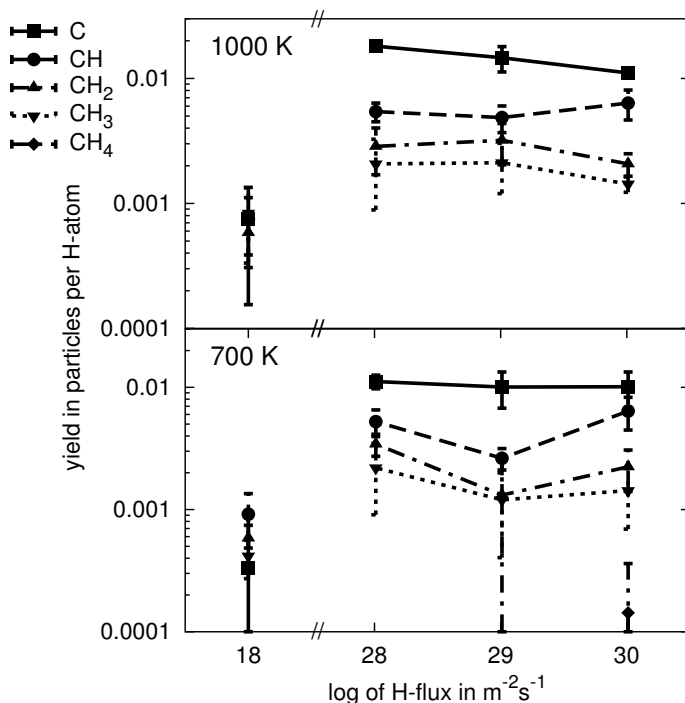


Fig. 6.7: The erosion yield of the different CH_y species as function of the hydrogen flux. The top panel shows the yield for a sample temperature of 1000 K the bottom panel for 700 K. Note the broken x-axis. At the flux of $10^{18} \text{m}^{-2} \text{s}^{-1}$ the value for the non-cumulative bombardment is plotted.

6.4 Conclusions

We have conducted molecular dynamics simulations of an a-C:H sample to determine the flux dependency of carbon erosion yields and eroded species in the high-flux regime at temperatures of 700 and 1000 K. The sample was cumulatively bombarded with 10 eV H atoms at different fluxes in the range of $10^{28} \text{m}^{-2} \text{s}^{-1}$ to $10^{30} \text{m}^{-2} \text{s}^{-1}$. Additionally, the sample was non-cumulatively bombarded.

The simulation results show no significant flux dependency of the erosion yield. This is in contrast to experimental findings where the yield drops steeply with increasing flux values above $10^{21} \text{m}^{-2} \text{s}^{-1}$. This suggests that the reason for the yield drop is not included in the MD simulations. For example, redeposition or a shielding cloud of hydrogen and hydrocarbons.

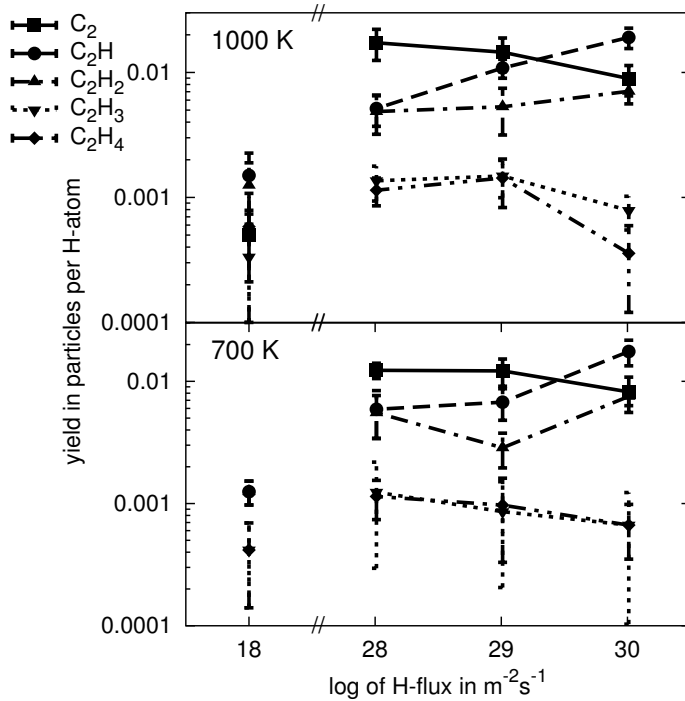


Fig. 6.8: The erosion yield of the different C_2H_y species as function of the hydrogen flux. The top panel shows the yield for a sample temperature of 1000 K the bottom panel for 700 K. Note the broken x-axis. At the flux of $10^{18}m^{-2}s^{-1}$ the value for the non-cumulative bombardment is plotted.

The main eroded species under cumulative bombardment are C_2 , C_2H and C and the H:C ratio of all eroded material is 0.6 - 0.7. For increasing fluxes there is a tendency towards more CH , C_2H and C_2H_2 but a drop in more hydrogenated hydrocarbons, C atoms and C_2 . The total H:C ratio hardly changes. This ratio is larger for a sample of 1000 K than of 700 K. Under non-cumulative bombardment the main eroded species are C_2H_2 and C_2H with a H:C ratio of all eroded material of 1.05 - 1.1.

Non-cumulative bombardment results in yields that are a factor of 5 to 20 lower than the yields under cumulative bombardment. The differences are caused by the discontinuity of the non-cumulative bombardment neglecting the effects of the previous impact as, for example, defect formation or hydrogen abstraction.

Summarising, neither in the carbon erosion yield nor in the eroded species nor in the hydrogen buildup in the sample a strong flux dependency has been found in our simulation results. Therefore the MD results suggest that the experimentally measured flux

dependency is likely to be caused by external factors such as, for example, redeposition or vapour shielding, and not by properties inherent to the material. In that case a similar flux dependent decrease of the erosion yield may also be present for materials other than carbon, alleviating problems due to wall erosion in high-flux fusion experiments (like ITER and its successor DEMO). However, to the authors knowledge no comprehensive study of the flux dependency of the erosion yield of presently discussed plasma-facing wall materials (like tungsten or beryllium) similar to the one for carbon [13] does exist.

When attempting to simulate redeposition and vapour shielding effects one may have to use methods other than MD. The system size needs to be increased significantly and the influence of magnetic fields considered. Existing codes for simulating the plasma particle flow near surfaces under influence of a magnetic field need input regarding the erosion from the wall. They need to take care to use the 'naked' erosion and not experimental data which already include the very effects that are going to be simulated.

Chapter 7

Redeposition of Hydrocarbons on Amorphous Hydrogenated Carbon

7.1 Introduction

In chapter 6 the flux dependency of the carbon erosion yield was studied. The MD simulations results did not show a flux dependency, suggesting that the cause for the experimentally measured reduction of the erosion yield for higher fluxes lies outside the realm of the simulations. One of the possible effects that may cause the measured flux dependency is redeposition. To obtain more insight we study the sticking probability of hydrocarbons on a-C:H surfaces that have been subjected to different hydrogen fluxes.

In previously conducted MD simulations by Sharma et al. [67] the reflection coefficients of small hydrocarbons on an a-C:H surface decreased with the projectile energy increasing from thermal to 10 eV. All studied hydrocarbons with 10 eV energy had a reflection coefficient below 0.05 with higher values for the hydrocarbons with more H atoms. The reflection probability increases with the hybridisation from sp to sp² to sp³. The not reflected molecules either stick or break up. Alman and Ruzic [68] studied the reflection coefficients of hydrocarbons of thermal to 100 eV energy on a “soft” a-C:H surface and a “hard” graphite surface that had been bombarded with hydrogen. The surface temperature was 300 K. They found that the sticking probability increases with the number of unpaired electrons and when the hybridisation changes from sp³ to sp² to sp. Furthermore, the sticking probability on the “soft” surface was higher.

The sticking of CH₃ on unsaturated carbon atom sites was studied by Träskelin et al. [69] for energies from thermal up to 10 eV. For thermal CH₃ they found very low sticking probabilities which are observed in experiments with thermal CH₃ as well [70]. CH₃ with 10 eV energy on the other hand had a much higher sticking probability. In other simulations Träskelin et al. [71] investigated the sticking of thermal C₂H_x (x = 0 – 6) on a diamond surface of 0 K. The energies of the hydrocarbons were 0.03 and 0.2 eV. Their results showed that the sticking probability decreases with increasing number of H atoms in the molecule. Furthermore, they found that the more energetic molecules with x ≤ 2 had a higher sticking probability than the ones with 0.03 eV.

Redeposition occurs when the eroded hydrocarbon is ionised in the plasma and subsequently forced back to the surface along the magnetic field lines. This may or may not be close to where it originally was eroded. The question is now, how well these hydrocarbons stick on the surfaces. To answer this we determined the sticking coefficient for various hydrocarbons on samples that were subjected to different hydrogen fluxes in the previous simulations. A sticking coefficient that is higher on the sample subjected to the higher flux may help reduce the erosion yield. This is a simple approach not taking into account the effect of pumps etc.

To investigate this the steady state samples from the simulations in chapter 6 were bombarded non-cumulatively with hydrocarbons. For comparison, the initial surface is bombarded with hydrocarbons as well.

7.2 Modelling

The MD code we used for our simulations is described in section 2.1.3.

The steady state samples described in chapter 6 and the initial sample are non-cumulatively bombarded with carbon atoms, C_2 molecules and the following hydrocarbons: CH, CH_2 , CH_3 , C_2H and C_2H_2 . Fig. 6.2 in chapter 6 shows the initial sample and Fig. 7.1 the samples after the bombardment with different hydrogen fluxes.

One sees that the lower the flux the sample was subjected to, the more porous the surface appears. Note that all the samples still have about the same number of carbon atoms, roughly 600 at 700 K and 500 at 1000 K. As shown in chapter 6 the carbon erosion yield is the same under all fluxes and the samples in Fig. 7.1 have been bombarded with the same number of hydrogen atoms. Please disregard the loose hydrogen and hydrocarbons hovering over the samples.

The samples are bombarded with carbon atoms and hydrocarbons of an energy of 10 eV. The angle of incidence is 0 degrees from the surface normal and the molecules are shot with different orientations as shown in Fig. 7.4 to 7.10. The temperature of the surfaces is 700 or 1000 K.

7.3 Results

7.3.1 Sample Properties

First we took a look at the simulated samples. Since previous studies show a relation between hybridisation and sticking probability [67, 68] we determined the sp^2 and sp^3 fraction of the samples. The result is shown in Fig. 7.2.

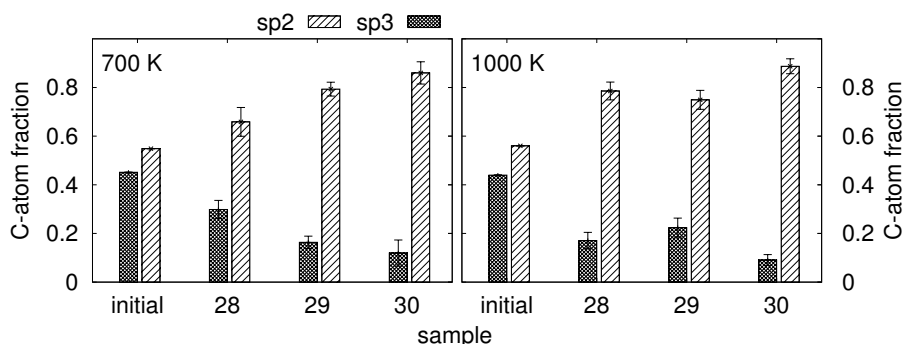


Fig. 7.2: The fraction of sp^2 and sp^3 hybridised carbon in the samples.

One clearly sees a trend towards a higher sp^2 fraction in the samples for higher fluxes. This means that in samples that have been bombarded with higher fluxes more CC double bonds are present. This has an effect on the sticking probabilities of hydrocarbons.

The sp^3 fraction in the samples decreases with increasing sp^2 fraction. There is no sp^3 hybridised carbon in the sample.

7.3.2 Sticking Probability

In the presence of H atoms CC double bonds tend to break and form two energetically more favourable single bonds. This is an exothermic transition: A CC double bond has a bond energy of 6.4 eV whereas two CH bonds $2 \times 4.3 \text{ eV} = 8.6 \text{ eV}$. This mechanism facilitates the chemical erosion of carbon as described by Mech et al. [51]. Hydrocarbon molecules with reactive sites probably have a similar effect on a CC double bond. Two CC single bonds have a binding energy of $2 \times 3.6 \text{ eV} = 7.2 \text{ eV}$ which is more than that of a CC double bond. Thus, the reaction is exothermic. This implies that the probability for hydrocarbons to react with the carbon atoms of a surface with a high sp^2 fraction is higher than on a surface with lower sp^2 fraction. This results in a higher sticking probability on surfaces with higher sp^2 fraction. In the same direction point the results

of Sharma et al. [67] and Alman and Ruzic [68] who found that the sticking probability increased when the hybridisation of the projectile changed from sp^3 to sp^2 .

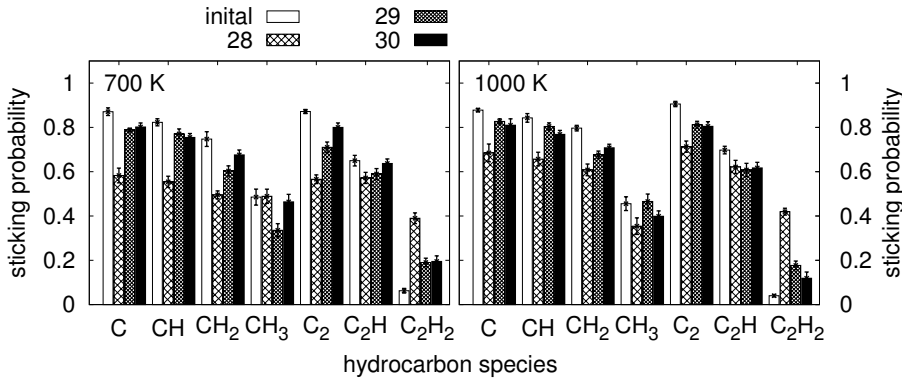


Fig. 7.3: The sticking probability for the selected hydrocarbons. They are shown for the various samples and both sample temperatures.

Fig. 7.3 shows the sticking probability for each of the simulated hydrocarbons on the different samples. The values represent the average over all simulation runs for the respective molecules and the limited number of orientations shown in Figs. 7.5 to 7.10. This means that the results do not represent an averaging over all possible molecule orientations and their probability.

In all figures from Fig. 7.3 onwards “28” means that the bombarded sample is the steady state sample from the simulations at the flux of 10^{28} hydrogen atoms per second per m^2 conducted for the study described in chapter 6, “29” means the sample is the steady state at the flux of $10^{29}m^{-2}s^{-1}$ and so on. “Initial” or “0” refers to the initial sample which was the input configuration for the simulations regarding the flux dependency in chapter 6. The initial sample has a atomic hydrogen percentage of $\approx 38\%$, the bombarded samples $\approx 43\%$ for 1000 K and $\approx 46\%$ for 700 K.

Overall Fig. 7.3 shows that the sticking probability decreases with increasing number of H atoms in the hydrocarbon which is in line with previous findings [67, 68, 71]. There is hardly any temperature dependence visible in Fig. 7.3. On the 1000 K sample the sticking probability is about 5% higher than on the 700 K sample.

For most simulated hydrocarbons there is a rising trend for the sticking with increasing hydrogen flux on the surfaces. The exceptions are CH_3 and C_2H with no visible trend and C_2H_2 , where the sticking probability drops with increasing flux. The sticking probability is highest on the initial sample, except for C_2H_2 .

In the following we take a closer look at the individual species:

C, CH, CH₂ exhibit higher sticking probabilities for higher fluxes, see Figs. 7.4, 7.5 and 7.6. This trend follows the increase of the sp² fraction in the sample, see Fig. 7.2.

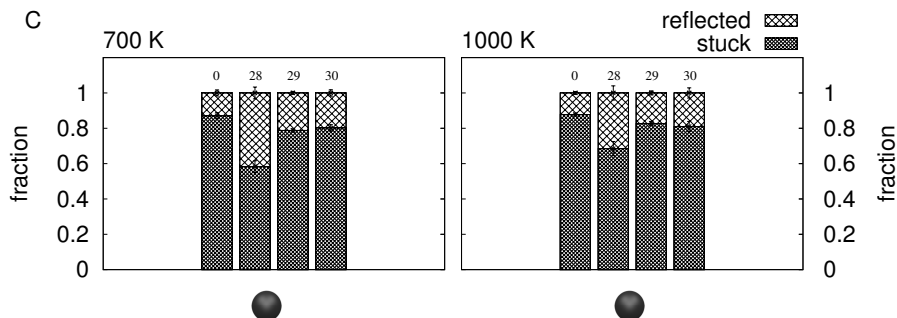


Fig. 7.4: The probabilities for sticking and reflection of the C atom on different surfaces and for both temperatures. “Stuck” means that all atoms of the molecule are stuck to the surface and “reflected” means that all atoms of the molecule have escaped from the surface.

However, the highest sticking probability occurs on the initial sample even though it has the lowest sp² fraction. The reason is probably the difference in hydrogen content which is lower in the initial sample than in the other samples. Salonen et al. [40] found in MD simulations that carbon material saturated with hydrogen exhibits a lower chemical erosion yield under hydrogen bombardment. This implies that the incoming hydrogen reacted less with the hydrogen saturated surface. Hence, it is conceivable that a high hydrogen content also works as a shield against the sticking of hydrocarbons.

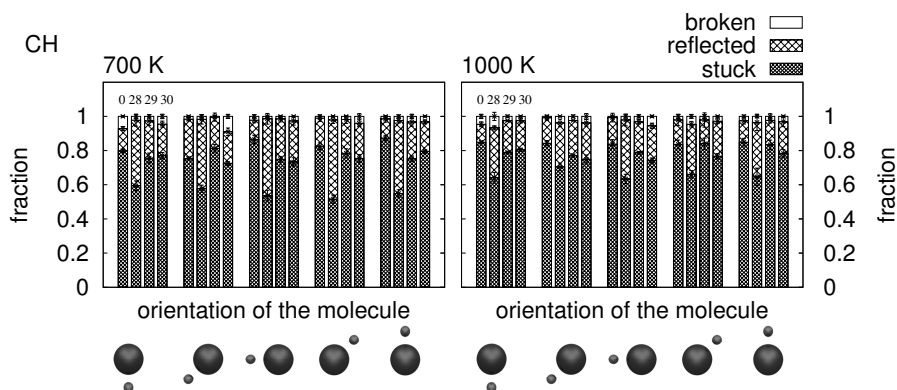


Fig. 7.5: As in Fig. 7.4 but for CH. “broken” means that the molecule broke on impact and at least one fragment stuck to the surface and one other fragment escaped.

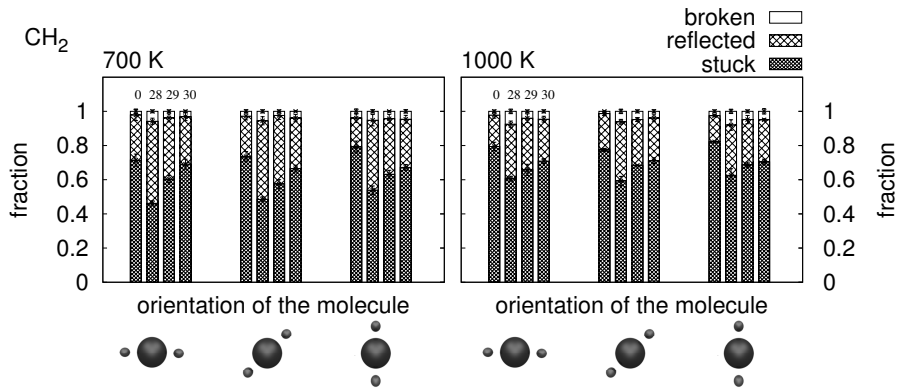


Fig. 7.6: As in Fig. 7.5 but for CH_2 .

The sticking probability for atomic C hardly differs from the one for CH. Most of the studied orientations of CH are such that a reactive site of the molecule points towards the surface. Hence, the result is not surprising. From CH to CH_2 there is a drop in the sticking probability which is explained by the additional H atom which reduces the number of reactive sites on the C atom. This effect was already observed in previous studies [67, 68]. The sticking probabilities of the CH and CH_2 molecules only weakly depend on their orientation. This suggests that they are both very reactive species.

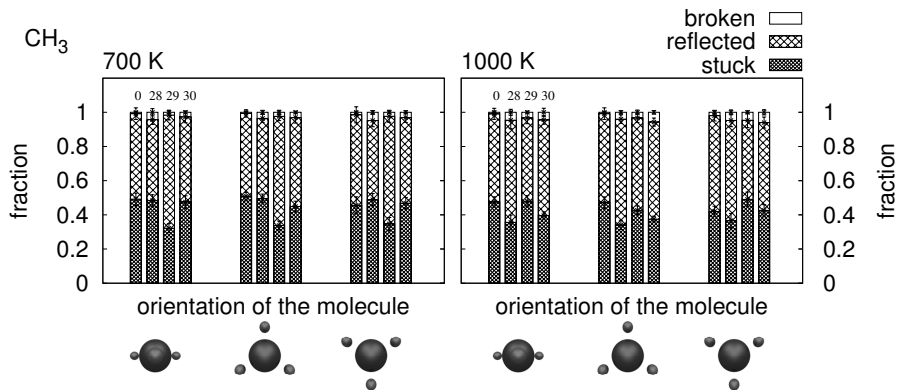


Fig. 7.7: As in Fig. 7.5 but for CH_3 .

The sticking probability of CH_3 is lower than that for CH_2 which is in line with the expectations. However, there is no clear trend towards higher sticking on the surfaces with the sp^2 fraction. Furthermore, the molecule does not show a higher sticking prob-

ability on the initial surface even though this surface has the lowest hydrogen content. This suggests that the molecule has a stable configuration and is not very reactive.

Fig. 7.7 shows that the sticking probability is independent from the molecule's orientation. This differs from thermal CH_3 where in MD simulations sticking only occurred when the one bonding site of the molecule points towards the surface and finds a dangling bond to stick. At higher CH_3 energy, as in our simulations, this effect loses its importance [69].

C_2 exhibits higher sticking probabilities for higher fluxes, see Fig. 7.8. Very similar to C, CH and CH_2 this trend follows the increase of the sp^2 fraction in the sample which is shown in Fig. 7.2. C_2 has a sticking probability comparable to atomic carbon, there are no hydrogen atoms that can prevent a binding reaction at the surface.

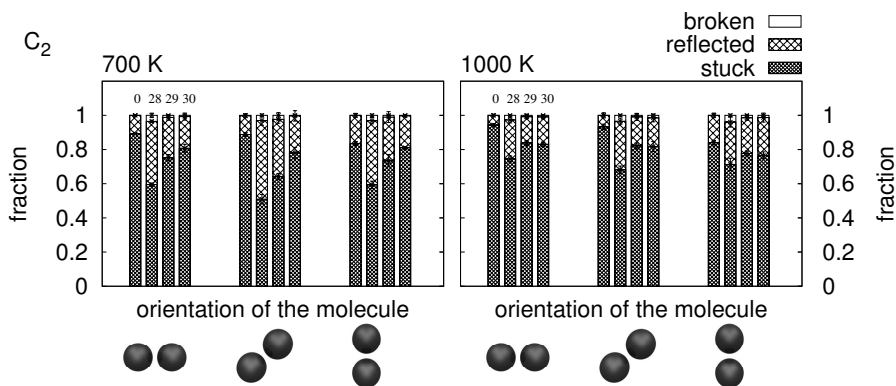


Fig. 7.8: As in Fig. 7.5 but for C_2 .

The sticking probability of C_2H is shown in Fig. 7.9 and is virtually constant on all bombarded samples. A higher sp^2 hybridisation has no effect on the sticking of this molecule.

The C_2H is a linear molecule which is reactive at the end of the C atom with the unpaired electron. For the molecule to stick the reactive end has to encounter a reactive site. Looking solely at the sp^2 fraction of the samples this implies that the sticking probability should increase with increasing sp^2 fraction.

However, the make-up of the sample plays an important role here. In Fig. 7.1 the bombarded samples are shown. It is apparent that the one under the lowest flux at the top of the figure is the most porous. One can easily imagine that small hydrocarbons (C, CH, CH_2 , CH_3) can slip in and out the pores without reacting with sample atoms. If the hydrocarbon is a little larger though, it is less likely to enter the pores, but once it has

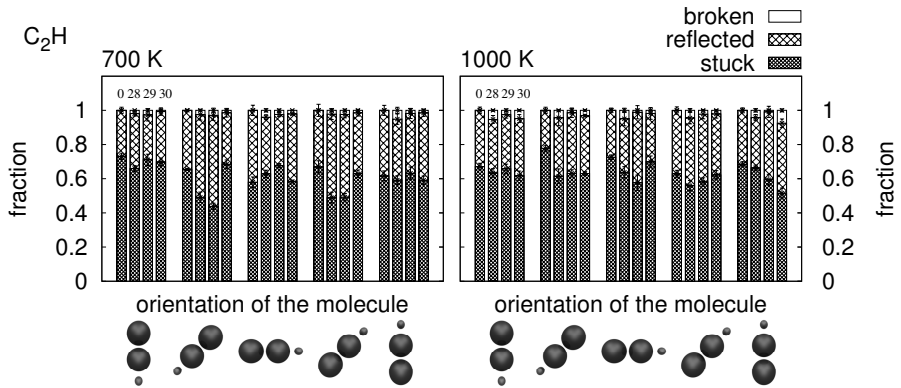


Fig. 7.9: As in Fig. 7.5 but for C_2H .

done so it will have difficulties exiting them. During this extended stay at the sample surface its reactive end may encounter a site to stick to. Hence, the more porous the surface the more likely is a hydrocarbon of a certain size to stick. Looking again at the pictures of the bombarded samples in Fig. 7.1 one may conclude that the C_2H will have the highest probability to stick on the sample that was bombarded with a hydrogen flux of $10^{28} m^{-2} s^{-1}$. It is the least likely to stick on the sample bombarded with $10^{30} m^{-2} s^{-1}$. The sticking increasing effect of a higher sp^2 fraction is compensated by the sticking decreasing effect of a less porous surface.

C_2H sticks a little better to the initial sample than to the bombarded samples. This is caused by the lower hydrogen contents of the initial sample which increases the reactivity of the surface.

The sticking probability of C_2H_2 on the bombarded samples is the lower the higher the flux the sample was subjected to. This can be seen in Fig. 7.10. The sticking probability appears to be inversely proportional to the sp^2 fraction of the sample.

C_2H_2 is a very stable molecule, not easily inclined to break its triple bond and engage in chemical bonds with other molecules. Continuing the line of thought we followed for C_2H we find that the apparent sticking probability of C_2H_2 is mainly determined by the effects of the porosity of the surface. Hence the sticking probability is the lowest on the least porous surface.

The relatively high sticking probability observed for the sample bombarded with $10^{28} m^{-2} s^{-1}$ might be caused by the simulation parameter choice: The hydrocarbon needs longer to escape from the pores than the simulation follows its trajectory. The very low sticking on the initial sample supports this notion, since this is a flat smooth surface and the effect of porosity is absent.

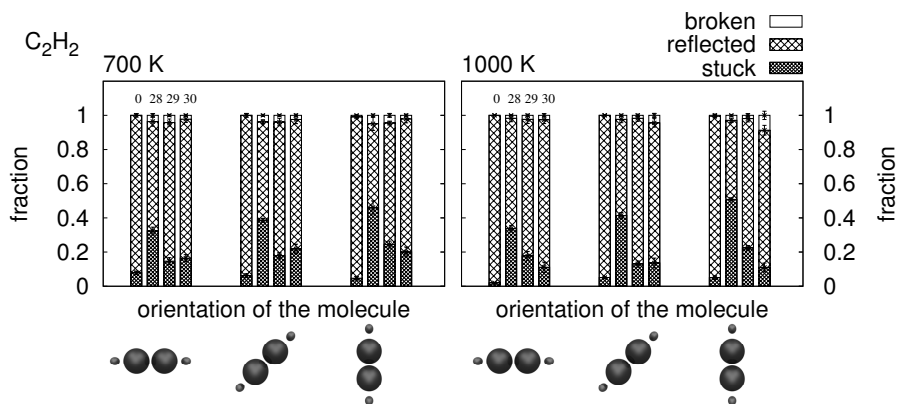


Fig. 7.10: As in Fig. 7.5 but for C_2H_2 .

7.3.3 Breaking of Hydrocarbons

Sticking on the surface is only one possible fate of a hydrocarbon hitting an a-C:H surface. It can also be reflected as a whole or in fragments after breaking up on the surface. Alternatively, some of the fragments stick, others return to the gas phase.

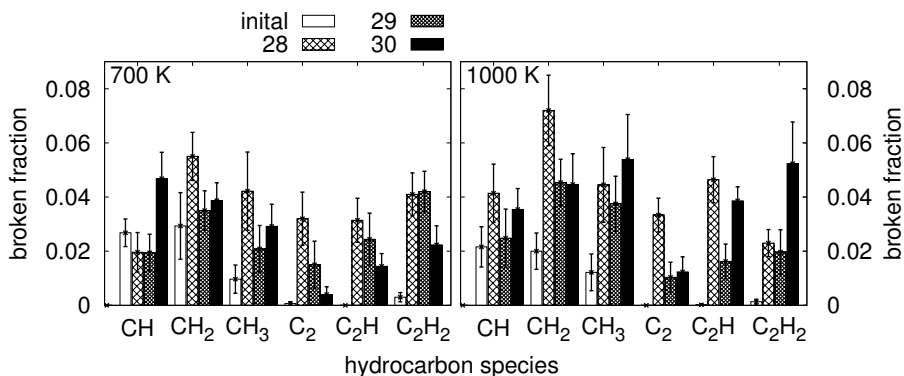


Fig. 7.11: The breaking probability of the selected hydrocarbons. They are shown for the various samples and both sample temperatures.

We now look at the fraction of the hydrocarbons that undergoes the fate of breaking up on impact and getting only partly reflected, that is, at least one of the fragments sticks to the surface and another returns to the gas phase. The breaking probability is shown in Fig. 7.11. The fraction that breaks up is fairly small, clearly less than 1%.

On the initial surface the hydrocarbons with one C atom show a decreasing breaking

probability (within error bars) with increasing number of H atoms. The more H atoms they have the more stable they are. This can be explained by the fact that the binding energy between C and H in a hydrocarbon increases with the number of H atoms bound to a C atom. The average binding energy between the C and H atom in CH is 3.5 eV, in CH₂ 4.2 eV and in CH₃ 4.4 eV [72].

Hydrocarbons with two C atoms hardly ever break on the initial surface, only C₂H₂ shows a small probability of 0.2%..

Overall, breaking is more likely on a surface that was subjected to hydrogen bombardment than on the initial surface. The higher sp² fraction may contribute by increasing the likelihood of hydrogen abstraction and the higher porosity of the bombarded surfaces increases the residence time of the hydrocarbon which increases the probability for a reaction.

For the breaking probability on the surfaces that were subjected to hydrogen bombardment there is no general trend discernible. Possibly the number of runs is too small to render sufficient statistics for such an unlikely event.

7.4 Conclusions

We have bombarded various a-C:H samples non-cumulatively with 10 eV hydrocarbons at two different temperatures of 700 and 1000 K. The samples were previously exposed to hydrogen atom bombardment of different fluxes, namely 10²⁸ m⁻²s⁻¹, 10²⁹ m⁻²s⁻¹ and 10³⁰ m⁻²s⁻¹. For comparison the initial sample was subjected to hydrocarbon bombardment as well.

The results of the simulations show that the sp² fraction in the a-C:H samples increases with the hydrogen flux they were subjected to. This higher sp² fraction leads to an increased sticking probability for the subsequently impinging hydrocarbons. Furthermore, the a-C:H samples were the less porous the higher the hydrogen flux they were subjected to previously. This increased the probability for larger species to get trapped in the pores increasing their residence time at the surface. This in turn caused a higher sticking coefficient for larger non-reactive hydrocarbons. For all hydrocarbons the probability to break on impact and leave a part sticking to the surface is very small, less than 1%. The higher degree of porosity of the surface subjected to an H flux can increase the probability of the molecule to break up on impact.

Summarising, our MD simulations show that the surface structure of the a-C:H material depends on the hydrogen flux it is subjected to: the higher the flux the higher is the fraction of sp² hybridised carbon. The higher this fraction the higher is the sticking probability of atomic carbon, the C₂ molecule and small reactive hydrocarbons on that surface. Additionally, at higher fluxes the plasma density is higher. This reduces the

mean free path for the erosion products in the plasma and increases the probability that they return to the surface. Combining this effect with our simulation results one can conclude that on divertor plates made from carbon material under high hydrogen flux more hydrocarbons stick than under a lower flux. Consequently, more of the erosion products are redeposited and do not enter the plasma. This result could be part of an explanation for the reduction of the carbon erosion yield with increasing flux as suggested by the experimental results shown in Fig. 6.1 by Roth et al. [13].

Chapter 8

Tungsten Carbide under Deuterium Bombardment

8.1 Introduction

In the previous chapters we presented results from the simulation of carbon material under hydrogen bombardment. In this section we turn to the other candidate material for the ITER divertor which is tungsten. In particular we will look at mixed materials consisting of carbon and tungsten. According to current design plans the divertor surface will partly be covered with carbon and partly with tungsten. Therefore the mixing of these materials is very likely when either is eroded, ionised in the plasma and thrown back at the divertor surface.

The group of Kai Nordlund in Helsinki updated the HPCARCAS code with the needed tungsten-carbon and tungsten-hydrogen potentials in 2005 [22]. Since then a number of MD simulations of tungsten have been conducted.

Salonen et al. [73] showed that the results of simulations of tungsten self sputtering agree well with experimental values. Henriksson et al. [74] simulated the sticking of hydrogen on a pure tungsten surface for H energies below 10 eV. Their simulations agreed with the experimentally found decrease of sticking with increasing H energy and the adsorption site in the simulations is in perfect agreement with experiments. Both studies verified the new potentials.

Henriksson et al. [74] simulated the irradiation of tungsten with helium atoms with energies of 50 to 200 eV at sample temperatures of 0 and 300 K. They found that the helium accumulated and forced the surrounding tungsten material out of the way to form clusters of up to 100 atoms at a depth of 5 to 6 Å. They also ran Monte Carlo simulations and found that the depth of the blister is a function of the He flux, the lower the flux the deeper the blister, indicating that diffusion plays an important role.

Träskelin et al. [75] simulated the bombardment of crystalline and amorphous tungsten carbide (10 to 50% carbon) with deuterium in the energy range of 50 eV to 2 keV. They found that under a bombardment with 100 eV deuterium the crystalline sample quickly

and to a larger depth than for other energies turned into an amorphous state. Furthermore, the carbon erosion yield from the amorphous samples is directly proportional to the carbon contents. However, they did not observe bubble formation which is likely due to the limited number of deuterium impacts they simulated.

Several experiments with deuterium plasma and carbon enriched deuterium plasma impinging on tungsten surfaces have been conducted.

Alimov et al. [14] exposed carbon implanted tungsten to a deuterium ion beam of 10 keV per D^+ . Compared to pure crystalline tungsten the retention of deuterium is lower in the carbon implanted tungsten. Furthermore, the deuterium is retained in the carbon containing regions with no diffusion out of this region, the deuterium is held in place by the carbon.

In a continuation of this work tungsten was exposed to low-energy deuterium of about 200 eV with and without carbon contamination of the beam [16]. Deuterium retention showed to be temperature dependent with a maximum at around 500 K for the pure deuterium plasma and 600 K for the carbon polluted plasma. They concluded that the tungsten carbide forming at the surface inhibits diffusion out of the material increasing retention of deuterium. Furthermore, they found deuterium accumulations or blisters at several μm depths, much deeper than the implantation depth of several nm.

Sze et al. [17] conducted experiments regarding carbon redeposition on tungsten. Tungsten was exposed to pure deuterium plasma and carbon enriched deuterium plasma of ion energies around 100 eV. They found that the retention depended on the substrate temperature (the higher the temperature the lower the retention) and the degree of the carbon contamination (more carbon means higher retention). Furthermore, they could determine that for a substrate temperature below 850 K most of the trapped deuterium formed D_2 whereas at higher temperatures the dominant species was atomic D.

In their review article Condon and Schober identify criteria for hydrogen bubble formation in metals [76]. Firstly, the hydrogen must be dissolved in a supersaturated condition. Supersaturation can among other ways be reached by hydrogen implantation if the implantation time scale is shorter than the diffusion time scale. If the level of supersaturation is below a certain level a large concentration of metal vacancies must be present to allow bubble formation. Above this saturation level the gas pressure is sufficiently high to form cavities. However, to obtain bubbles the supersaturation must remain below the concentration required for hydride formation.

The main goal of this study is to investigate whether the blistering of tungsten carbon mixtures which is observed in experiments can be recreated in MD simulations.

We bombarded amorphous mixtures of tungsten and carbon of different carbon per-

centages at different temperatures with deuterium atoms of an energy of 100 eV. This is at the high end of the energy range the hydrogen atoms are expected to have when hitting the divertor. A reason to choose this value was the finding of Träskelin et al. [75] that at this energy the crystalline sample amorphisises the fastest and the amorphised layer is the thickest. Hence, we expected shorter simulation times until bubbles formed.

The presented results include the carbon and tungsten erosion yields, the amount of deuterium retained in the materials and blistering.

8.2 Modelling

The MD code we used for our simulations is described in section 2.1.3.

The simulated samples consist of amorphous mixtures of carbon (C) and tungsten (W). The atomic carbon percentages are 15, 50 and 95%. All samples have 2440 atoms. The sizes of the samples are listed in Table 8.1. They vary because the atomic radii of C and W differ by a factor of two (about 0.7 Å for C and about 1.4 Å for W).

Table 8.1: Sizes of simulated tungsten carbide samples.

% C in sample	x / Å	y / Å	z / Å
15	24.8	24.2	62.5
50	21.6	22.8	67.8
95	19.8	21.2	65.0

The simulated temperatures of the samples are 700 and 1000 K. The deuterium atom energy is 100 eV and the angle of incidence parallel to the surface normal. Since the energy is well above the physical sputtering threshold for carbon material it may be expected that the erosion yields for off-normal angles are larger than the ones presented in this study [32]. The deuterium energy is too low to physically sputter tungsten [6].

The launching positions of the deuterium projectiles randomly vary in x- and y-direction (surface normal is z-direction). So, the samples are the same but the impact coordinates are different for every run.

In real life tungsten is very hard to cool once it has heated up. The same behaviour showed in the MD simulations. Frequent cooling cycles (that is, running an extra simulation round without bombardment) had to be applied to return the sample to the desired temperature. The cooling cycles started when the desired temperature was exceeded by 20%. The rise times for the thermostat are 5 and 10 fs.

Initially the plan was to simulate 15% carbon samples for both temperatures as well. The maintaining of 700 K in these samples required so many cooling cycles that the simulations went about a factor of 10 slower than the simulations of the higher carbon percentages. Only at 1000 K the bombardment simulation of a 15% carbon sample went fast enough, so some results of that run are presented here.

Because of the cooling cycles the time periods between impacts varied and consequently the deuterium flux on the samples varied between approximately 10^{28} and $1.5 \cdot 10^{29} \text{ m}^{-2}\text{s}^{-1}$ corresponding to a time of 20 to 1.5 ps, respectively, between deuterium impacts.

The variation in flux is not expected to have any influence on the results with regards to the erosion yields. In chapter 6 was shown that the flux dependency of the carbon erosion yield is caused by processes outside of the MD simulation realm.

Retention, however, is most likely affected, since diffusion and the flux of the incoming deuterium compete with each other. Expected is that the depth where the deuterium is retained is depending on the flux.

The number of deuterium impacts was 10000. For each of the four combinations of carbon percentage and sample temperature two simulations with two different rise times were run, so, in total four simulation runs per combination of C percentage and sample temperature.

8.3 Results

8.3.1 The 50% Carbon Sample

Retained deuterium and eroded carbon and tungsten

Fig. 8.1 shows the number of retained deuterium atoms and the number of eroded carbon and tungsten atoms as a function of the number of deuterium impacts. The figure consists of four panels each showing the results of one simulation run. In the top row the number of retained deuterium atoms, in the second row the number of eroded carbon atoms and in the bottom row the number of eroded tungsten atoms is plotted. The left column shows the quantities for the 700 K sample and the right column for 1000 K.

Since the plots of each individual simulation run are shown there are no error bars. Averaging over the values and calculating the standard deviation does not make sense since jumps in the results for the 50% carbon sample do not occur after the same number of deuterium impacts.

Fig. 8.1 shows that one of the general features is the following sequence of events: The retained amount of deuterium increases fast and steadily. About half of the impacting deuterium atoms is retained in the sample. Then the number drops steeply over a few impacts. In some instances a jump occurs in both the carbon and the tungsten erosion at the same time as the sudden decrease of the amount of retained deuterium occurs. This feature shows in all four panels for both temperatures.

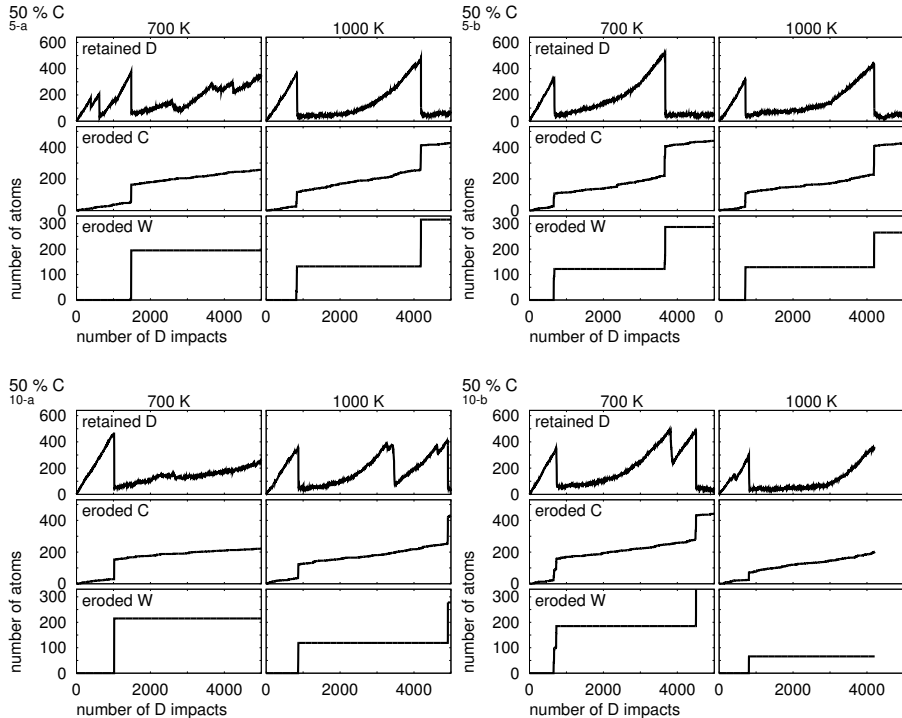


Fig. 8.1: In the four figures from top to bottom the number of retained deuterium atoms, the number of eroded C atoms and the number of eroded W atoms for the samples with 50% carbon contents are shown. Each plot is from one simulation run, so no error bars are available. The plots are for 700 K (left) and 1000 K (right). (The number-letter combinations 5-a, 5-b etc. printed underneath the carbon percentages are markers for the simulation run, the number gives the thermostat rise time in fs, the letter is just an index.)

Visualising the Bubble

Visual inspection of images created from the simulation results show that a deuterium blister formed that burst open releasing the retained deuterium and taking the piece

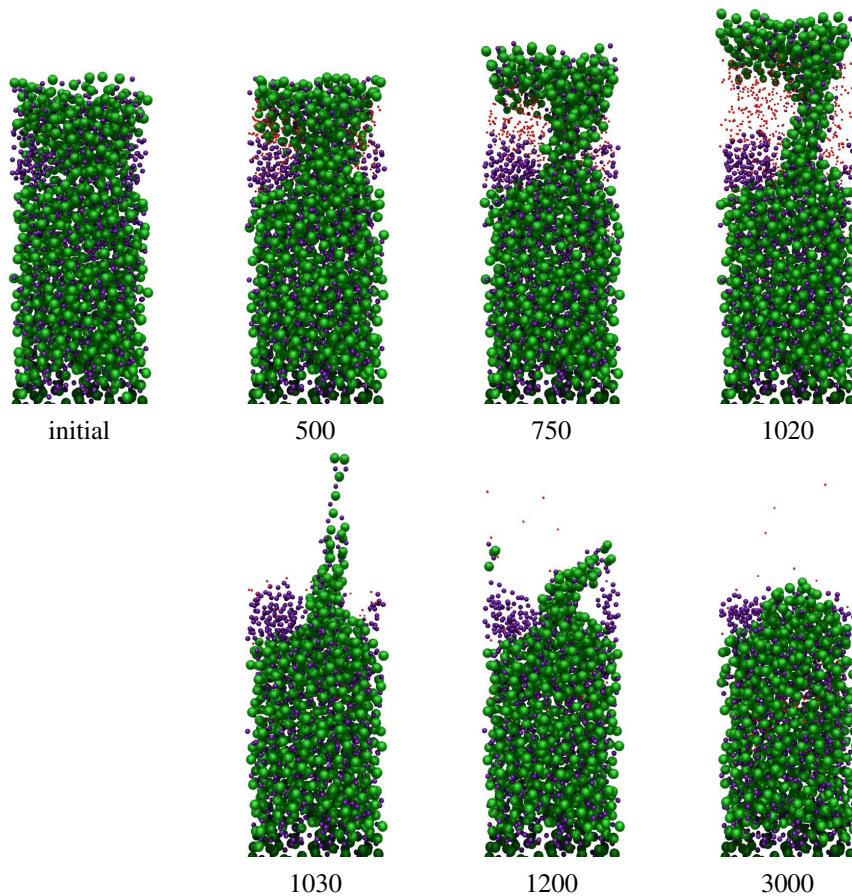


Fig. 8.2: Pictures made from the simulation results of a sample with 50% carbon at 700 K (run 10-a). The numbers indicate the number of deuterium impacts the sample has endured. The green spheres symbolise tungsten atoms, the blue ones carbon and the red ones deuterium.

of material that covered it with it. The images are shown for run 10-a in Fig. 8.2. The green spheres symbolise W atoms, the blue ones C atoms and deuterium atoms are shown as red spheres. The numbers at the bottom of the images refer to the number of D impacts the sample has been subjected to.

The images show that after 500 D impacts a clear accumulation of deuterium has formed under the top surface layer. During the following impacts the accumulation grows. When one looks carefully at the initial sample one finds that at the site where the bubble subsequently evolves a slight accumulation of carbon is present. This becomes

even clearer in the following snapshots. Between the 1020-th and 1030-th D impacts the bubble bursts and all the deuterium is released into the gas phase including the W-C material that covered the bubble. Now the carbon patch where the deuterium bubble nucleated on is clearly visible at the surface. Only the side wall of the bubble is left standing. This “finger” reaching up into the gas phase is gradually flattened under the subsequent deuterium impacts. Interestingly, there is no tungsten eroded during the flattening process or at any other time outside the blister popping. The carbon erosion on the other hand continues at the same rate as before the blister burst.

One of the requirements for bubble formation - as described by Condon and Schober [76] - is that the deuterium buildup happens on a time scale that is much shorter than the deuterium diffusion in the material. This is certainly the case in our simulations where the deuterium flux is larger than $10^{28} \text{ m}^{-2}\text{s}^{-1}$ and hence so high that the atoms accumulate at the implantation depth before they can diffuse away (the estimated typical diffusion length is 6 Å, see section 8.3.4).

As mentioned earlier, at the point where the deuterium bubble evolves a slight random accumulation of carbon is present in the initial sample, see Fig. 8.2. Apparently this random carbon enrichment served as nucleation site. The deuterium preferred to accumulate at the location of higher carbon concentration which makes sense because deuterium and carbon like to form a chemical bond but deuterium and tungsten do not. The chemical bond energies are listed in Table 8.2. This preference of the deuterium to stay in carbon enriched regions was already found in experiments by Alimov et al. [14].

Table 8.2: Chemical bond energies in eV.

	C	D	W
C	3.6 ^s 6.6 ^d 8.7 ^t	4.3	6.0
D	4.3	4.5	<1.0
W	6.0	<1.0	4.1

^s single, ^d double, ^t triple bond

Once a certain amount of deuterium has accumulated and supersaturation is reached the D atoms that are bound to carbon form D₂ molecules. Analysis of the simulation results shows that in the bubble mostly D₂ molecules are present. Inspecting the images in Fig. 8.2 gives the impression that the inner walls of the bubble are lined with deuterium atoms. It is conceivable that on the inner walls hydrogen abstraction processes as Langmuir-Hinshelwood, Eley-Rideal and hot-atom reactions take place. These processes were described in section 5.3.3 on page 44. The abandoned carbon binding sites are replenished by the ongoing deuterium bombardment.

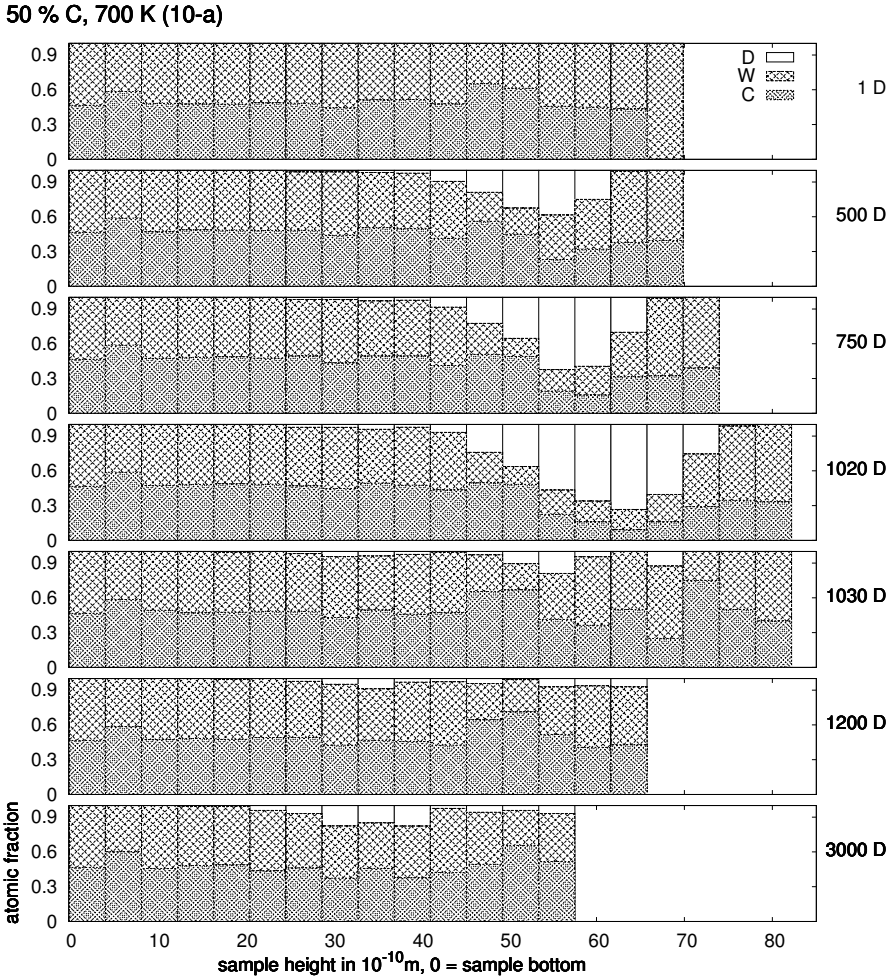


Fig. 8.3: A depth profile of the 50% carbon sample at 700 K (run 10-a, the same as in Fig. 8.2). The numbers to the right give the number of deuterium impacts the sample has been subjected to. The plots show the fraction of C, W and D atoms in the sample after the given number of D impacts. Note that after 1030 D impacts the filled bars at 70 to 80 Å consist of only a few atoms, see Fig. 8.2.

This process continues until the gas pressure becomes so high that W-C material is pushed aside and a gas bubble forms. The gas formation and volume increase associated with this process result in an increased entropy of the system [77] which favours

the formation of a gas bubble. The proximity of the sample surface allows bubble formation at lower deuterium gas pressures than would be required deeper in the bulk since the surface layers can give way easier, forming the dome shaped blisters which are also observed in experiments [16, 17]. Further growth of the bubble under continuing D bombardment leads to a point where the connecting material between bulk and bubble lid cannot withstand the pressure anymore and the blister bursts.

Fig. 8.3 shows depth profiles of a 50% carbon sample at 700 K (run 10-a, the same as in Fig. 8.2). The atomic fractions of carbon, tungsten and deuterium are shown as function of the sample depth. The carbon accumulation that most likely served as nucleation site for the bubble is visible in the first plot at around 50 Å sample height. One sees the deuterium accumulation and the bulging of the surface top layer giving way to the deuterium pressure. Between 1020 and 1030 D impacts the deuterium suddenly leaves the sample when the bubble bursts.

Most of the deuterium in the bubble are D_2 molecules. The number of D atoms to D_2 molecules is approximately 1:5 without dependency on the temperature. This is not in agreement with experiments where it was found that above about 850 K more D atoms are trapped than D_2 molecules [17]. The reason for this discrepancy is still unclear.

Additionally the fact that there are bubbles at all in samples that are hotter than 700 K differs from experimental findings with 200 eV deuterium energy [16] where no blister formation was observed on material this hot. However, experiments with 100 eV deuterium energy showed pit formation at temperatures higher than 800 K. The pits may have been caused by burst blisters [17]. MD simulations showed that deuterium of 200 eV energy have a shallower implantation depth than 100 eV deuterium [75]. Consequently, at elevated temperatures less blisters may form because the implanted deuterium can already at lower temperatures diffuse out of the sample.

Deuterium Buildup and Release without Bubble

The buildup of deuterium and its subsequent release is not always connected to bubble formation, bubble bursting and the loss of surface material. For example, in Fig. 8.1 on the bottom left panel (run 10-a) at a sample temperature of 1000 K deuterium is released from the sample after about 3000 D impacts but there is no jump in the numbers of eroded atoms. This out-gassing happens in other runs as well at both temperatures and for both thermostat rise times.

Fig. 8.4 shows the images from the simulation. In contrast to the previous case there is no deuterium bubble forming. Instead deuterium is dissolved in the material but supersaturation - required for bubble formation [76] - is not reached. In the sample where the bubble forms the D fraction reached 70% in some layers (Fig. 8.3) whereas in the other case where the deuterium is dissolved in the sample the D fraction reaches about

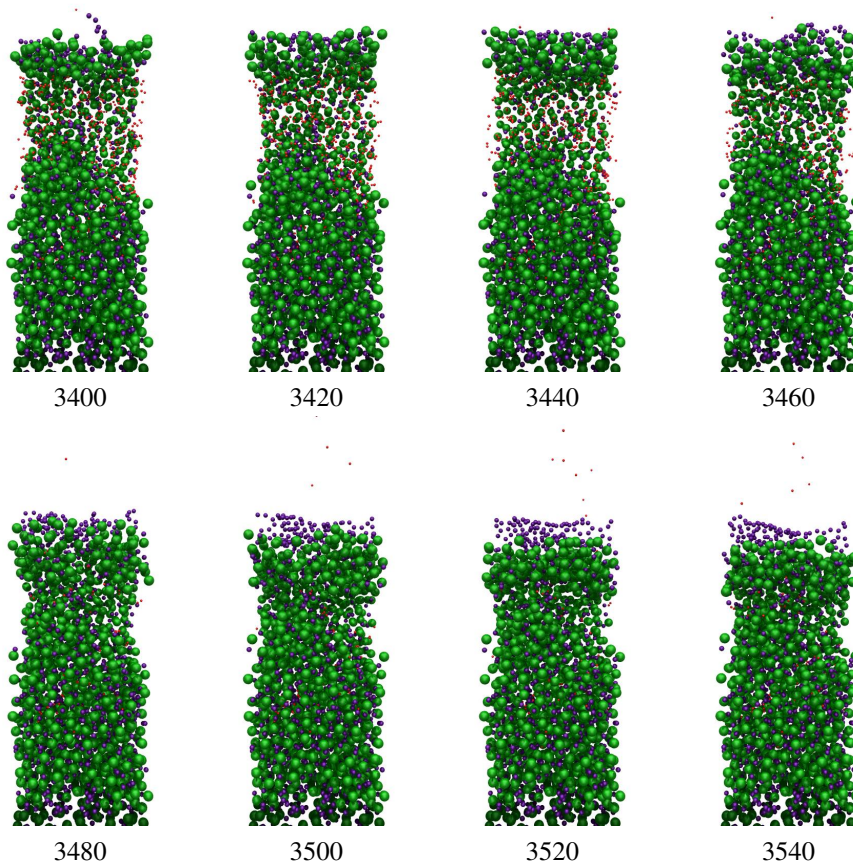


Fig. 8.4: Images made from the simulation results of a sample with 50% carbon at 1000 K (run 10-a). The numbers indicate the number of deuterium impacts the sample has endured. The green spheres symbolise tungsten atoms, the blue ones carbon and the red ones deuterium.

55% (Fig. 8.5). The deuterium leaves the sample gradually through the surface layers. A look at Fig. 8.1 reveals that the drop in the number of retained D atoms in run 10-a is less sudden than in the previously discussed bubble case.

Why does no bubble form? There are two differences between the samples that may have some influence. Firstly, whether or not there is a local carbon enrichment that serves as nucleation site for a deuterium bubble. Secondly, the composition of material covering the deuterium accumulation. A bubble forms when the deuterium can accumulate at one spot and the gas release is prevented.

50 % C, 1000 K (10-a)

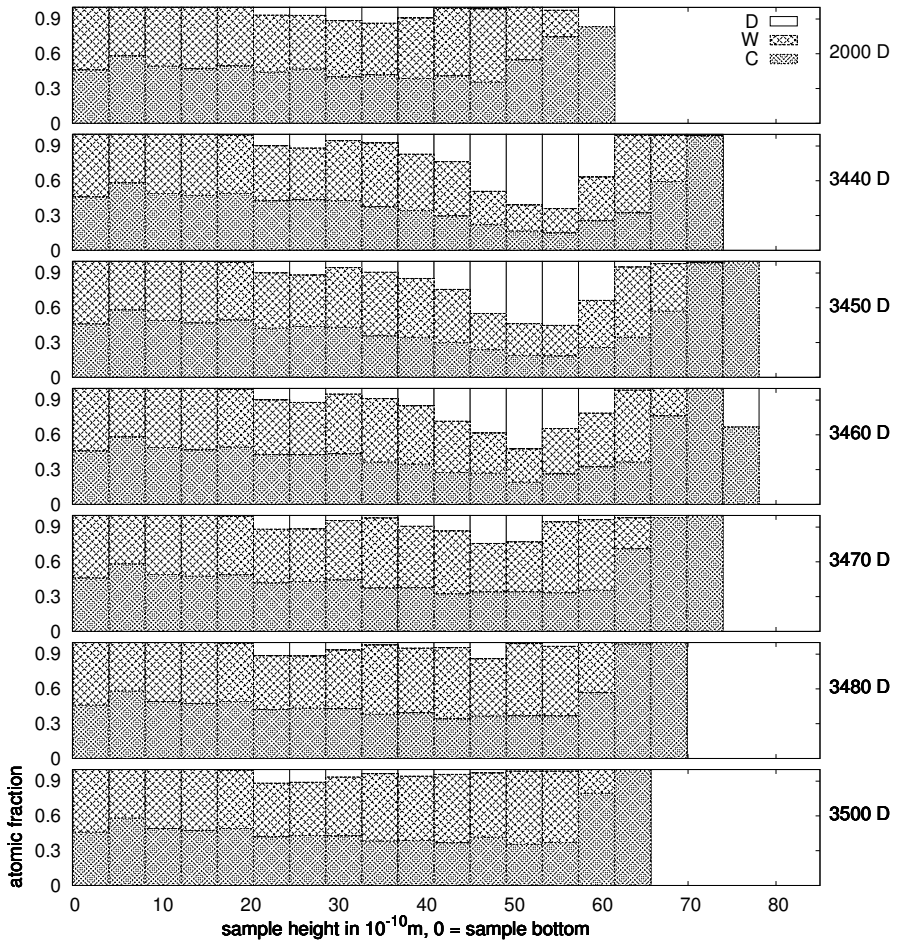


Fig. 8.5: Depth profiles of the 50% carbon sample at 1000 K (run 10-a, the same as in Fig. 8.4). The numbers to the right give the number of deuterium impacts the sample has been subjected to. The plots show the fraction of C, W and D atoms in the sample after the given number of D impacts.

In Fig. 8.5 the depth profiles are shown that belong to the images in Fig. 8.4. Again a large amount of deuterium is built up but it leaves the sample gradually over about 30 deuterium impacts and there is no material lost from the sample. Also here there is more D_2 present than D atoms in about the same ratio of 1 D atom per 5 D_2 as in the bubble.

8.3.2 The 95% Carbon Sample

In Fig. 8.6 the number of retained D and the number of eroded C and W are shown. There are no jumps in any of the plots of the individual simulation runs, therefore the averages are shown with their standard deviations. That there are no jumps indicates that there is no bubble bursting or other events that can suddenly change one of the shown quantities. In the images created from the simulation results shown in Fig. 8.7 one sees that there is no bubble formation in the sample.

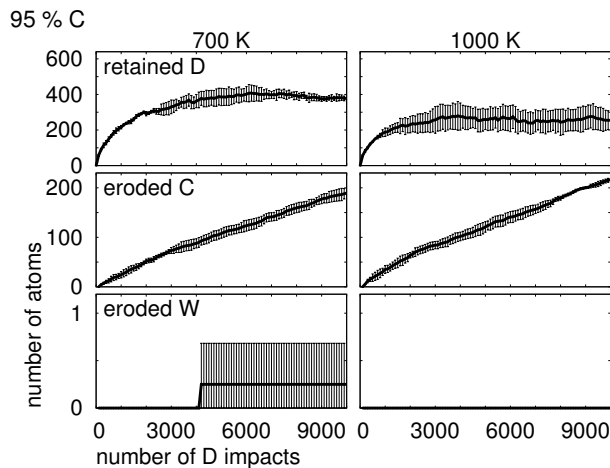


Fig. 8.6: The number of retained deuterium, eroded carbon and eroded tungsten for the sample with 95% carbon contents. The panels to the left show the results at 700 K, to the right at 1000 K. The plots show the averages over the four runs with their standard deviation.

The number of retained D atoms shows a strong temperature dependency. After 10000 D impacts the 700 K sample holds about 400 D atoms whereas the 1000 K sample holds only about half of that amount. The rate at which deuterium is retained is about the same for the two temperatures but saturation is reached earlier in the hotter sample.

The number of eroded tungsten is as good as zero. One stray W atom took off in one of the 700 K simulations.

The number of eroded carbon atoms is a bit larger for the 1000 K than for the 700 K sample. The erosion yield is about $2.3 \cdot 10^{-2}$ C atoms per D impacts for 1000 K and $1.9 \cdot 10^{-2}$ C atoms per D impacts for 700 K. These are lower values than for a-C:H and diamond (see chapters 6 and 5) under bombardment with H energies of 10 to 20 eV. Lower carbon erosion yields from carbon doped with silicon and carbides have been observed before in simulations and experiments [78, 79, 80]. In carbon doped

with titanium or tungsten carbide an enrichment of the surface with the dopant material has been observed [81, 82]. This enrichment at the surface appears to protect the underlying carbon material from erosion. However, the mechanism of the erosion yield reduction is not fully understood yet.

The accumulation of tungsten at the surface observed in experiments also happens in our simulations. However, in the simulation the accumulation takes a somewhat different shape: The sample produces a tungsten “pearl”. The tungsten atoms form a cluster and in the shown example the cluster moves to the top of the upper layer of the sample. It is connected to the sample by chemical bonds between some tungsten cluster atoms and surface carbon atoms. This happened in all four simulations at 700 K. In the 1000 K samples these “pearls” formed too, but not all of them moved to the top of the sample. In one case the tungsten accumulation happened in the bottom half of the sample. During the entire simulation time - in some cases up to 20000 D impacts - the “pearl” did not detach from the sample.

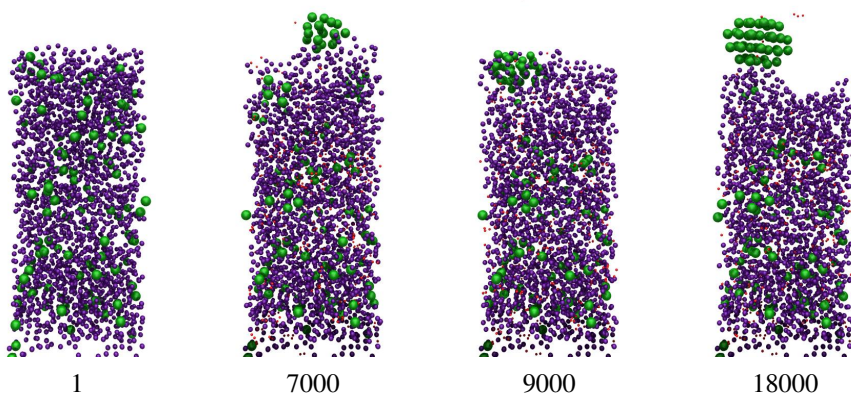


Fig. 8.7: Images made from the simulation results of a sample with 95% carbon at 700 K (run 5-a). The numbers indicate the number of deuterium impacts the sample has been subjected to. The green spheres symbolise tungsten atoms, the blue ones carbon and the red ones deuterium.

Fig. 8.8 shows the depth profiles of one of the 700 K samples with rise time 10 fs (run 5-a, one of the runs with 5 fs thermostat rise time). The deuterium is equally distributed throughout the sample and there is no accumulation as in the 50% carbon sample. What is remarkable though is the accumulation of tungsten at the surface of the sample.

A possible explanation could be that tungsten and a-C:H do not like to mix and that

the formation of tungsten nano-crystals is energetically more favourable. This sounds plausible when one assumes that a number of carbon atoms form double bonds which have a higher bond energy (6.6 eV) than W-C bonds (6.0 eV).

95 % C, 700 K (5-a)

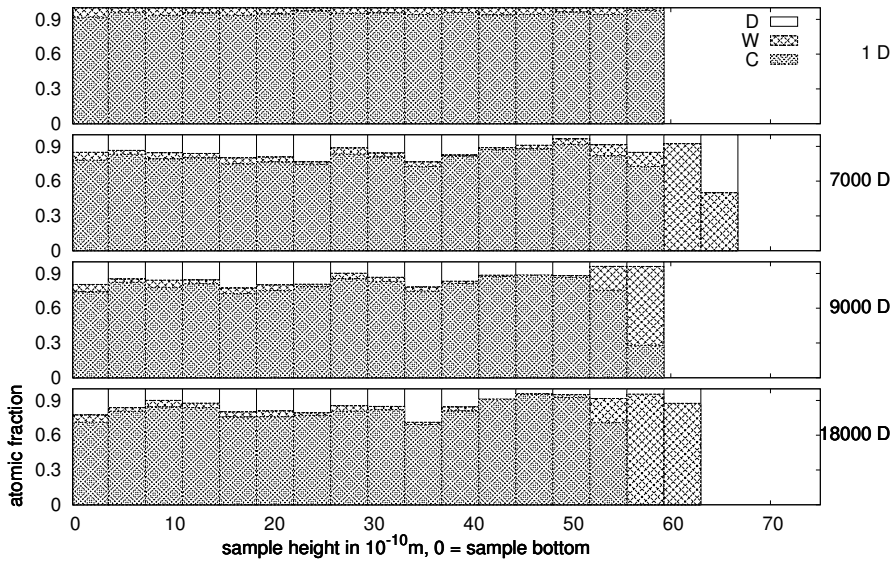


Fig. 8.8: Depth profiles of the 95% carbon sample at 700 K (run 5-a, the same as in Fig. 8.7). The numbers to the right give the number of deuterium impacts the sample has been subjected to. The plots show the fraction of C, W and D atoms in the sample after the given number of D impacts.

8.3.3 The 15% Carbon Sample

As mentioned in section 8.2 we simulated a 1000 K sample with 15% carbon. The results for deuterium retention, carbon and tungsten erosion are shown in Fig. 8.9. Comparing the results for deuterium retention with those for the 95% carbon sample in Fig. 8.6 one sees that the number of retained D atoms in the 15% carbon sample is only about half of that in the 95% carbon sample. This is in line with the experimental finding that a higher carbon contents means higher deuterium retention [14, 16, 17].

The carbon erosion yield is only about a third of the value in the sample with the higher carbon contents. During the simulations no tungsten is eroded.

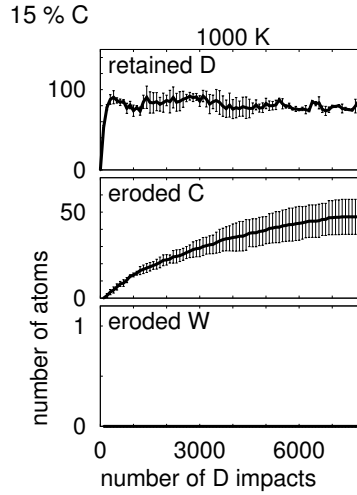


Fig. 8.9: The number of retained deuterium, eroded carbon and eroded tungsten for the sample with 15% carbon contents at 1000 K. The plots show the averages over the four runs with their standard deviation.

8.3.4 Bubble Depths

As visible in Figs. 8.3 and 8.5 the deuterium accumulations and bubbles appear at a depth of approximately 20 to 30 Å below the top layer. This is much closer to the top surface layer than measured in experiments where under bombardment with 200 eV deuterium bubbles form at several μm depth [16]. The flux in this experiment was about $10^{21} \text{ m}^{-2}\text{s}^{-1}$ which is seven to eight orders of magnitude lower than in the simulations. In the experiment the tungsten substrate was irradiated for about 30 minutes. The simulated time was less than a few 100 ns. Thus the fluence in the simulations is about 100 times lower than in the experiments.

In the experiments the implanted deuterium has ample time to diffuse further into the bulk and accumulate at larger depths. In the simulations the implanted deuterium has no time to move away from the implantation depth and the subsequent D atoms arrive in such fast succession that deuterium accumulates close to the surface top layer. The longest time between deuterium impacts in our simulations is 20 ps at a flux of $10^{28} \text{ m}^{-2}\text{s}^{-1}$, in the experiment [16] this time was about 10^7 times longer (for the same surface area) than in our simulations. The typical diffusion length l_D in three dimensions is given by:

$$l_D = \sqrt{6Dt} \quad (8.1)$$

where D is the diffusion coefficient and t the time. Filling in the time between impacts

$t=2 \cdot 10^{-4}$ s and a bubble depth of 2 μm from the experiments we arrive at a diffusion coefficient of $3 \cdot 10^{-9} \text{m}^2 \text{s}^{-1}$. This is lower than previously determined diffusion coefficients for deuterium in tungsten of about $3 \cdot 10^{-8} \text{m}^2 \text{s}^{-1}$ [83, 84]. This is to be expected since carbon has been identified as diffusion barrier, that is, its presence in the tungsten reduces the diffusion coefficient for deuterium [14, 16]. Calculating the typical diffusion length for the simulation time scale one arrives at $l_D = 6 \text{ \AA}$ which confirms the earlier made statement that implantation occurs faster than the diffusion time scale.

The shallow depth of the bubble is also an explanation for the short time before the bubble bursts. The proximity to the surface means that less deuterium gas pressure is required to burst the bubble, the top layers have no bulk material backing them so they easily bulge. Additionally, the higher flux in the simulations delivers deuterium in a much shorter time span such that bubbles can build up much faster. Therefore less fluence is required in the simulations to reproduce bubble formation.

In simulations by Henriksson et al. [74] helium bubbles formed at depths of 5 to 6 \AA . This is about a factor of 4 to 5 less than in our simulations. It is to be expected that the He has a smaller implantation depth because its energy in the simulations by Henriksson et al. [74] was half of that of our deuterium, its size is somewhat larger and the sample temperature was 300 K as opposed to 700 and 1000 K in our simulations.

8.3.5 Carbon and Tungsten Erosion Yields

Within the error bars there is no difference between the carbon or tungsten erosion yield for the two temperatures. The yields for the 15% carbon sample at 1000 K and for the 95% carbon sample at 700 and 1000 K are much lower than for the 50% carbon sample. This is caused by the propensity of the 50% carbon material to allow deuterium bubble formation. The bubbles burst open and in the process remove material from the sample.

Fig. 8.10 shows the carbon and tungsten erosion yields after 5000 deuterium atom impacts for the different simulated temperatures and carbon percentages.

At 1000 K the carbon erosion yield for the 95% carbon sample is with $24.8 \cdot 10^{-3}$ about three times that of the 15% carbon sample with $8.1 \cdot 10^{-3}$ C atoms per D impact. This agrees with the finding from MD simulations that a higher carbon contents means higher carbon erosion yields [75].

8.4 Conclusions

We simulated the deuterium bombardment of amorphous tungsten carbide samples with three different carbon percentages of 15, 50 and 95%. The D atoms had an energy

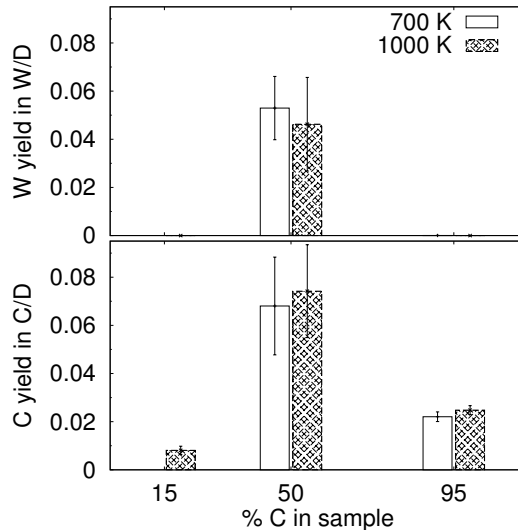


Fig. 8.10: The carbon and tungsten erosion yield after 5000 deuterium atom impacts. Note that there are no data available for the 15% carbon sample at 700 K.

of 100 eV and the sample temperatures of 700 and 1000 K.

We found that a higher carbon contents leads to higher deuterium retention and a higher temperature to a lower retention. This is in agreement with experiments.

The sample with 50% carbon is prone to blister formation, a phenomenon that occurs in experiments also for targets with lower carbon contents or of pure tungsten. Furthermore, in experiments the blisters form at far larger depths than in our simulations, several μm as opposed to several nm. The explanation is found in the factor of 10^7 to 10^8 larger fluxes in the simulations. The high flux allows accumulation of large amounts of deuterium at implantation depth in a very short time span before diffusion can disperse it.

Our simulations showed that local carbon enrichment serves as nucleation site for deuterium and can promote the formation of gas bubbles in the sample.

As in experiments the deuterium bubbles burst and sample material is jettisoned into the gas phase. However, the simulations also show a non-destructive way of deuterium release where the deuterium is gradually returned to the gas phase by seeping through the inter-atomic gaps leading to the top surface layer.

The 95% carbon sample under deuterium bombardment showed segregation of carbon and tungsten. Tungsten “pearls” of around 40 W atoms accumulated at the top of the sample only connected to the rest of the sample by a few chemical bonds to sample

C atoms. In one simulation run the accumulation took place at a larger depth in the sample. Segregation of carbon and tungsten has been observed in experiments with tungsten doped carbon subjected to deuterium bombardment. A possible explanation could be that tungsten and a-C:H do not like to mix and that the formation of tungsten nano-crystals is energetically more favourable.

The sample with 15% carbon at 1000 K showed no blister formation and a lower deuterium retention and carbon erosion than the other samples.

In general the results of the MD simulations agree with experimental results if one takes into account the limitations of the simulations to small samples, short time scales and high fluxes.

In the context of research for ITER the results of this study suggest that the material mix of carbon and tungsten behaves differently than the original pure materials. Deuterium retention in mixtures with a small or moderate amount of carbon does not play a large role. However, once the carbon contents exceeds a certain percentage these materials are prone to produce blisters that burst and contaminate the plasma with carbon and tungsten. Carbon rich materials, on the other hand, retain a lot of deuterium but higher surface temperatures can reduce the deuterium retention. Summarising, high temperatures, tungsten and little or no carbon appear preferable for the ITER divertor conditions.

Chapter 9

Conclusions & Outlook

This thesis presents a number of molecular dynamics studies of the hydrogen bombardment of carbon and tungsten materials. The motivation is to gain insight into the plasma surface interactions under conditions as they are expected at the divertor plates in the next step fusion device ITER and to complement experimental findings.

In general one may say that the results of MD simulations agree well with experimental results, given that one is careful to interpret the results within the limitations of the simulation method.

The MD simulations were conducted with two different versions of the same MD code called HCPARCAS. The simulations where only carbon and hydrogen were involved were conducted with the older version which incorporates the Brenner potential only. The last study was performed with a newer version where a tungsten-tungsten, tungsten-carbon and tungsten-hydrogen interaction potential had been added to the existing Brenner potential.

The first study is mainly about verifying that the results of the simulations agree with the potential corrected Baule model quantifying the sticking probability of hydrogen on a diamond surface as function of the hydrogen energy. The results agreed quantitatively with the model. Furthermore, agreement with experiments was found regarding the dependency of hydrogen retention on temperature and bombardment energy.

In the second study diamond and amorphous hydrogenated carbon (a-C:H) were bombarded with hydrogen. The results showed that in hotter material less hydrogen is retained and that a higher temperature leads to higher carbon erosion yields. Diamond retains more hydrogen and a-C:H has a higher carbon erosion yield. Additionally, the hot-atom and Langmuir-Hinshelwood processes were identified as the main channels to H₂ formation. The total carbon erosion yield increases with the temperature and the hydrogen energy. The eroded hydrocarbon species were determined and each species shows the same overall dependency on temperature and hydrogen energy as the total carbon erosion yield. The largest contribution to the erosion products were delivered by C, CH, CH₂ and C₂H₂. However, one has to bear in mind that the time scale of the MD simulations is limited. Experiments have shown that the diamond structure under hydrogen bombardment of H energies ≥ 10 eV changes to a a-C:H like structure at room

temperature and to a graphitic structure at higher temperatures. These graphitic layers are removed under subsequent exposure and possibly increase the carbon erosion yield to the same level as that of graphite or a-C:H.

Next the hydrogen flux dependency of the carbon erosion yield was studied. Results of experiments where carbon material was subjected to hydrogen suggest that the carbon erosion yield decreases with increasing flux roughly as one over the square root of the flux. We conducted MD simulations of a-C:H samples that were subjected to hydrogen fluxes of 10^{28} to 10^{30} $\text{m}^{-2}\text{s}^{-1}$. The simulation results showed no discernible flux dependency neither in the carbon erosion yield nor in the C:H ratio in the final samples. The main conclusion is that the effect that causes the reduction in the erosion yield measured in the experiments is not included in the MD simulations. Furthermore, a previously proposed relation between the hydrogen shielding effect caused by supersaturation and the reduction of the carbon erosion yield could be dismissed. This proposal assumes a dependency of the saturation degree on the flux. However, there was no difference in the hydrogen percentage in the samples after bombardment with different hydrogen fluxes.

Another suggested cause for the erosion yield reduction is redeposition where eroded hydrocarbons get ionised in the plasma and return to the surface following the magnetic field lines. This implies that redeposited material has a higher sticking probability on surfaces that have been subjected to higher fluxes. The bombarded samples from the previous study were taken as input configurations. It turned out that the porosity of the sample is depending on the previously administered flux, the lower the flux the more porous the surface. Furthermore, the sp^2/sp^3 ratio in the sample increased with the flux. For hydrocarbons with reactive sites this results in an increasing sticking probability with increasing flux - they bind to the CC double bonds. For less reactive species this results in a decreasing sticking probability with increasing flux because a lower porosity lowers the residence time and the probability to react. Overall our MD simulation results suggest that the sticking probability increases with the hydrogen flux a surface has been subjected to. This effect could be part of an explanation for the decreasing carbon erosion yield for increasing flux since less hydrocarbons move into the gas phase.

Lastly, an MD study of amorphous tungsten carbide under deuterium bombardment was performed. The main results were that a higher carbon content means a higher deuterium retention and that higher temperatures reduce the retention. Furthermore, deuterium blister formation - which is observed in experiments - was reproduced in an amorphous 50:50 tungsten carbide sample. Considering the high flux in the simulations the bubble depth agrees with experimental results. However, some of the simulation results were difficult to relate to experimental results. These are the formation of a tungsten "pearl" on top of a 95% carbon containing tungsten carbide sample and the

D atom to D_2 ratio in the bubble which was much higher than measured in experiments.

In the context of ITER the simulation results suggest that carbon surfaces may not be the most advisable choice for the divertor surfaces. Every studied carbon material showed properties with regards to hydrogen retention and carbon erosion that may be unacceptable. The alternative material tungsten shows more promising behaviour as long as it is kept hot enough and is not mixed with carbon. Cool tungsten which is contaminated with carbon and exposed to hydrogen plasma tends to form hydrogen blisters. Tungsten carbide material is jettisoned into the plasma when the blister bursts. Untamated tungsten at sufficiently high temperatures does not form blisters or retain large amounts of hydrogen.

We have seen that mixing two materials results in a material with a whole new set of properties. Looking at the plans for ITER we find that the main chamber wall is going to be covered with beryllium. This wall is not immune to erosion so ionised beryllium will make its way along the magnetic field lines down to the divertor and happily add to the material mixture on its surface. It may be expected that the resulting material will show some unexpected properties and it is currently unpredictable whether these will be desirable.

Having said that, it is blatantly clear that a lot of additional research into the area of mixed materials is necessary, both in experiments and in simulations. If one wants to conduct MD simulations, this requires the design of interaction potentials for beryllium and all the other players: carbon, tungsten and hydrogen. This is not an easy task and will require some time before a sufficiently validated version of the potentials is available.

There are also goals on a shorter time scale. It was already hinted in the previous chapters that rerunning of some of the simulations is required to gain more information on the fundamental processes taking place, for example, for determining the cross sections of the H_2 abstraction processes. Furthermore, the redeposition of hydrocarbons lends itself for further study. One can simulate cumulative bombardment and sample properly over the molecule orientation, giving them vibrational or rotational energy.

On a different track it is probably worthwhile to sort out why the ratio of D atoms to D_2 molecules in the bubbles in the simulated tungsten carbide differs so much from the ratio observed in the experiments and why there is no temperature dependency in the simulation results. The tungsten "pearl" also begs for an explanation.

Another path worth pursuing may be venturing into an area of MD simulations that is fairly new and not widely used: accelerated dynamics [85, 86].

We stumbled on something along those lines by accident caused by the peculiarity of the MD code to normalise the sides of the simulated box to one. Unintended by us, the

tungsten carbide sample was squeezed back to the size of the initial sample before every deuterium atom impact. Curiously, this resulted in bubble formation as well but much sooner than in the MD simulations presented here. This is of course wisdom of hindsight. When we found out about the squeezing, we did not think the simulation results could be accurate. This occurred too late in the course of the PhD project to be able to spend any time on studying the phenomenon. It may be a nice challenge for the next PhD student generation ...

Bibliography

- [1] M. P. Fewell. The atomic nuclide with the highest mean binding energy. *American Journal of Physics*, 63(7):653–658, 1995.
- [2] AMDC. Atomic mass data center, 2005. <http://www.nndc.bnl.gov/amdc/>.
- [3] A. W. Kley, N. J. Lopes Cardozo, and U. Samm. Plasma-surface interaction in the context of ITER. *Phys. Chem. Chem. Phys.*, 8:1761, 2006.
- [4] ITER - the way to new energy. <http://www.iter.org/>.
- [5] EFDA. European fusion development agreement. <http://www.jet.efda.org>.
- [6] Joachim Roth, E. Tsitrone, A. Loarte, Th. Loarer, G. Counsell, R. Neu, V. Philipps, S. Brezinsek, M. Lehnen, P. Coad, Ch. Grisolia, K. Schmid, K. Krieger, A. Kallenbach, B. Lipschultz, R. Doerner, R. Causey, V. Alimov, W. Shu, O. Ogorodnikova, A. Kirschner, G. Federici, and A. Kukushkin. Recent analysis of key plasma wall interactions issues for ITER. *Journal of Nuclear Materials*, 390-391:1 – 9, 2009. Proceedings of the 18th International Conference on Plasma-Surface Interactions in Controlled Fusion Device, Proceedings of the 18th International Conference on Plasma-Surface Interactions in Controlled Fusion Device.
- [7] A.S. Kukushkin, H.D. Pacher, V. Kotov, D. Reiter, D. Coster, and G.W. Pacher. Effect of neutral transport on ITER divertor performance. *Nuclear Fusion*, 45(7):608–616, 2005.
- [8] ITER Physics Expert Group on Divertor, ITER Physics Expert Group on Divertor Modelling, Database, and ITER Physics Basis Editors. Chapter 4: Power and particle control. *Nuclear Fusion*, 39(12):2391–2469, 1999.
- [9] Kathleen De Bleecker, Annemie Bogaerts, and Wim Goedheer. Modelling of nanoparticle coagulation and transport dynamics in dusty silane discharges. *New Journal of Physics*, 8(9):178, 2006.
- [10] J Winter. Dust in fusion devices - experimental evidence, possible sources and consequences. *Plasma Physics and Controlled Fusion*, 40(6):1201–1210, 1998.
- [11] A. Huber, V. Philipps, A. Pospieszczyk, A. Kirschner, M. Lehnen, T. Ohgo, K. Ohya, M. Rubel, B. Schweer, J. von Seggern, G. Sergienko, T. Tanabe, and M. Wada.

- Comparison of impurity production, recycling and power deposition on carbon and tungsten limiters in TEXTOR-94. *Journal of Nuclear Materials*, 290-293:276 – 280, 2001. 14th Int. Conf. on Plasma-Surface Interactions in Controlled Fusion Devices.
- [12] J. Westerhout, W. R. Koppers, W. A. J. Vijvers, R. S. Al, S. Brezinsek, S. Brons, H. J. N. van Eck, R. Engeln, B. de Groot, R. Koch, H. J. van der Meiden, M. P. Nuijten, V. Philipps, M. J. van de Pol, P. R. Prins, U. Samm, J. Scholten, D. C. Schram, B. Schweer, P. H. M. Smeets, D. G. Whyte, E. Zoethout, A. W. Kleyn, W. J. Goedheer, N. J. Lopes Cardozo, and G. J. van Rooij. PSI research in the ITER divertor parameter range at the FOM PSI-lab. *Physica Scripta*, T128:18–22, 2007.
- [13] J. Roth, A. Kirschner, W. Bohmeyer, S. Brezinsek, A. Cambe, E. Casarotto, R. Doerner, E. Gauthier, G. Federici, S. Higashijima, J. Hogan, A. Kallenbach, H. Kubo, J.M. Layet, T. Nakano, V. Philipps, A. Pospieszczyk, R. Preuss, R. Pugno, R. Ruggiéri, B. Schweer, G. Sergienko, and M. Stamp. Flux dependence of carbon erosion and implication for ITER. *Journal of Nuclear Materials*, 337-339:970 – 974, 2005. PSI-16.
- [14] V. Kh. Alimov, K. Ertl, J. Roth, and K. Schmid. Retention of ion-implanted deuterium in tungsten pre-irradiated with carbon ions. *Journal of Nuclear Materials*, 282(2-3):125 – 130, 2000.
- [15] V.Kh. Alimov and D.A. Komarov. Deuterium retention in carbon and tungsten-carbon mixed films deposited by magnetron sputtering in D_2 atmosphere. *Journal of Nuclear Materials*, 313-316:599 – 603, 2003. Plasma-Surface Interactions in Controlled Fusion Devices 15.
- [16] V.Kh. Alimov, J. Roth, R.A. Causey, D.A. Komarov, Ch. Linsmeier, A. Wiltner, F. Kost, and S. Lindig. Deuterium retention in tungsten exposed to low-energy, high-flux clean and carbon-seeded deuterium plasmas. *Journal of Nuclear Materials*, 375(2):192 – 201, 2008.
- [17] Fan C. Sze, Leo Chousal, Russ P. Doerner, and Stan Luckhardt. Growth of re-deposited carbon and its impact on isotope retention properties on tungsten in a high flux deuterium plasma. *Journal of Nuclear Materials*, 266-269:1212 – 1218, 1999.
- [18] Wenmin Wang, J. Roth, S. Lindig, and C. H. Wu. Blister formation of tungsten due to ion bombardment. *Journal of Nuclear Materials*, 299(2):124 – 131, 2001.
- [19] A. Kirschner, V. Philipps, J. Winter, and U. Kogler. Simulation of the plasma-wall interaction in a tokamak with the Monte Carlo code ERO-TEXTOR. *Nuclear Fusion*, 40(5):989–1001, 2000.
-

-
- [20] K. Nordlund, J. Keinonen, and T. Mattila. Formation of ion irradiation induced small-scale defects on graphite surfaces. *Phys. Rev. Lett.*, 77(4):699–702, Jul 1996.
- [21] E. D. de Rooij, U. von Toussaint, A. W. Kleyn, and W. J. Goedheer. Molecular dynamics simulations of amorphous hydrogenated carbon under high hydrogen fluxes. *Phys. Chem. Chem. Phys.*, 11(42):9823, 2009.
- [22] N. Juslin, P. Erhart, P. Träskelin, J. Nord, K. O. E. Henriksson, K. Nordlund, E. Salonen, and K. Albe. Analytical interatomic potential for modeling nonequilibrium processes in the W–C–H system. *Journal of Applied Physics*, 98(12):123520, 2005.
- [23] Yue-Lin Liu, Ying Zhang, G.-N. Luo, and Guang-Hong Lu. Structure, stability and diffusion of hydrogen in tungsten: A first-principles study. *Journal of Nuclear Materials*, 390-391:1032 – 1034, 2009. Proceedings of the 18th International Conference on Plasma-Surface Interactions in Controlled Fusion Device, Proceedings of the 18th International Conference on Plasma-Surface Interactions in Controlled Fusion Device.
- [24] Donald W. Brenner. Empirical potential for hydrocarbons for use in simulating the chemical vapor deposition of diamond films. *Phys. Rev. B*, 42:9458–9471, 1990.
- [25] Donald W. Brenner. Erratum: Empirical potential for hydrocarbons for use in simulating the chemical vapor deposition of diamond films. *Phys. Rev. B*, 46:1948, 1992.
- [26] Thorsten Pöschel and Thomas Schwager. *Computational granular dynamics: models and algorithms*. Springer, Berlin, 2005.
- [27] C. William Gear. *Numerical Initial Value Problems in Ordinary Differential Equations*. Prentice-Hall, Englewood Cliffs, New Jersey, 1971.
- [28] C. W. Gear. The numerical integration of ordinary differential equations of various orders. *Argonne National Laboratories Report*, #ANL-7126, 1966.
- [29] H. J. C. Berendsen, J. P. M. Postma, W. F. van Gunsteren, A. DiNola, and J. R. Haak. Molecular dynamics with coupling to an external bath. *The Journal of Chemical Physics*, 81(8):3684–3690, 1984.
- [30] S. C. Harvey, R. K.-Z. Tan, and T. E. Chaetham III. The flying ice cube: Velocity rescaling in molecular dynamics leads to violation of energy equipartition. *Journal of Computational Chemistry*, 19:726–740, 1998.
- [31] J. F. Ziegler, J. P. Biersack, and U. Littmark. *The Stopping and Range of Ions in Solids*. Pergamon Press, New York, 1985.
-

-
- [32] M. Küstner, W. Eckstein, E. Hechtel, and J. Roth. Angular dependence of the sputtering yield of rough beryllium surfaces. *Journal of Nuclear Materials*, 265:22–27, 1999.
- [33] Daan Frenkel and Berend Smit. *Understanding Molecular Simulation - 2nd edn.* Academic Press, 2002.
- [34] O. L. Mayorga, W. W. van Osdol, J. L. Lacombe, and E. Freire. Frequency spectrum of enthalpy fluctuations associated with macromolecular transitions. *PNAS*, 85:9514–9518, 1988.
- [35] P. Varga, W. Hofer, and H. Winter. Auger neutralization of multiply charged noble gas ions at a tungsten surface. *Surface Science*, 117:142–153, 1982.
- [36] L.C.A. van den Oetelaar, S.N. Mikhailov, and H.H. Brongersma. Mechanism of neutralization in low-energy He⁺ ion scattering from carbidic and graphitic carbon species on rhenium. *Nuclear Instruments and Methods in Physics Research Section B: Beam Interactions with Materials and Atoms*, 85:420–423, 1994.
- [37] J. Harris. *Dynamics of Gas-surface Interactions.* C.T. Rettner and M.N.R. Ashfold (Eds.) The Royal Society of Chemistry, 1991.
- [38] G. Federici, C.H. Skinner, J.N. Brooks, J.P. Coad, C. Grisolia, A.A. Haasz, A. Hasanein, V. Philipps, C.S. Pitcher, J. Roth, W.R. Wampler, and D.G. Whyte. Plasma-material interactions in current tokamaks and their implications for next step fusion reactors. *Nuclear Fusion*, 41(12):1967–2137, 2001.
- [39] Samuele Porro, Gregory De Temmerman, Steve Lisgo, Phillip John, Isabela Villalpando, Jerry W. Zimmer, Bob Johnson, and John I.B. Wilson. Nanocrystalline diamond coating of fusion plasma facing components. *Diamond and Related Materials*, 18(5-8):740 – 744, 2009. Proceedings of Diamond 2008, the 19th European Conference on Diamond, Diamond-Like Materials, Carbon Nanotubes, Nitrides and Silicon Carbide.
- [40] E. Salonen, K. Nordlund, J. Keinonen, and C. H. Wu. Swift chemical sputtering of amorphous hydrogenated carbon. *Phys. Rev. B*, 63(19):195415, Apr 2001.
- [41] B. Baule. Theoretische Behandlung der Erscheinungen in verdünnten Gasen. *Journal of Nuclear Materials*, 349(9):145 – 176, 1914.
- [42] Gary Attard and Colin Barnes. *Surfaces.* Oxford University Press, 2006.
- [43] C. M. Donnelly, R. W. McCullough, and J. Geddes. Etching of graphite and diamond by thermal energy hydrogen atoms. *Diamond and Related Materials*, 6(5-7):787 – 790, 1997.
-

-
- [44] M. Schlüter, C. Hopf, T. Schwarz-Selinger, and W. Jacob. Temperature dependence of the chemical sputtering of amorphous hydrogenated carbon films by hydrogen. *Journal of Nuclear Materials*, 376(1):33 – 37, 2008.
- [45] J.W. Davis, A.A. Haasz, and P.C. Stangeby. Hydrocarbon formation due to combined H^+ ion and H^0 atom impact on pyrolytic graphite. *Journal of Nuclear Materials*, 155-157(Part 1):234 – 240, 1988.
- [46] Y. Yamazaki, K. Ishikawa, N. Mizuochi, and S. Yamasaki. Structural change in diamond by hydrogen plasma treatment at room temperature. *Diamond and Related Materials*, 14(11-12):1939 – 1942, 2005. Proceedings of the 10th International Conference on New Diamond Science and Technology (ICNDST-10) - ICNDST-10 Special Issue.
- [47] Y. Yamazaki, K. Ishikawa, N. Mizuochi, and S. Yamasaki. Structure of diamond surface defective layer damaged by hydrogen ion beam exposure. *Diamond and Related Materials*, 15(4-8):703 – 706, 2006. Diamond 2005.
- [48] P. N. Maya, U. von Toussaint, and C. Hopf. Synergistic erosion process of hydrocarbon films: a molecular dynamics study. *New Journal of Physics*, 10(2):023002 (15pp), 2008.
- [49] A. C. Ferrari, A. Libassi, B. K. Tanner, V. Stolojan, J. Yuan, L. M. Brown, S. E. Rodil, B. Kleinsorge, and J. Robertson. Density, sp^3 fraction, and cross-sectional structure of amorphous carbon films determined by X-ray reflectivity and electron energy-loss spectroscopy. *Phys. Rev. B*, 62(16):11089–11103, Oct 2000.
- [50] B. Jackson and D. Lemoine. Eley-Rideal reactions between H atoms on metal and graphite surfaces: The variation of reactivity with substrate. *Journal of Chemical Physics*, 114:474, 2001.
- [51] B. V. Mech, A. A. Haasz, and Davis J. W. Model for the chemical erosion of graphite due to low energy H^+ and D^+ impact. *Journal of Applied Physics*, 84:1655, 1998.
- [52] E. Salonen, K. Nordlund, J. Tarus, T. Ahlgren, and J. Keinonen. Suppression of carbon erosion by hydrogen shielding during high-flux bombardment. *Phys. Rev. B*, 60(20):R14005–R14008, 1999.
- [53] Jürgen Küppers. The hydrogen surface chemistry of carbon as a plasma facing material. *Surface Science Reports*, 22(7-8):249 – 321, 1995.
- [54] M. Wittmann and J. Küppers. A model of hydrogen impact induced chemical erosion of carbon based on elementary reaction steps. *Journal of Nuclear Materials*, 227(3):186 – 194, 1996.
-

-
- [55] D.P. Woodruff, editor. *Surface Dynamics: Volume 11 (The Chemical Physics of Solid Surfaces)*. Elsevier Science, 2003.
- [56] Ziya B. Guvenc, Xianwei Sha, and Bret Jackson. The Effects of Lattice Motion on Eley-Rideal and Hot Atom Reactions: Quasiclassical Studies of Hydrogen Recombination on Ni(100). *The Journal of Physical Chemistry B*, 106:8342, 2002.
- [57] J. Roth, R. Preuss, W. Bohmeyer, S. Brezinsek, A. Cambe, E. Casarotto, R. Doerner, E. Gauthier, G. Federici, S. Higashijima, J. Hogan, A. Kallenbach, A. Kirschner, H. Kubo, J.M. Layet, T. Nakano, V. Philipps, A. Pospieszczyk, R. Pugno, R. Ruggiéri, B. Schweer, G. Sergienko, and M. Stamp. Flux dependence of carbon chemical erosion by deuterium ions. *Nuclear Fusion*, 44(11):L21–L25, 2004.
- [58] P. Träskelin, K. Nordlund, and J.Keinonen. H, He, Ne, Ar-bombardment of amorphous hydrocarbon structures. *Journal of Nuclear Materials*, 357:1–8, 2006.
- [59] W. Jacob and J. Roth. *Sputtering by Particle Bombardment, Experiments and Computer Calculations from Threshold to MeV Energies*. R. Behrisch and W. Eckstein (Eds.) Springer, Berlin, 2007.
- [60] Toshiyuki Nakamiya, Shinichi Aouib, and Kenji Ebiharac. Experimental and numerical study on pulsed-laser annealing process of diamond-like carbon thin films. *Diamond and Related Materials*, 10(3-7):905–909, March 2001.
- [61] W. Hurler, M. Pietralla, and A. Hammerschmidt. Determination of thermal properties of hydrogenated amorphous carbon films via mirage effect measurements. *Diamond and Related Materials*, 4:954–957, 1995.
- [62] M. Hakorvita, J.E. Vuorinen, X.M. He, M. Nastasi, and R.B. Schwarz. Heat capacity of hydrogenated diamond-like carbon films. *Applied Physics Letters*, 77(15):2340, 2000.
- [63] A. C. Ferrari, J. Robertson, R. Pastorelli, M. G. Beghi, and C. E. Bottani. *Elastic Constants of Diamond-Like Carbon Films by Surface Brillouin Scattering in Thin Films - Stresses and Mechanical Properties VIII*, edited by R. Vinci, O. Kraft, N. Moody, P. Besser, and E. Shaffer II. Mater. Res. Soc. Symp. Proc. Volume 594, Warrendale, PA, 2000, 2000.
- [64] J. Roth and C. Garcia-Rosales. Analytic description of the chemical erosion of graphite by hydrogen ions. *Nuclear Fusion*, 36(12):1647–59, 1996.
- [65] U. von Toussaint, P. N. Maya, and C. Hopf. Molecular dynamics modeling of chemical erosion of hydrocarbon films. *Journal of Nuclear Materials*, 386-388:353, 2009.
-

-
- [66] R. M. A Heeren, D. Ćirić, Hopman, H. J., and A. W. Kleyn. Enhanced preferential sputtering of a hydrogenated barium surface. *Appl. Phys. Lett.*, 59:158, 1991.
- [67] A. R. Sharma, R. Schneider, U. Toussaint, and K. Nordlund. Hydrocarbon radicals interaction with amorphous carbon surfaces. *Journal of Nuclear Materials*, 363-365:1283 – 1288, 2007. Plasma-Surface Interactions-17.
- [68] D.A. Alman and D.N. Ruzic. Molecular dynamics simulation of hydrocarbon reflection and dissociation coefficients from fusion-relevant carbon surfaces. *Physica Scripta*, T111:145–151, 2004.
- [69] P. Träskelin, E. Salonen, K. Nordlund, J. Keinonen, and C. H. Wu. Molecular dynamics simulations of CH₃ sticking on carbon surfaces, angular and energy dependence. *Journal of Nuclear Materials*, 334(1):65 – 70, 2004.
- [70] Achim von Keudell. Formation of polymer-like hydrocarbon films from radical beams of methyl and atomic hydrogen. *Thin Solid Films*, 402(1-2):1 – 37, 2002.
- [71] P. Träskelin, O. Saresoja, and K. Nordlund. Molecular dynamics simulations of C₂, C₂H, C₂H₂, C₂H₃, C₂H₄, C₂H₅, and C₂H₆ bombardment of diamond (111) surfaces. *Journal of Nuclear Materials*, 375(2):270 – 274, 2008.
- [72] Stephen J. Blanksby and G. Barney Ellison. Bond dissociation energies of organic molecules. *Accounts of Chemical Research*, 36:255–263, 2003.
- [73] E. Salonen, K. Nordlund, J. Keinonen, and C.H. Wu. Molecular dynamics studies of the sputtering of divertor materials. *Journal of Nuclear Materials*, 313-316:404 – 407, 2003. Plasma-Surface Interactions in Controlled Fusion Devices 15.
- [74] K.O.E. Henriksson, K. Nordlund, and J. Keinonen. Molecular dynamics simulations of helium cluster formation in tungsten. *Nuclear Instruments and Methods in Physics Research Section B: Beam Interactions with Materials and Atoms*, 244(2):377 – 391, 2006.
- [75] P. Träskelin, N. Juslin, P. Erhart, and K. Nordlund. Molecular dynamics simulations of hydrogen bombardment of tungsten carbide surfaces. *Physical Review B (Condensed Matter and Materials Physics)*, 75(17):174113, 2007.
- [76] J.B. Condon and T. Schober. Hydrogen bubbles in metals. *Journal of Nuclear Materials*, 207:1 – 24, 1993.
- [77] Charles Kittel and Herbert Kroemer. *Thermal Physics (2nd Edition)*. W. H. Freeman, 1980.
-

-
- [78] E. Salonen, K. Nordlund, J. Keinonen, and C. H. Wu. Chemical sputtering of amorphous silicon carbide under hydrogen bombardment. *Applied Surface Science*, 184(1-4):387 – 390, 2001.
- [79] C. H. Wu, C. Alessandrini, R. Moormann, M. Rubel, and B. M. U. Scherzer. Evaluation of silicon doped cfc's for plasma facing material. *Journal of Nuclear Materials*, 220-222:860 – 864, 1995. Plasma-Surface Interactions in Controlled Fusion Devices.
- [80] R. Schwörer, H. Plank, and J. Roth. Surface modifications and erosion yields of silicon and titanium doped graphites due to low energy D⁺ bombardment. *Journal of Nuclear Materials*, 230(3):208 – 213, 1996.
- [81] M. Balden, C. García-Rosales, R. Behrisch, J. Roth, P. Paz, and J. Etxeberria. Chemical erosion of carbon doped with different fine-grain carbides. *Journal of Nuclear Materials*, 290-293:52 – 56, 2001. 14th Int. Conf. on Plasma-Surface Interactions in Controlled Fusion Devices.
- [82] C. García-Rosales, I. López-Galilea, N. Ordás, C. Adelhelm, M. Balden, G. Pintsuk, M. Grattarola, and C. Gualco. Ti-doped isotropic graphite: A promising armour material for plasma-facing components. *Journal of Nuclear Materials*, 386-388:801 – 804, 2009. Fusion Reactor Materials, Proceedings of the Thirteenth International Conference on Fusion Reactor Materials.
- [83] R. Frauenfelder. Solution and diffusion of hydrogen in tungsten. *Journal of Vacuum Science and Technology*, 6(3):388–397, 1969.
- [84] M. Fukumoto, H. Kashiwagi, Y. Ohtsuka, Y. Ueda, M. Taniguchi, T. Inoue, K. Sakamoto, J. Yagyu, T. Arai, I. Takagi, and T. Kawamura. Deuterium trapping in tungsten damaged by high-energy hydrogen ion irradiation. *Journal of Nuclear Materials*, 390-391:572 – 575, 2009. Proceedings of the 18th International Conference on Plasma-Surface Interactions in Controlled Fusion Device, Proceedings of the 18th International Conference on Plasma-Surface Interactions in Controlled Fusion Device.
- [85] Arthur F. Voter, Francesco Montalenti, and Timothy C. Germann. Extending the time scale in atomistic simulation of materials. *Annual Review of Materials Research*, 32(1):321–346, 2002.
- [86] A.F. Voter. Arthur F. Voter's Home Page. <http://www.t12.lanl.gov/home/afv/>.
- [87] Rechenzentrum Garching. <http://www.rzg.mpg.de/>.
- [88] SARA - Computing & Networking Services. http://www.sara.nl/index_eng.html.
-

List of Publications

Journals

- Molecular dynamics simulations of amorphous hydrogenated carbon under high hydrogen fluxes
E. D. de Rooij, U. von Toussaint, A. W. Kleyn and W. J. Goedheer
Physical Chemistry Chemical Physics, 11(42):9823, 2009

Posters

- Sticky Grooves and Groovy Sticking:
MD Simulations of Hydrogen Interacting with Rough Carbon Surfaces
E.D. de Rooij, E. van Eijk, W.J. Goedheer, E. Neyts
CPS conference - Research Centre for Plasma Physics and Radiation Technology, Lunteren, The Netherlands, March 2006
- Molecular Dynamics Simulations of Hydrogen interacting with Carbon-surfaces under ITER-like Conditions
E.D. de Rooij, E. van Eijk, A.W.Kleyn, W.J. Goedheer
PFMC-11, Plasma Facing Materials and Components for Fusion Applications, Greifswald, Germany, October 2006
- Molecular Dynamics Simulations of Hydrogen interacting with Carbon-surfaces under ITER-like Conditions
E.D. de Rooij, A.W.Kleyn, W.J. Goedheer
WELTPP-9, The 9th Workshop on the Exploration of Low Temperature Plasma Physics, Rolduc, Kerkrade, The Netherlands, November 2006
- Hydrogen retention in diamond
E.D. de Rooij, A.W.Kleyn, W.J. Goedheer
13th International Conference on Surfaces Science (ICSS), Stockholm, Sweden, July 2007
- Hydrogen retention in diamond
E.D. de Rooij, A.W.Kleyn, W.J. Goedheer
Gordon Research School (GRC) - Dynamics at Surfaces, Andover, New Hampshire, USA, August 2007

- Hydrogen retention in diamond
E.D. de Rooij, A.W.Kleyn, W.J. Goedheer
7th Carolus Magnus Summer School on Plasma and Fusion Energy Physics,
Bad Honnef, Germany, September 2007
- Amorphous carbon surfaces under high hydrogen fluxes
E.D. de Rooij, U. von Toussaint, A.W.Kleyn, W.J. Goedheer
CPS conference - Research Centre for Plasma Physics and Radiation Technol-
ogy, Lunteren, The Netherlands, March 2008
- Amorphous carbon surfaces under high hydrogen fluxes
E.D. de Rooij, U. von Toussaint, A.W.Kleyn, W.J. Goedheer
shared with: "Carbon chemical erosion yield at ITER relevant plasma fluxes", J.
Westerhout
18th International Conference on Plasma Surface Interactions, Toledo, Spain,
May 2008
- Amorphous carbon surfaces under high hydrogen fluxes
E.D. de Rooij, U. von Toussaint, A.W.Kleyn, W.J. Goedheer
13th European Summer School "Low Temperature Plasma Physics: Basics and
Applications", Bad Honnef, Germany, October 2008
- Amorphous carbon surfaces under high hydrogen fluxes
E.D. de Rooij, U. von Toussaint, A.W.Kleyn, W.J. Goedheer
WELTPP-11, The 11th Workshop on the Exploration of Low Temperature Plasma
Physics, Rolduc, Kerkrade, The Netherlands, November 2006
- Fusion-relevant surfaces under extremely high hydrogen fluxes
E.D. de Rooij, U. von Toussaint, A.W.Kleyn, W.J. Goedheer
Physics@FOM, Velthoven, The Netherlands, January 2009
- Molecular Dynamics simulations of amorphous tungsten-carbide under deuterium
bombardment
E.D. de Rooij, U. von Toussaint, A.W.Kleyn, W.J. Goedheer
PFMC-12, Plasma Facing Materials and Components for Fusion Applications,
Jülich, Germany, May 2009

Presentations

- Hydrogen retention in diamond
E.D. de Rooij
Pre-colloquium at FOM Institute for Plasma Physics Rijnhuizen, Nieuwegein,
The Netherlands, February 2007
-

- Hydrogen retention in diamond
E.D. de Rooij
CPS conference - Research Centre for Plasma Physics and Radiation Technology, Lunteren, The Netherlands, March 2007
 - Hydrogen interacting with fusion relevant materials
E.D. de Rooij
Joint FOM Rijnhuizen/ FZ Jülich meeting, Nieuwegein, The Netherlands, March 2009
 - Hydrogen interacting with fusion relevant materials
E.D. de Rooij
IPP Bereichsseminar (department meeting), Max-Planck-Institute for Plasma Physics, Garching, Germany, March 2009
-

Computing Facilities

The calculations necessary to realise the studies described in this thesis were conducted at the “Rechenzentrum Garching” of the Max-Planck-Gesellschaft and IPP in Germany [87] and at “Sara Computing & Networking Services” in Amsterdam, The Netherlands [88]. At Sara the Lisa cluster and the Grid facilities were used. The Grid consists of a network of several computing facilities in the Netherlands and Belgium usually located at universities.

The configurations are as follows:

Sara national compute cluster Lisa (status of December 2009)

- 571 compute nodes:
 - 419 equipped with
 - . 2 Intel[®] Xeon[™] processors
 - . 3.4 GHz, Extended Memory 64 Technology (EM64T)
 - . 800 MHz Front Side Bus
 - . Gigabit Ethernet adapter for maintenance
 - 120 equipped with
 - . Intel[®] quad-core Xeon[™] E5345 processors
 - . 2.33 GHz
 - . Extended Memory 64 Technology (EM64T)
 - . 1330 MHz Front Side Bus
 - . Gigabit Ethernet adapter for maintenance
 - 32 equipped with
 - . 2 Intel[®] quad-core Xeon[™] L5420 processors
 - . 2.5 GHz
 - . Extended Memory 64 Technology (EM64T)
 - . 1330 MHz Front Side Bus
 - . Gigabit Ethernet adapter for maintenance
- Topspin InfiniBand network:
 - . Bandwidth: 800 MB/sec
 - . Latency: < 6 μ sec
- Qlogic InfiniBand network:
 - . Bandwidth: 1600 MB/sec
 - . Latency: < 6 μ sec
- Total peak performance: 11.5 TFlop/sec

- Disk space: 25 TB SUN[®]Thor systems for the home file systems
- Operating system: Debian Linux 32bit and 64bit

Rechenzentrum Garching

- IBM Blade Center HS21
 - Intel[®] Dual Core 5160 processors
 - . 3 GHz
 - . 1333 MHz Front Side Bus
 - . 4 MB L2 cache
 - PC2-5300 667 MHz ECC DDR2 FBDIMM memory
 - Gigabit-Ethernet-Interconnect
-

Summary

In a thermonuclear reactor fusion between hydrogen isotopes takes place, producing helium and energy. The so-called divertor is the part of the fusion reactor vessel where the plasma is neutralized in order to exhaust the helium. The surface plates of the divertor are subjected to high heat loads and high fluxes of energetic hydrogen and helium. In the next generation fusion device - the tokamak ITER - the expected conditions at the plates are particle fluxes exceeding 10^{24} per second and square metre, particle energies ranging from 1 to 100 eV and an average heat load of 10 MW per square metre. Two materials have been identified as candidates for the ITER divertor plates: carbon and tungsten. Since there are currently no fusion devices that can create these harsh conditions, it is unknown how the materials will behave in terms of erosion and hydrogen retention.

To gain more insight in the physical processes under these conditions molecular dynamics simulations have been conducted. Since diamond has been proposed as possible plasma facing material, we have studied erosion and hydrogen retention in diamond and amorphous hydrogenated carbon (a-C:H). As in experiments, diamond shows a lower erosion yield than a-C:H, however the hydrogen retention in diamond is much larger than in a-C:H and also hardly depending on the substrate temperature. This implies that simple heating of the surface is not sufficient to retrieve the hydrogen from diamond material, whereas a-C:H readily releases the retained hydrogen. So, in spite of the higher erosion yield carbon material other than diamond seems more suitable.

Experiments suggest that the erosion yield of carbon material decreases with increasing flux. This was studied in our simulations. The results show no flux dependency, suggesting that the observed reduction is not a material property but is caused by external factors as, for example, redeposition of the erosion products. Our study of the redeposition showed that the sticking probability of small hydrocarbons is highest on material previously subjected to the highest hydrogen flux. This result suggests that redeposition is more effective under high than under low hydrogen fluxes, partly explaining the experimentally observed reduction in the carbon erosion yield.

Lastly, we studied amorphous tungsten carbide. Amorphous material with three different carbon percentages (15, 50 and 95%) was subjected to deuterium bombardment and the resulting erosion and deuterium retention was analyzed. The 95% carbon sample behaves like doped carbon, the carbon erosion yield is reduced and no tungsten

is eroded. Segregation of the materials was observed, resulting in an accumulation of tungsten at the surface. The hydrogen retention was similar to a-C:H. The 15% carbon sample showed no significant erosion or retention. The most interesting was the 50% sample. Here deuterium bubbles formed that burst open after sufficiently long bombardment, thereby removing both carbon and tungsten from the surface. In the context of ITER our MD simulations suggest that tungsten is the better suited material since both the erosion and the hydrogen retention are significantly lower than for carbon.

Samenvatting

Een thermonucleaire reactor produceert energie door de fusie van waterstofisotopen, waarbij helium vrijkomt. De zogenaamde divertor is het deel van het reactorvat waar het plasma de wand raakt en geneutraliseerd wordt, zodat het helium kan worden afgevoerd. De oppervlakteplaten van de divertor krijgen grote hittebelasting en flux van energetische waterstof- en heliumkernen te verwerken. In de tokamak ITER - de next generation fusie-installatie - worden de divertorplaten volgens verwachting blootgesteld aan deeltjesflux boven de 10^{24} per seconde en vierkante meter, met deeltjesenergieën tussen 1 en 100 eV en een gemiddelde warmtebelasting van 10 MW per vierkante meter. Er zijn twee kandidaatmaterialen gevonden voor de ITER divertorwand: koolstof en wolfram. Omdat er momenteel geen fusie-installaties zijn die de zware omstandigheden in ITER kunnen nabootsen, is nog onbekend hoe het erosie en waterstofretentie-gedrag van de twee materialen is.

Om meer inzicht te krijgen in de fysische processen onder deze omstandigheden, zijn moleculaire dynamica-simulaties (MD) uitgevoerd. Diamant is voorgesteld als mogelijk plasmagericht materiaal, dus hebben we erosie en waterstof-retentie in diamant en in amorf gehydrogeneerd koolstof (a-C:H) bestudeerd. Diamant vertoonde net als in experimenten een lagere erosie dan a-C:H, maar de waterstofretentie in diamant is veel hoger - en nauwelijks afhankelijk van de temperatuur van het substraat. Dit impliceert dat simpelweg verhitten van het substraat niet genoeg is om het opgenomen waterstof weer te bevrijden, terwijl a-C:H het ingevangen waterstof dan juist makkelijk vrijlaat. Ondanks de hogere erosie lijkt een andere koolstofvariant dan diamant daarom bruikbaar.

Volgens experimenten daalt de erosie van koolstofmaterialen bij stijgende deeltjesflux en dit is onderzocht in onze simulaties. De resultaten laten geen fluxafhankelijkheid zien, wat suggereert dat de waargenomen afname geen materiaaleigenschap is, maar wordt veroorzaakt door externe factoren zoals bijvoorbeeld redepositie van de erosieproducten. Ons onderzoek naar redepositie liet zien dat de plakkans van kleine koolwaterstoffen het grootst is bij materialen die voorheen de hoogste waterstofflux ondergingen. Dit wijst erop, dat redepositie effectiever is naarmate de waterstofflux stijgt, wat deels een verklaring is voor de experimenteel waargenomen lagere koolstoferosie bij hogere flux.

Tenslotte is amorf wolfram carbide onderzocht; amorf materiaal met drie verschil-

lende koolstofpercentages (15, 50 en 95%) werd in de simulatie blootgesteld aan een deuteriumbombardement. De daaruit voortvloeiende erosie en deuteriumretentie zijn onderzocht. Het sample met 95% koolstof bleek zich als gedoteerd koolstof te gedragen - de koolstoferosie is verminderd en er wordt geen wolfram geërodeerd. Er werd segregatie van de materialen waargenomen - het wolfram hoopte zich op aan het oppervlak. De waterstofretentie was vergelijkbaar met die van a-C:H. Het materiaal met 15% koolstof vertoonde geen significante erosie of retentie, maar het interessantst was het sample met 50% koolstof. Hier ontstonden deuteriumbellen in het materiaal, die na voldoende lange deuteriumbeschieting openbarstten en zowel koolstof als wolfram verwijderden. In de context van ITER wijzen onze simulaties erop dat wolfram het beter geschikte materiaal is, omdat zowel de erosie als waterstofretentie significant lager zijn dan voor koolstof.

Acknowledgements

There are many people who in one way or the other helped me to get my PhD degree. They are listed in the following in roughly chronological order:

Special thanks to: Roland Hellwig, Carl Sagan, Holger Fouquet, Mr. Spock, my parents, Frank Moret, Leo van Berkum, Gerrit van Dompseleer, Toine Arts, Bram Achterberg, Rob Rutten, Sandra Franken, Alfred Duteweert, Selma de Mink, Peter Sütterlin, Alfred de Wijn, Onno Pols, Axel Bonacic Marinovic, Johann Sebastian Bach, Hans Goedbloed, Rony Keppens, Niek Lopez Cardozo, Wim Goedheer, Emiel van der Plas, Hugo de Blank, Victor Veremiyenko, Erik Min, Jan-Willem Blokland, Viktor Land, Jeroen Westerhout, Erik Neyts, Annemie Bogaerts, Hennie van der Meiden, Foujun Gou, Aart Kleyn, Hans van Eck, Amy Shumack, Wouter Vijvers, Marco de Baar, Graham Wright, Gerard van Rooij, Rob Wieggers, Wim Koppers, Udo von Toussaint, Wolfgang Jacob, Thomas Schwarz-Seliger, Michael Schlüter, Vasile Vartolomei, Christian Hopf, Jochen Roth, Noud Oomens, Hirokazu Ueta, Kai Nordlund, Emppu Salonen, Annalisa Fasolino, Jonathan Citrin, Gieljan de Vries ... everybody else at the FOM Rijnhuizen institute, the Reaktive Plasmaprozesse group at the IPP in Garching and all the people whom I forgot but who think they should be mentioned (please forgive me!).

They sparked my enthusiasm, made me believe in myself, answered my questions, made me wonder, motivated me, gave me leeway, shared their wisdom with me, listened to my stories and told their stories, endured my sense of humour and my laughter, had a drink with me or dined with me.

And there is one person who did all of the above and who deserves a very special thank you: Frans de Rooij.

Curriculum Vitae

I was born the 12th of September 1965 in Gräfelfing near Munich in Bavaria, Germany. My name at birth was Elisabeth Dagmar Bellinghausen. In 1984 I finished secondary school with Abitur at the St. Joseph Gymnasium in Rheinbach, North Rhine-Westphalia. After some time of searching for the right education I decided to study telecommunications at the Fachhochschule in Dortmund where I received my engineer's degree in July 1992.

In January 1993 I started working for the telecommunications company Ericsson. During my eight years in their employment I worked as software designer, tester, and briefly as project manager and product manager. Ericsson gave me the opportunity to work in several countries besides Germany, namely, Denmark, Australia and The Netherlands. Another even more pleasant outcome of my time at Ericsson's is that I found the best husband in the world. When we got married I changed my last name to de Rooij.

In 2001 I decided to quit my job and to study physics at the university of Utrecht where I graduated in October 2005 with astrophysics as specialisation. In December of the same year I started as PhD student at the FOM Institute for Plasma Physics Rijnhuizen in Nieuwegein. This thesis describes the results of my PhD research.